Electronic Theses and Dissertations, 2004-2019

2012

Optimization Of Process Parameters For Faster Deposition Of Cuin1-xgaxs2 And Cuin1-xgaxse2-ysy Thin Film Solar Cells

Ashwani Kaul
University of Central Florida

Showcase of Text, Archives, Research & Scholarship

OPTIMIZATION OF PROCESS PARAMETERS FOR FASTER DEPOSITION
OF $CuIn_{1-x}Ga_xS_2$ AND $CuIn_{1-x}Ga_xSe_{2-y}S_y$ THIN FILM SOLAR CELLS

by

ASHWANI KAUL
B.S. North Maharashtra University, 2001
M.S. University of Pune, 2004

A dissertation submitted in partial fulfillment of the requirements
for the degree of Doctor of Philosophy
in the Department of Mechanical, Materials and Aerospace Engineering
in the College of Engineering and Computer Science
at the University of Central Florida
Orlando, Florida

Fall Term
2012

Major Professor: Neelkanth G. Dhere

ABSTRACT

Thin film solar cells have the potential to be an important contributor to the world energy demand in the 21st century. Among all the thin film technologies, CuInGaSe$_2$ (CIGS) thin film solar cells have achieved the highest efficiency. However, the high price of photovoltaic (PV) modules has been a major factor impeding their growth for terrestrial applications. Reduction in cost of PV modules can be realized by several ways including choosing scalable processes amenable to large area deposition, reduction in the materials consumption of active layers, and attaining faster deposition rates suitable for in-line processing. Selenization-sulfurization of sputtered metallic Cu-In-Ga precursors is known to be more amenable to large area deposition.

Sputter-deposited molybdenum thin film is commonly employed as a back contact layer for CIGS solar cells. However, there are several difficulties in fabricating an optimum back contact layer. It is known that molybdenum thin films deposited at higher sputtering power and lower gas pressure exhibit better electrical conductivity. However, such films exhibit poor adhesion to the soda-lime glass substrate. On the other hand, films deposited at lower discharge power and higher pressure although exhibit excellent adhesion show lower electrical conductivity. Therefore, a multilayer structure is normally used so as to get best from the two deposition regimes. A multi-pass processing is not desirable in high volume production because it prolongs total production time and correspondingly increases the manufacturing cost. In order to make manufacturing compliant with an in-line deposition, it is justifiable having fewer deposition sequences. Thorough analysis of pressure and power relationship of film properties deposited at various parameters has been carried out. It has been shown that it is possible to achieve a molybdenum back contact of desired properties in a single deposition pass by choosing

the optimum deposition parameters. It is also shown that the film deposited in a single pass is actually a composite structure. CIGS solar cells have successfully been completed on the developed single layer back contact with National Renewable Energy Laboratory (NREL) certified device efficiencies >11%. The optimization of parameters has been carried out in such a way that the deposition of back contact and metallic precursors can be carried out in identical pressure conditions which is essential for in-line deposition without a need for load-lock.

It is know that the presence of sodium plays a very critical role during the growth of CIGS absorber layer and is beneficial for the optimum device performance. The effect of sodium location during the growth of the absorber layer has been studied so as to optimize its quantity and location in order to get devices with improved performance. NREL certified devices with efficiencies >12% have been successfully completed.

Dedicated To

"My Spiritual Master and my Beloved Family"

ACKNOWLEDGMENTS

acknowledge AMPAC's Materials Characterization Facility (MCF). A special word of thanks goes to all the personnel at MCF.

TABLE OF CONTENTS

LIST OF FIGURES

xiv

LIST OF TABLES

LIST OF ACRONYMS

A	Diode Ideality Factor
CdS	Cadmium Sulfide
CIGS	Copper Indium Gallium Diselenide
CIGS2	Copper Indium Gallium Disulfide
CIGSeS	Copper Indium Gallium Selenide Sulfide
CIS	Copper Indium Diselenide
EBSD	Electron Backscattered Diffraction
EDS	Energy Dispersive X-ray Spectroscopy
EPMA	Electron Probe Micro Analysis
eV	electron volts
η	Efficiency (%)
FF	Fill Factor (%)
i:ZnO	Intrinsic Zinc Oxide
J	Current Density (mA/cm^2)
J_0	Reverse Saturation Current Density (mA/cm^2)
J_m	Maximum Current Density (mA/cm^2)
J_{sc}	Short Circuit Current Density (mA/cm^2)
K	Botlzmann's Constant , 8.61×10^{-5} eV/°C
kV	kilo volts
μm	Micrometer (10^{-6} meter)
nm	Nanometer (10^{-9} meter)
P_s	Irradiated Power Density (mW/cm^2)
QE	Quantum Efficiency
R_p	Shunt or Parallel Resistance (Ohm)
R_s	Series Resistance (Ohm)
SEM	Scanning Electron Microscopy
V	Biased Voltage (Volts)

V_{bi}	Built-in Voltage (Volts)
V_m	Maximum Voltage (Volts)
V_{oc}	Open Circuit Voltage (Volts)
W_d	Depletion Width
XRD	X-ray diffraction
ZnO:Al	Aluminum doped Zinc Oxide

CHAPTER 1 INTRODUCTION

Energy has played a dominant role in the growth and development of mankind. The current global power consumption is approximated 15 TW, the vast majority of which is generated through the consumption of fossil fuels such as oil, coal, natural gas and also to some extent by nuclear resources. The world energy demand is projected to be 30% higher in 2040 compared to the current usage [1]. There are bound to be concerns regarding how long the existing fossil energy resources would last. The International Energy Outlook expects a nearly 50 percent jump in global energy demand by 2035 as shown in Figure 1.
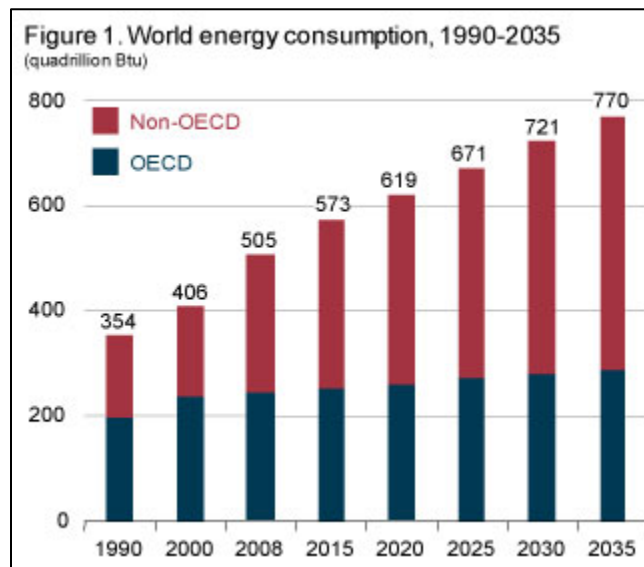
Figure 1 World energy consumption 1990-2035 [1]

The production of energy using fossil resources poses a serious threat to the overall health of the global environment. Burning of fossil fuels produces ~21.3 billion tons of CO_2 per year [2]. A major threat faced by mankind is the harmful effects of global warming due to the

accumulation of greenhouse gases in the atmosphere. CO_2 (82%), methane (9%), nitrous oxide (5%), and pollutants (4%) constitute the greenhouse gases in the atmosphere [3]. The effect of global warming on climatic changes seems to be accelerating with every passing year. Hence during the last two decades there has been an enhanced interest in the development of clean renewable resources for energy production.

1.1 Renewable Energy Technology

The world currently relies heavily on coal, oil, and natural gas for its energy requirements. Fossil fuels are non-renewable, that is, they draw on finite resources that will eventually dwindle, becoming too expensive or too environmentally damaging to retrieve. On the other hand, there are several types of renewable energy resources that are constantly replenished and will never run out.

The most promising source of clean, safe and abundant energy is the sun. The total solar energy captured by the earth's surface in one hour is ~14 TWyr. Thus solar has the great potential to meet a large fraction of energy needs. In fact, most renewable energy comes either directly or indirectly from the sun. **Solar energy** can be used directly for heating and lighting homes and other buildings, for generating electricity, and for hot water heating, solar cooling, and a variety of commercial and industrial applications. The sun's heat also drives the winds, whose energy, is captured using wind turbines. The winds and the sun's heat cause water to evaporate. When this water vapor turns into rain or snow and flows downhill into rivers or streams, its energy can be captured using **hydroelectric power**.

Along with the rain and snow, sunlight is also responsible for growth of plants by the process of photosynthesis. The organic matter that makes up those plants is known as biomass. Biomass can be used to produce electricity, transportation fuels, or chemicals. The use of biomass for any of these purposes is termed **bioenergy**.

Hydrogen can be found in many organic compounds as well as in water. It is the most abundant element on the Earth. However, it does not occur naturally as a gas. It always exits in a combined form with other elements, such as with oxygen to make water. Once separated from another element, hydrogen can be burned as a fuel or converted into electricity.

Not all renewable energy resources are derived from the sun. **Geothermal** energy taps the Earth's internal heat for a variety of uses, including electric power generation and the heating and cooling of buildings.

The energy of the ocean's tides is realized due to the gravitational pull of the moon and the sun upon the Earth. In fact, ocean energy comes from a number of sources. In addition to **tidal energy** there is the energy of the ocean's waves, which are driven by both the tides and the winds. The sun also warms the surface of the ocean more than the ocean depths, creating a temperature difference that can be used as an energy source. All these forms of energies from ocean can be used to generate electricity.

1.2 Harvesting Solar Energy

It is clear from the above discussion that solar energy is the strongest contender among various renewable energy technologies. By the end of this century mankind may possibly run out of fossil fuels. The energy reaching the earth's surface is ~7000 times the present global energy

consumption. Sun's energy is abundant and clean. If 1% of the unused land area is used ~4 times more electricity could be produced as compared to the fossil fuels and nuclear power [4]. Hence technology has to be developed so as to efficiently produce and store the electricity from sun.

Energy from the sun can be used to heat homes through passive solar design, solar hot water systems, solar space heating and electrical generation using solar panels (photovoltaics).
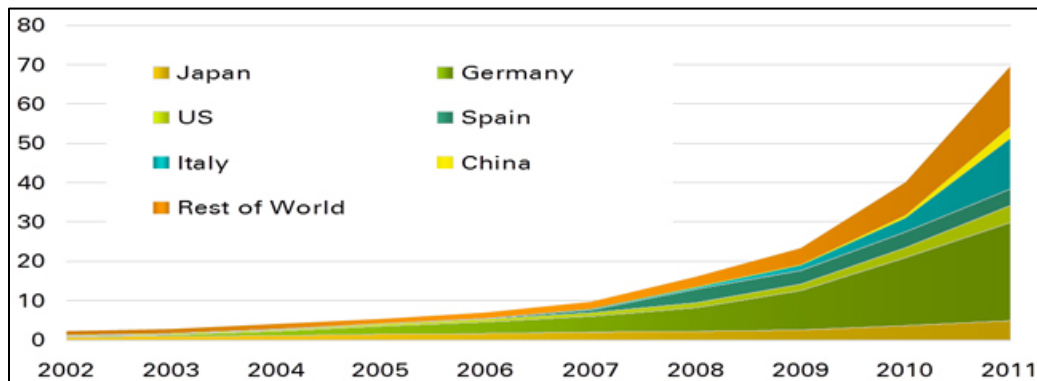
Figure 2 Solar PV generation Capacity (Source: BP Solar)

1.2.1 Photovoltaics

Solar power generating capacity grew by 73.3% in 2011, the fastest growth recorded since 1996. Total capacity grew by 29.3 GW to reach 63.4 GW. Capacity has grown almost ten-fold over the past 5 years. As seen in Figure 2, Solar capacity growth in 2011 was dominated by two countries, Italy (9.3 GW added) and Germany (7.5 GW). Together they accounted for 57.1% of global capacity growth in 2011. Germany remains the leader for cumulative installed capacity (24.8 GW), and Italy (12.8 GW) has leapt into second place ahead of Japan (4.9 GW). China, already the leading manufacturer of solar PV, has started to develop its domestic solar market,

adding 2.2 GW in 2011. China completed a 200 MW solar PV plant, which was at the time the world's largest solar PV plant.

Solar power generation enjoyed spectacular growth in 2011, with a record 86.3% increase. Its overall share of renewable power remains low (6.5%), but 2011 marked the arrival of solar power at scale, contributing 20% of the growth of renewable power in 2011 [5].

1.2.2 Solar PV Technologies

Crystalline silicon (c-Si) solar cells are considered as the first generation solar cell technology. The present solar cell market is dominated by silicon based solar cells having a share of 90% while market share of thin film modules is 10% [6]. Figure 3 provide the growth in the efficiency of various PV technologies around the world.

As of 2012, the worldwide thin film PV market is worth $3 Billion and the thin film market share is ~ 10% of the total PV market. Most of the other market share belongs to Silicon wafer based technologies. The CIGS based technologies constitute ~ 2 % of the market in 2012 [Source: GTM Research].

Thin film PV industry has grown significantly over the last ten years. Shipments of thin film PV grew from a very small value of 68 megawatt in 2004 to 2 gigawatt in 2009 - at a compound annual growth rate (CAGR) of 97 %. Figure 4 shows the historic thin film production since year 2002.
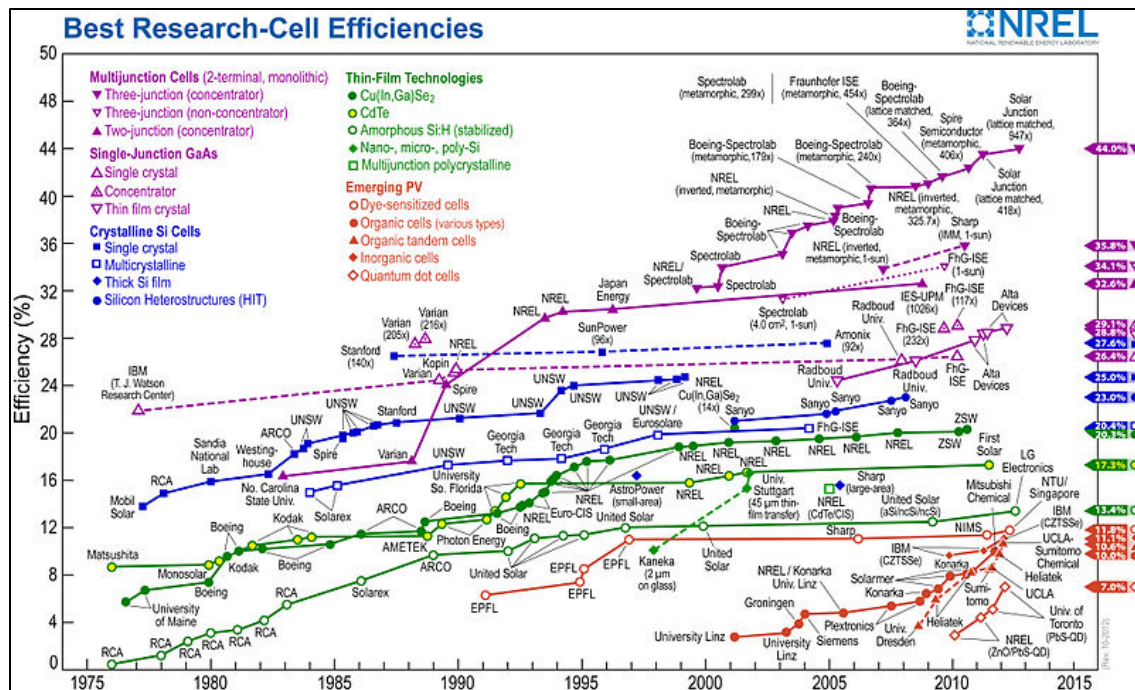
Figure 3 PV efficiency chart-present status [Source: NREL]
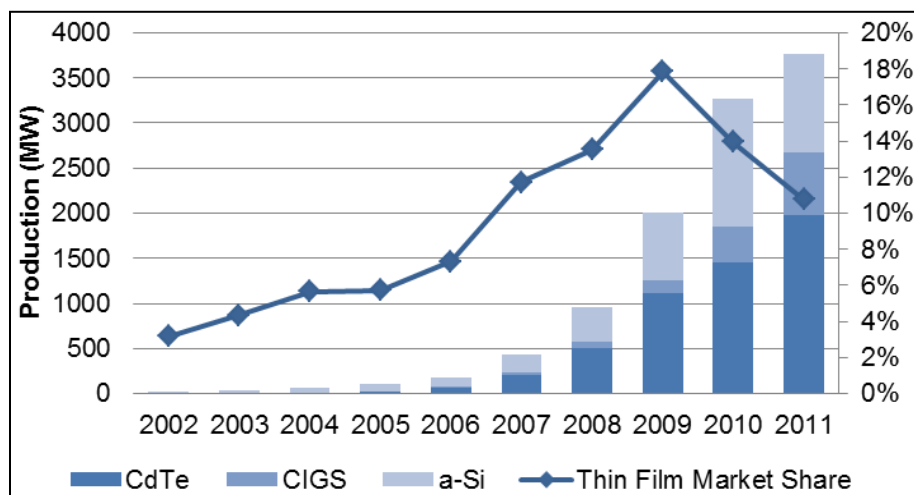
Figure 4 Historic Thin Film PV Production (Source: GTM Research)

The thin film PV market share rapidly increased between 2005 through 2009 and reached its summit at 18% in 2009 during the period of polysilicon bottleneck. After 2009, the thin film market share continued to fall every year due to rapid decrease in price and over supply of polysilicon. In 2011, polysilicon based PV modules dropped in price by over 40% during the course of the year. Prior to these last few years thin-film PV was considered a superior alternative due to the low material consumption and freedom from the unstable prices of polysilicon. As the price of silicon based PV rapidly decreased the value proposition of thin-film solar cells was undermined. Although the original cost advantages have been compromised, there are still several advantages to thin-film PV such as better energy output per nameplate power rating due to improved performance in low light and high temperature conditions. Figure 5 shows the comparison of historic thin film PV growth and the polysilicon spot prices. It is clear from the figure that as the polysilicon prices crashed after 2008, the YoY growth rate of thin film PV fell from 140% to mere 20%.
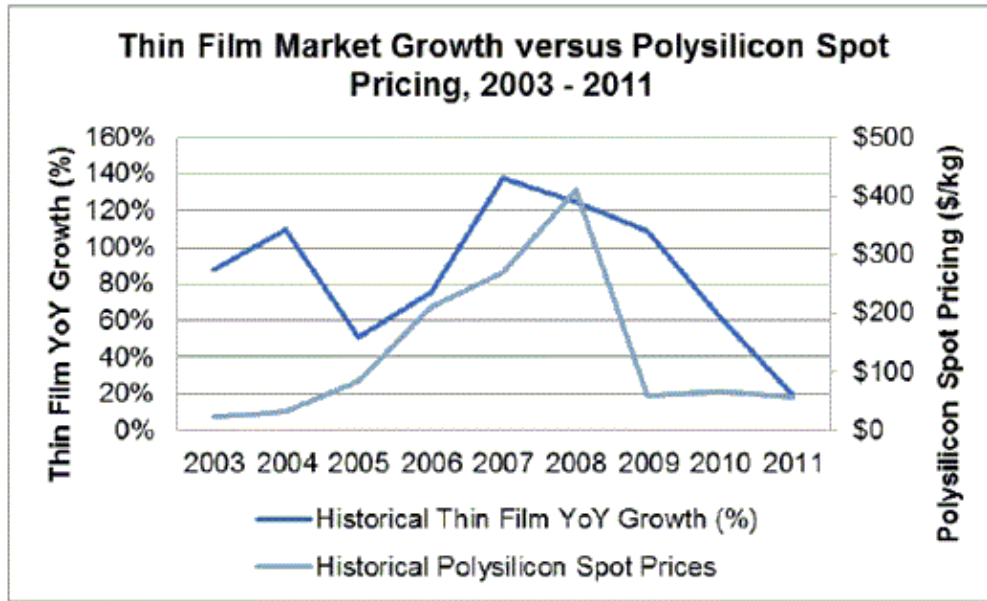
Source: Thin Film PV 2012- 2016: Technologies, Markets and Strategies for Survival

Figure 5 Comparison of Thin Film Year over Year (YoY) growth and polysilicon spot pricing

1.2.3 Future for Thin Film PV Manufacturers

Despite of the challenging times faced by the thin film PV manufacturers, there is a promising future for the CIGS PV manufacturers in the years ahead. The GTM Research's "Thin Film 2012-2016: Technologies, Markets, and Strategies for Survival" report forecasts global thin film production and total market value dipping below $3 billion in 2012. But the report also projects a jump in thin film demand in 2015-2016, when the total market recovers to $7.6 billion. In particular, the report forecasts strong growth in the CIGS technology segment, forecasting production at 4 GW in 2016. The industry's recovery is based on the assumptions that thin film PV manufacturers would manage to follow their efficiency and cost per watt road maps. The thin film modules perform better than the polysilicon modules in the low light as well as high

8

temperature environments. Hence, they have better energy yield performance than their polysilicon based counterparts.

CHAPTER 2 SEMICONDUCTOR DEVICE PHYSICS

2.1 Energy Levels in an Isolated Atom

An electron of an isolated atom can have discrete energy levels as given by the following approximation;

$$E_n = \frac{-Z^2 m_0 q^4}{8\varepsilon_0^2 h^2 n^2}$$ …..………………………………………………………………………. (1)

Where,

q- Electron charge;

Z- Atomic Number;

m_0- Mass of free electron;

ε_0- Permittivity of free space;

h- Plank's constant;

n- Principal quantum number

When two such identical atoms are brought in close proximity the energy level for the electron will be split into two levels by the interaction between the two atoms. Now let us consider a solid where there are N atoms very closely packed. The outer orbits of each atom then overlap and interact with each other. This results in shifting of the energy levels and N separate narrowly spaced energy levels are formed and for larger values of N which is generally the case in solids it results in a semi-continuous band of energy. Figure 6 illustrates the formation of energy bands in solids.
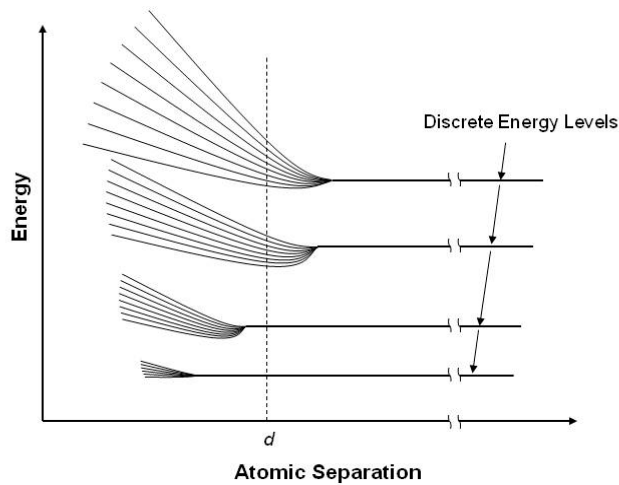
Figure 6 Formation of energy bands in a solid

2.2 Classification of Materials Based on Energy Levels of Electrons

Materials can be classified into metals, semiconductors and insulators based on the position of the valence band and conduction band (Figure 7). The conduction and valence bands completely overlap with each other in case of metals, resulting in no band gap. Therefore, electrons are free to move under the influence of very small electric field due to the availability of several empty states.
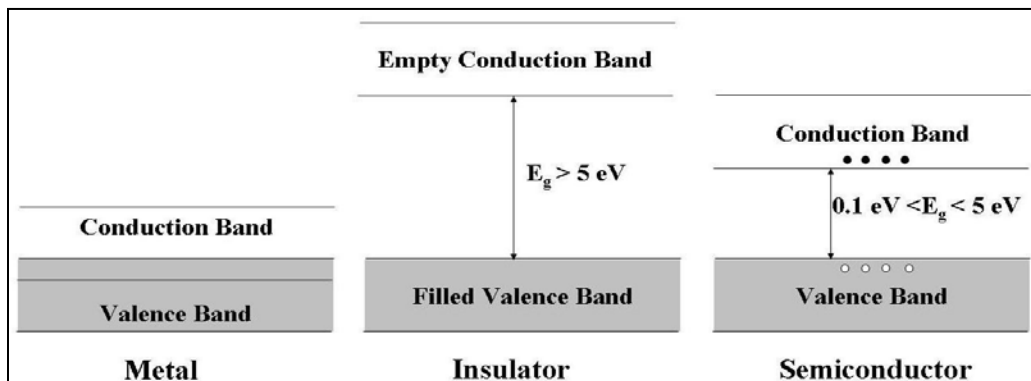
Figure 7 Energy band diagram of metal, insulator and semiconductor

For an insulator at room temperature, the valence band is completely filled with bound electrons and the conduction band is almost unoccupied with free electrons. Due to large bandgap (>5eV) the electrons cannot accelerate under the influence of an electric field. In semiconductors on the other hand, the valence band is completely filled at 0 °K while the bandgap is considerably smaller than that of the insulator. The thermal agitation at room temperature can excite some electrons from the valence band into the conduction band. The conduction band has many available empty energy states and hence the electrons are free to accelerate under the influence of an electric field. Thus, the conductivity of a semiconductor lies in between those of metals and insulators.

2.3 *p-n* junction

Since a solar cell is essentially a *p-n* junction, it is important to get a basic understating of them. The semiconductors can be classified into intrinsic or extrinsic. An intrinsic semiconductor or an undoped semiconductor is pure with a very low concentration of impurities. When an intrinsic semiconductor is doped with impurities it is known as an extrinsic semiconductor. An extrinsic semiconductor can be classified as n-type and p-type. An intrinsic semiconductor doped with donor impurities that provide extra electrons is known as n-type and that doped with acceptor impurities that provide extra holes is known as p-type.

When two isolated n-type and p-type material are electrically connected they form a metallurgical p-n junction. When a *p-n* junction is formed, there exists a large carrier concentration gradient at the junction. This leads to diffusion of electrons from the n-side to the p-side and diffusion of holes from the p-side to the n-side. As the electrons continue to diffuse to

12

the p-side some of the positive donor ions are left uncompensated on the n-side as they are fixed

in the lattice. Similarly diffusion of hole to the n-side causes some of the negative acceptor ions

to be left uncompensated on the p-side. This results in a negative space charge being formed near

the p-side of the junction and a positive space charge being formed near the n-side of the

junction as shown in Figure 8. The space charge region creates an electric field that is directed

from the positive charge to the negative, thus opposing the diffusion tendency of majority

carriers. A potential buildup occurs across the junction due to the electric field. The electric field

and the potential distribution are also shown in Figure 8.
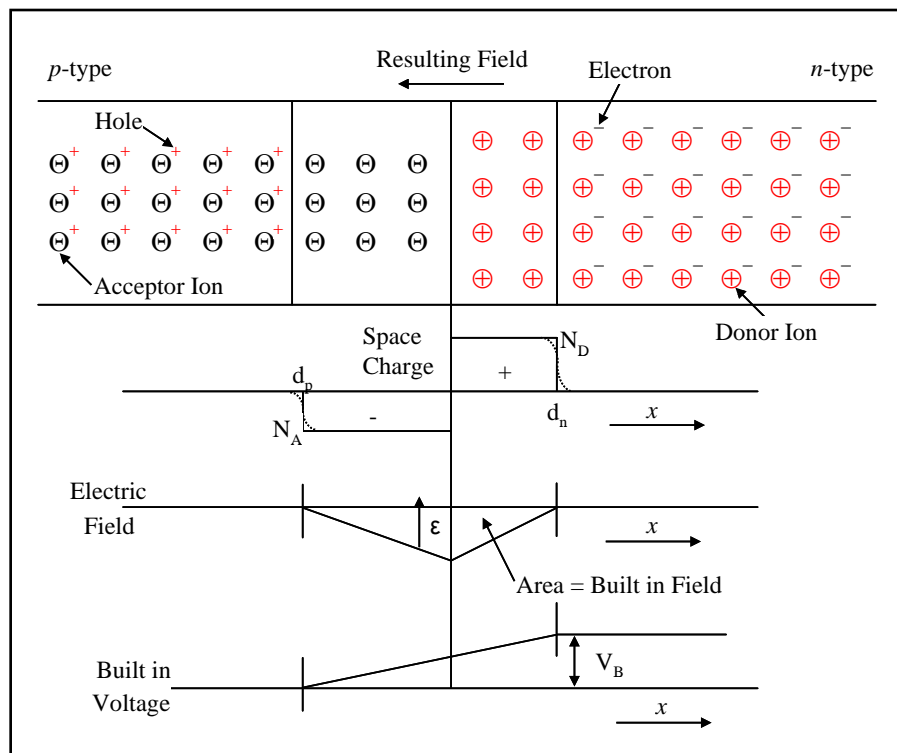
Figure 8 Formation of Space charge region, electric field and built in potential when *n* and *p* type semiconductor are brought in intimate contact

2.3.1 Types of *p-n* Junction

(a) *Homojunction*

      A homojunction is the interface formed between a *p*-type and an *n*-type of the same semiconductor material.
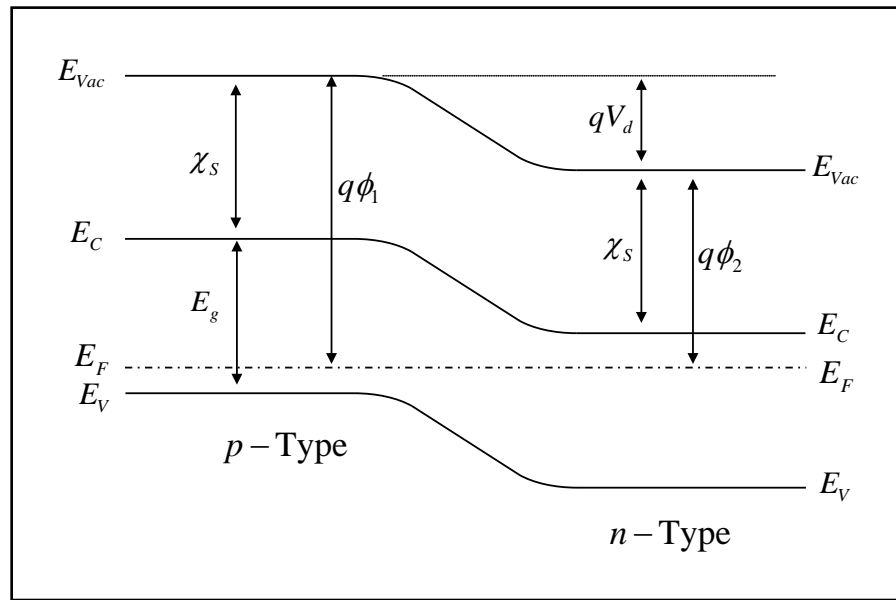
Figure 9 Energy band diagram of a homojunction

      Here,

E_{vac}	: Vacuum level
E_C	: Conduction band Minima
E_V	: Valence band Maxima
E_F	: Fermi level Energy
E_g	: Bandgap Energy
χ_s	: Electron Affinity
Φ_d	: Diffusion Potential
Φ_{wp} and Φ_{wn}	: Work functions for *p* and *n* sides respectively.

(a) *Heterojunction*

A heterojunction is an interface formed between two dissimilar semiconductor materials with different bandgaps, electron affinities and work functions. Figure 10 shows the example of two semiconductors and their important parameters. Discontinuity may occur at the junction between valence and conduction bands. It can be seen that a spike has appeared in the conduction band and a cliff in the valence band at the junction due to band bending. A spike in the conduction band is the result of properties specific to the material such as the electron affinity (χ) and the cliff in the valence band is a result of difference in energy bandgap. Presence of spike and cliff limit electron current that flows from *p* to *n* region when light is incident on the solar cell.
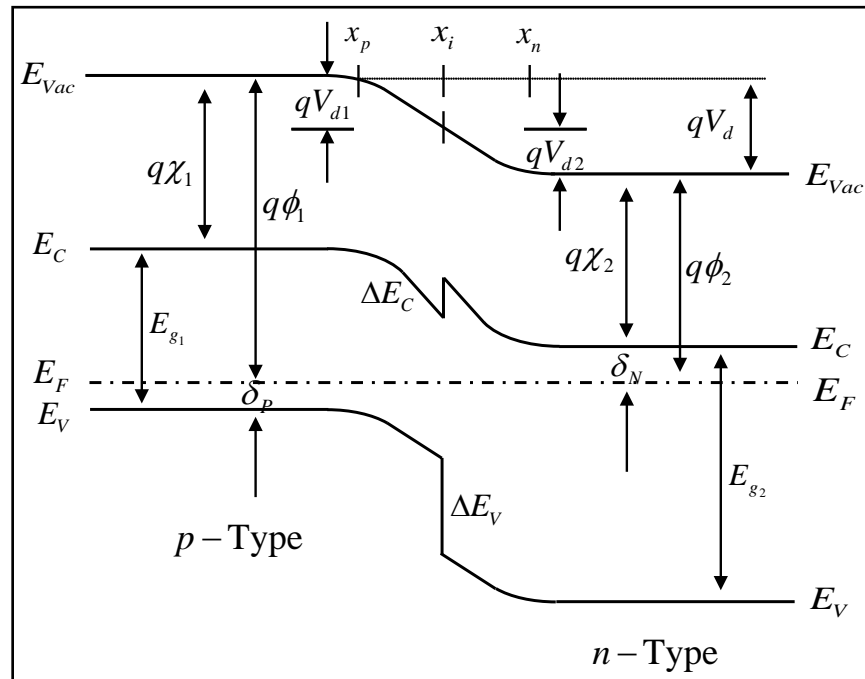
Figure 10 Energy band diagram of a heterojunction

Here, E_{g1} and E_{g2} : Bandgaps

$q\varphi_1$ and $q\varphi_2$: Work Functions

$q\chi_1$ and $q\chi_2$: Electron Affinities

2.4 An Ideal Solar Cell

An ideal solar cell under illuminated conditions can be described as a photo diode with a current source connected in parallel. Figure 11 provides schematic of an equivalent circuit of a solar cell under illumination. The diode represents the p-n junction of the solar cell and the current source represents the photo generated current. Under dark, a solar cell behaves like a diode. It follows the diode equation 1 [7]. The part of the circuit on the left of the two dots is the cell and remaining on the right is the load, characterized by the load resistor (R_{Load}). An actual solar cell has a series resistance (R_s) and a shunt resistance (R_{sh}). Ideally the values of $R_s = 0$ and $R_{sh} = \infty$. The value of R_s and R_{sh} depend upon the properties of the solar cell. R_s of a cell can arise from the following reason: (*i*) bulk resistance of the individual layers, (*ii*) interface resistance between layers such as between absorber and back contact, and between front contact window layer and the contact fingers (*iii*) contact resistance of front contact. The shunt resistance R_{sh} takes into account the parallel current paths due to recombination in the absorber material and the value of R_{sh} reduces as the number of shunt paths increase. The effect of R_s on short circuit current and R_{sh} on the open circuit voltage is shown in Figure 12 and Figure 13 respectively.
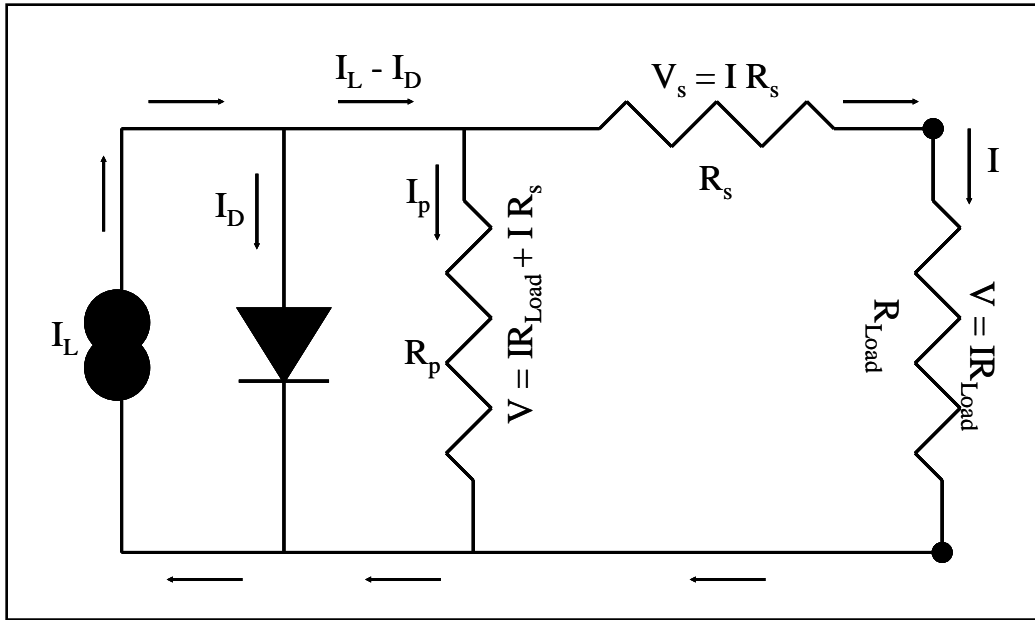
Figure 11 Equivalent Circuit of a Solar Cell
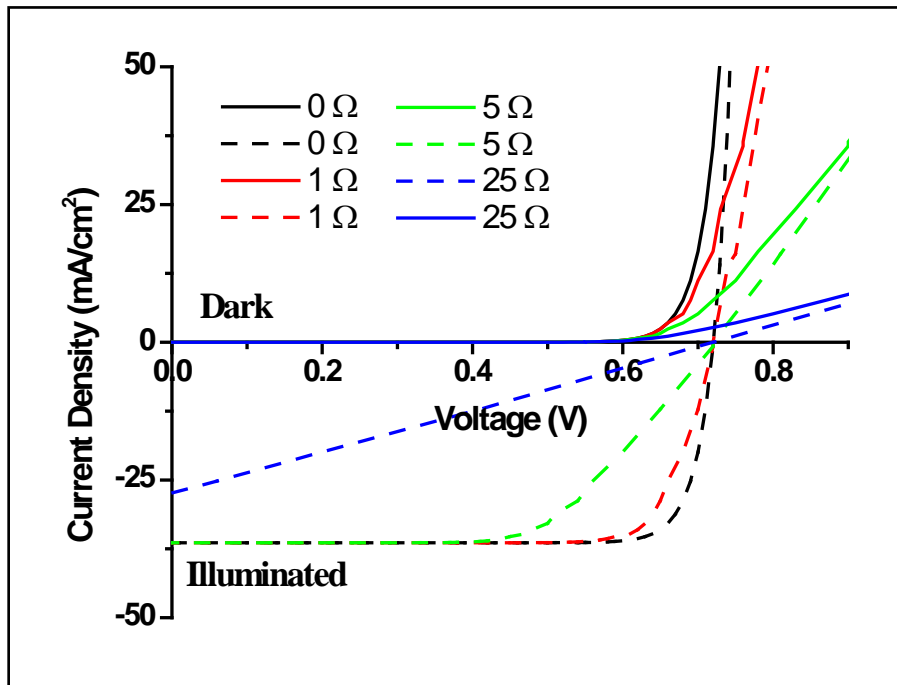
Figure 12 Effect of series resistance on solar cell short circuit current density
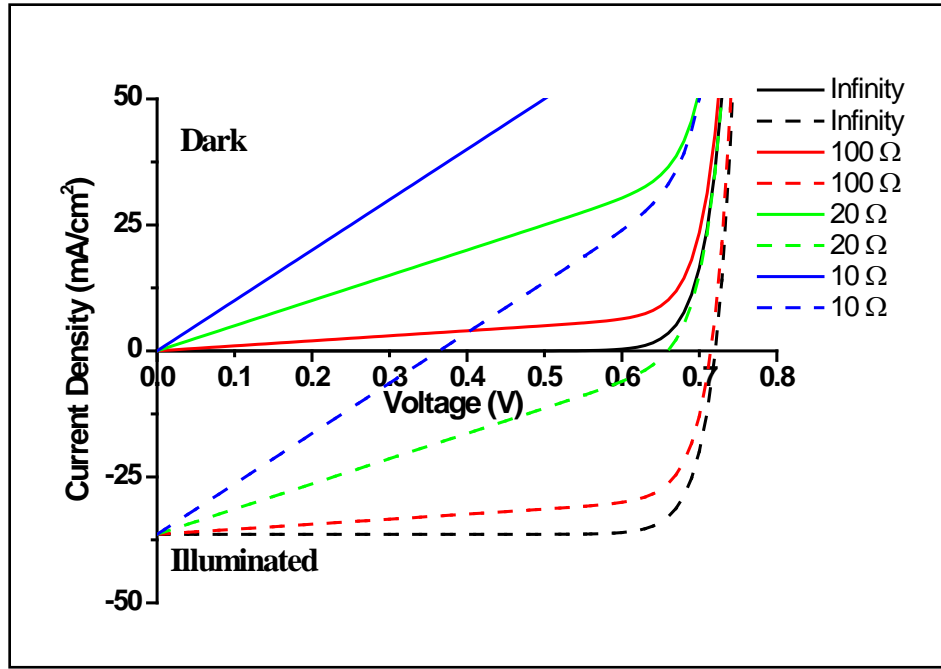
Figure 13 Effect of Shunt Resistance on solar cell open circuit voltage

$$I = I_0 \left(e^{qV/k_B T} - 1 \right) \ldots\ldots\ldots\ldots\ldots\ldots\ldots\ldots\ldots\ldots\ldots\ldots\ldots\ldots\ldots\ldots\ldots\ldots\ldots\ldots \quad (2)$$

Here, I_0 : Diode Reverse Saturation Current

              q : Electron Charge

              V : Voltage at the terminal ends

              T : Absolute Temperature (K)

              k_B : Boltzmann constant

Similarly, under illumination, the corresponding current-voltage equation of an ideal solar cell is modified to equation 3.

$$I = I_0\left(e^{qV/k_BT} - 1\right) - I_L \quad\text{...} \quad (3)$$

Here, I_L is the photogenerated current.

Under illumination the total current through the external circuit is the combination of the photogenerated current and the diode current. Under the short circuit condition the voltage, V = 0. Hence from equation 2.7, the short circuit current (I_{sc}) is equal to the photogenerated current (I_L).

$$I_{SC} = I_L \quad\text{...} \quad (4)$$

Open circuit voltage (V_{oc}) is obtained by setting the total current to zero in Equation 3.

$$V_{OC} = \frac{kT}{q}\ln\left[\frac{I_L}{I_0} + 1\right] \approx \frac{kT}{q}\ln\left[\frac{I_L}{I_0}\right] \quad\text{..} \quad (5)$$

The ideal current-voltage characteristics of a solar cell under dark and illuminated conditions are depicted in Figure 14.

Equation 3 does not include the effects of R_s and R_{sh} on the solar cell performance. The modified I-V equation is given by equation 6 as follows,

$$\ln\left[\left(I + \frac{I_L}{I_0}\right) - \frac{V - I.R_s}{I_0.R_{sh}} + 1\right] = \frac{q(V - I.R_s)}{kT} \quad\text{...} \quad (6)$$
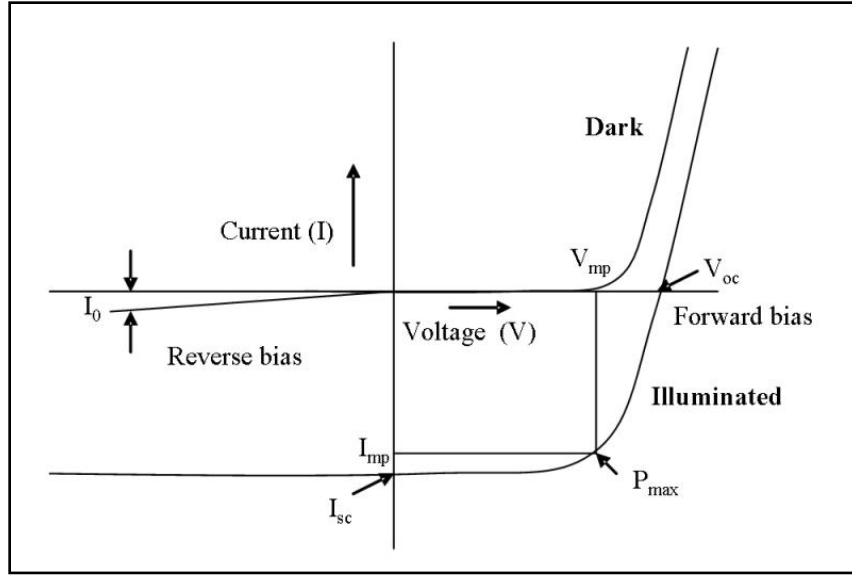
Figure 14 Current Voltage characteristics of a solar cell in dark and under illumination

The power generated at V_{oc} and I_{sc} is zero. The maximum power (P_{max}) is generated by cell at a voltage (V_{mp}) and at current (I_{mp}). Fill factor is the measure of squareness of the I-V curve defined mathematically as:

$$FF = \frac{V_m.I_m}{V_{oc}.I_{sc}} = \frac{P_{max}}{V_{oc}.I_{sc}} \dots\dots\dots\dots\dots\dots\dots\dots\dots\dots\dots\dots\dots\dots\dots\dots\dots\dots\dots\dots \text{(7)}$$

The conversion efficiency (η) of a solar cell is the ratio of the maximum power output (P_{max}) that can be extracted from the device to the incoming power (P_{in}):

$$\eta = \frac{P_{max}}{P_{in}} = \frac{FF.V_{oc}.I_{sc}}{P_{in}} \dots\dots\dots\dots\dots\dots\dots\dots\dots\dots\dots\dots\dots\dots\dots\dots\dots\dots\dots\dots \text{(8)}$$

For laboratory measurements, $P_{in} = 100$ W/cm^2, corresponds to the AM1.5 solar spectrum.

CHAPTER 3 MATERIALS REVIEW

3.1 Thin Film Solar Cells

Thin film solar cells are being developed with the active absorber layer thickness approximately 2-3µm instead of having a thickness of 180-300 µm typically used for crystalline silicon solar cells. This difference arises due to the fact that direct band gap semiconductors need small thicknesses to effectively absorb the solar radiation as against indirect band gap materials that need a reasonable thickness (at least 50 µm) to absorb the solar radiation. The actual thicknesses are much higher in crystalline silicon solar cells essentially to impart some mechanical strength to the wafers in order to make their handling easier without breakage.
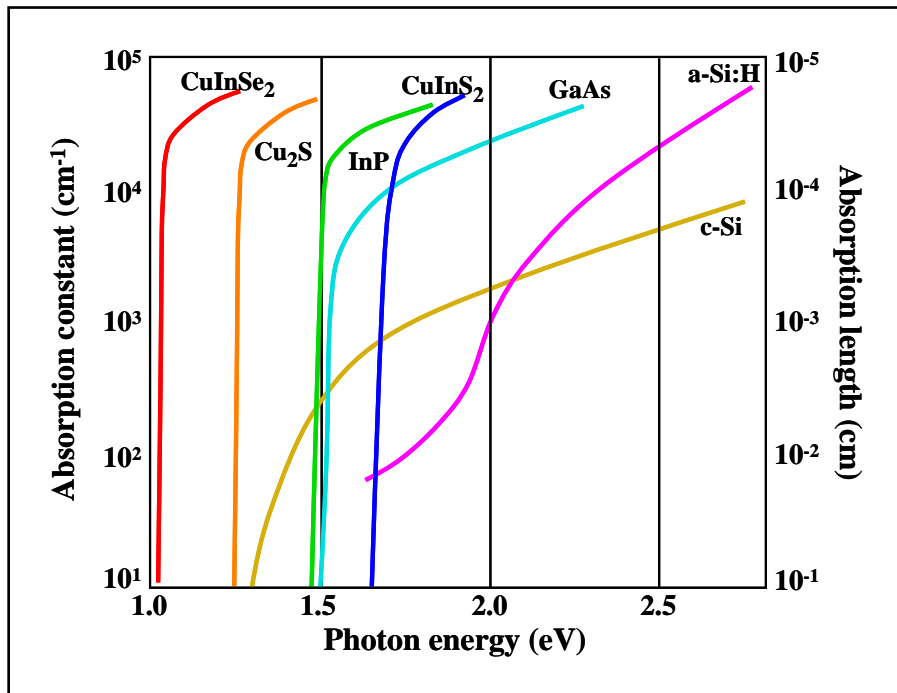
Figure 15 Variation of optical absorption coefficient with photon energy

Thin film solar cells offer several advantages over c-Si technology which are realized in the form of cost savings. These advantages are:

- The material consumption is reduced since the absorber thickness is lower for absorption of photon radiation

- By choosing scalable manufacturing technique such as sputtering, large area deposition is possible

- Due to monolithic integration of thin film solar cells the cost and time associated with wafer to wafer soldering is reduced

- The purity requirement for the materials is low. Essentially, in the case of crystalline silicon solar cells high purity of materials is necessary since the electron-hole pairs are generated far away from the built-in electric field. Presence of impurities would reduce the diffusion length of the charge carriers. However, in case thin film solar cells most of the electron-hole pairs are generated close to the built-in electric field and are separated by drift component instead of diffusion. Therefore, it is possible to use relatively low purity materials.

- The thermal budget associated with processing of c-Si solar cells is very high, due to high melting point of silicon. However, thin films solar cells can be fabricated at much lower temperatures, thereby, reducing the cost associated with high temperature processing.

3.2 Current Thin Film Technologies in the Market

The current thin film technologies that are manufactured on large scale include;

- Hydrogenated amorphous silicon (a-Si:H)

- Cadmium telluride (CdTe)

- Copper indium gallium selenide (CIGS)

3.3 CIGS Thin Film Solar Cells

      Compounds in the I-III-VI$_2$ family have an immense potential to make a significant contribution to address the energy need of the world. The initial development of thin film solar cells was pioneered with the study of Cu$_2$S/CdS heterojunction [8]. However, the research had to be abandoned on account of instability issues associated with these cells that resulted in their very fast degradation essentially due to migration of copper atoms. Later it was found that the addition of trivalent indium to the Cu$_2$S structure prevented the degradation due to copper migration and thus evolved the CuInSe$_2$ (CIS) thin film solar cells. CuInSe$_2$ and its alloys with gallium and sulfur have shown so far the highest conversion efficiencies of 20.3% [9].

3.3.1 Optical absorption

      High optical absorption coefficient is one of the properties that make CIS material well suited for solar cells applications as depicted in Figure 15. Hence, as mentioned before, CIS absorbers would require very small amount of material (~100 times less) compared to the crystalline silicon for the same extent of light absorption.

3.3.2 Band Gap Engineering

      CIS has a direct bandgap of 1.02±0.01 eV at room temperature with a temperature coefficient of -2±1 x 10^{-4} eV/K in the lower temperature range [10]. The typical absorption coefficient is greater than 10^5/cm for 1.4 eV and higher photon energies [11]. One of the

advantages of the compound semiconductors of I-III-VI$_2$ family is that various alloys can be mixed together to form compounds with variety of material properties and band gap energies as shown in figure 8. The band gap can be varied from 1.02 eV for CIS all the way up to 2.7 eV for CuAlS$_2$. Within CIS incorporation of gallium (Ga) leads to an increase in the bandgap over a wide range up to 1.68 eV by increasingly substituting In by Ga. The band gap increase due to Ga content is governed by the equation 9 [12]. Essentially the increase in band gap is due to increase in the energy of the conduction band as shown in Figure 17 [13].
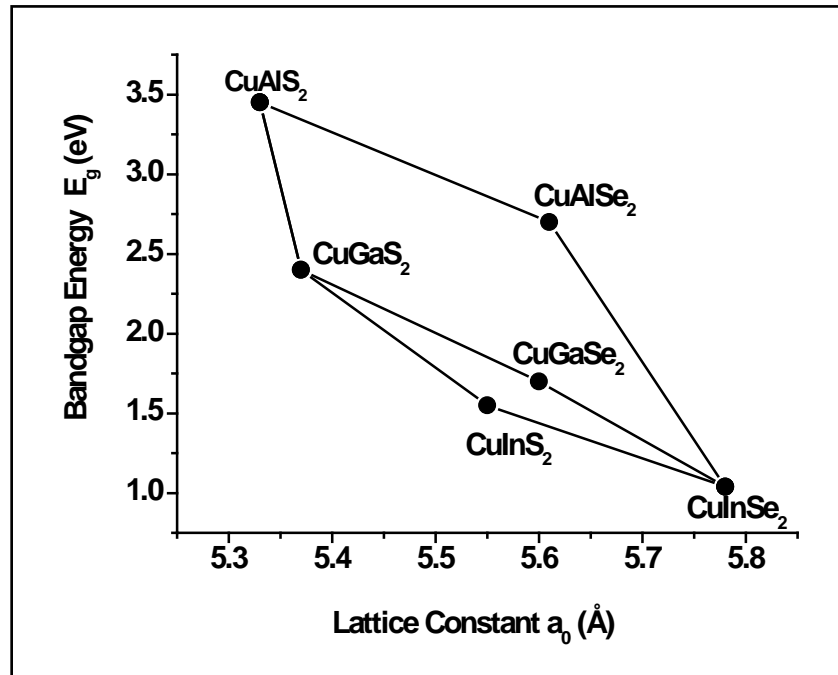
Figure 16 Variation of band gap energy with lattice constants for copper chalcopyrite materials

$$E_{g(x)} = E_{g(0)} + (E_{g(1)} - E_{g(0)})x + bx(x-1) \dots\dots\dots\dots\dots\dots\dots\dots\dots\dots\dots\dots\dots\dots 9$$

Where,

$E_{g(0)}$: Band gap of CuInSe$_2$ (1.02 eV)

$E_{g(1)}$: Band gap of CuGaSe$_2$ (1.68 eV)

b : Bowing parameter (0.15 – 0.24 eV for CuInGaSe$_2$)

x : Gallium concentration

Due to higher chemical activity of selenium with indium, gallium tends to diffuse towards the back contact and forms CuGaSe$_2$ (CGS) [14]. CGS is a wide bandgap semiconductor with a bandgap of 1.68 eV. The bandgap gradient created between CIS and CGS creates a back surface field (BSF) that acts as a mirror for the electrons moving towards the back contact. The BSF greatly minimizes the back contact recombination and thus increases the V$_{oc}$ [15].
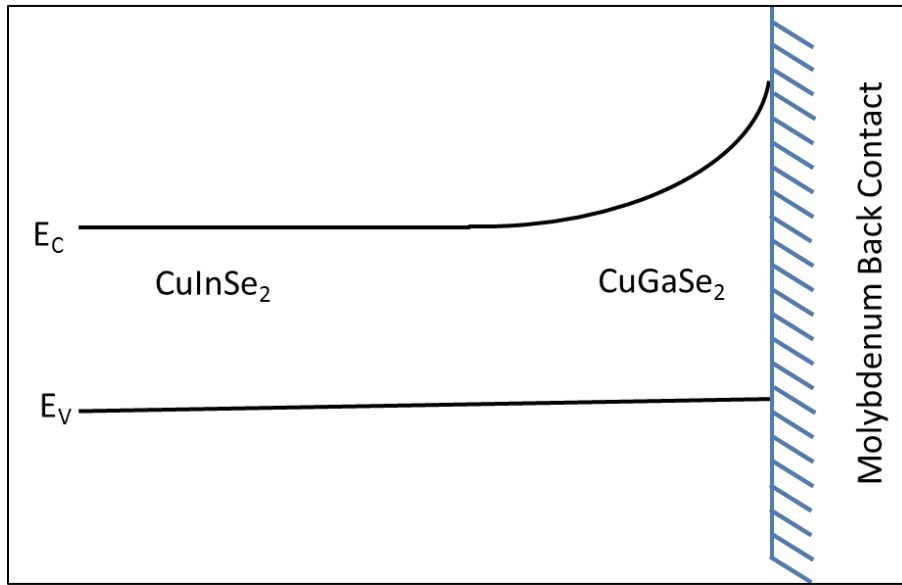
Figure 17 Bandgap bending due to formation of CGS compound

Similarly, the band gap can also be increased by up to 2.4 eV by substituting S for Se. CuInGaS$_2$ (CIGS2) is a wide bandgap semiconductor with a bandgap of 1.54 eV, higher than that

of CIGSe. Sulfurization of CIGSe leads to formation of CIGSeS compound at the surface of the absorber. This helps in increasing the bandgap of the absorber at the interface by shifting the valence band maxima to lower energies as shown in Figure 18. However, the grading depends on the time, temperature and also on the sulfur content. The increase in the bandgap due to the addition of sulfur is governed by the equation 2 as follows:

$$E_g = 0.95 + 0.8x - 0.17x(1-x) + 0.7y - 0.05y(1-y) \dots\dots\dots\dots\dots\dots\dots\dots\dots\dots\dots\dots 10$$

Where, x, y corresponds to the concentrations of selenium and sulfur respectively.
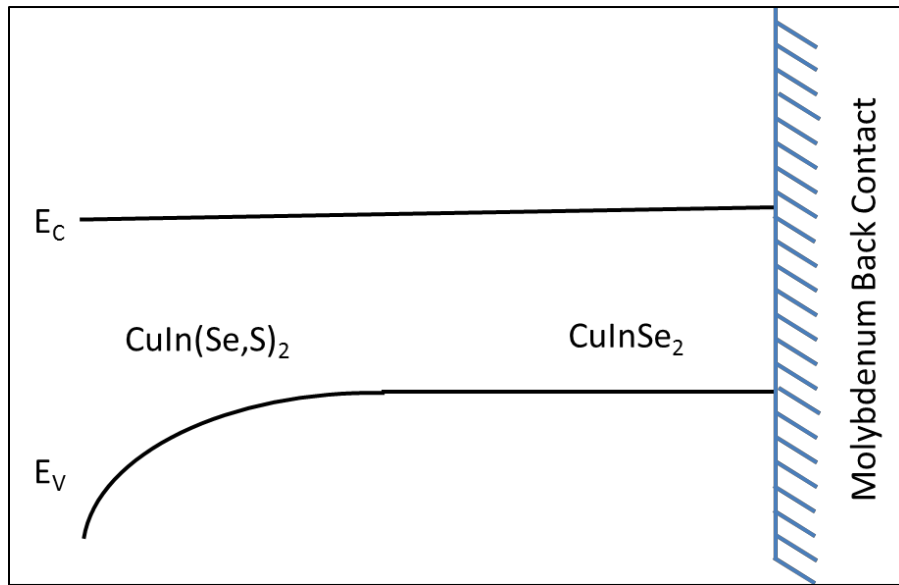
Figure 18 Bandgap bending due to formation of CIGSeS compound at the surface of CIGSe absorber

In a two-stage process, growth of favorable grains takes place at the expense of the unfavorable grains. Large numbers of small grains are present at the molybdenum/CIGSe

interface. Due to higher diffusivity of sulfur in the crystal, a longer sulfurization treatment leads to formation of CIGSeS or CGSeS, thus lowering the valence band. An excessive amount of sulfur can react with molybdenum at higher temperatures to form a thick MoS_2 layer which subsequently increases the series resistance of the cell and thereby, reduces the fill-factor. Therefore, optimization of sulfurization time is very critical to derive the best from this treatment without degrading the device parameters. Sulfur is also known to passivate and reduce the compensating donors at the CIGSe surface by either replacing the existing selenium or by occupying the existing vacancies [16].

3.3.3 Crystal Structure

CIS and its alloys belong to the I-III-IV$_2$ family that crystallizes in tetragonal chalcopyrite structure. The tetragonal chalcopyrite structure results from the cubic Zinc blend structure of ZnS as depicted in Figure 19 in which the Zn sites are replaced alternatively by Cu(I) and In/Ga(III) atoms. Each Cu(I) and In/Ga(III) atom has four bonds with the Se(IV) atom. In turn each Se atom has two bonds with Cu and two with In/Ga atoms. Since the bond strengths of I-VI and III-VI bonds are in general different, therefore, the ratio of the lattice constants (c/a) is not exactly 2. This deviation from c/a =2 is termed 'tetragonal distortion'. The value of c/a can vary from 2.01 for CuInSe$_2$ to 1.96 for CuGaSe$_2$. The system of copper chalcopyrites covers a wide bandgap of energies ranging from 1.02 eV in CuInSe$_2$ to 2.4 eV in CuGaSe$_2$ thus covering most of the visible spectrum. Since there is no miscibility gap in this system any desired alloys can be produced between these compounds.
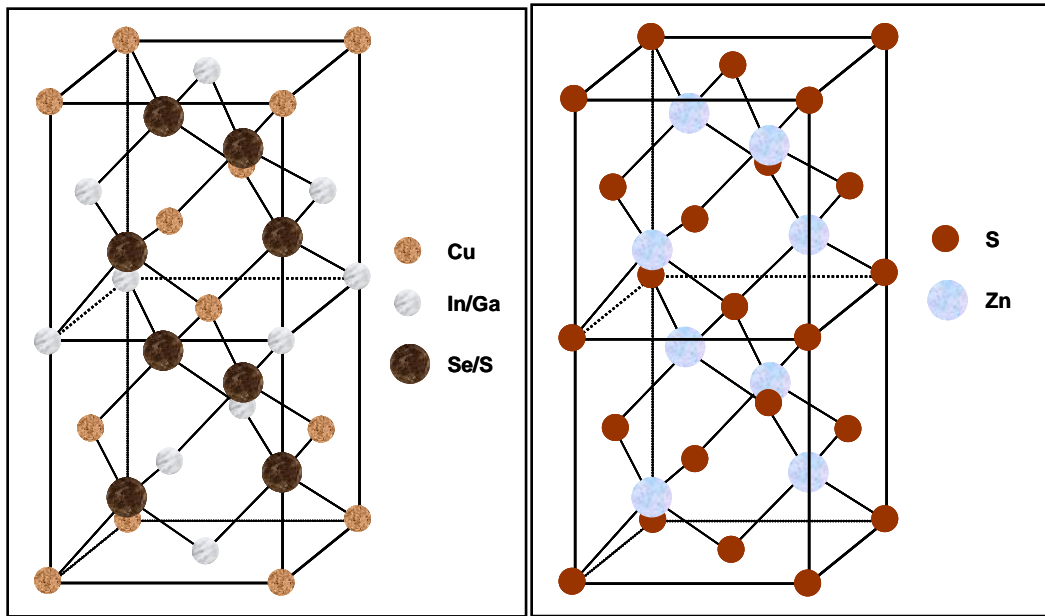
Figure 19(a) CIGS chalcopyrite crystal structure and (b) the equivalent ZnS structure

The tetragonal structure of CIS is equivalent to two FCC structures one stacked on top of the other. The growth plane in FCC structure is typically (111) which is the close packed plane. The equivalent close packed plane in chalcopyrites is (112).

3.3.4 Phase Diagram

$CuInSe_2$ alloy system has one of the most complex phase diagrams when compared with all the other thin-film solar cell materials. All the possible phases in the $CuInSe_2$ alloy system are indicated in the ternary phase at 500 ºC (Figure 20). $CuInSe_2$ absorber prepared under excess selenium has composition that fall on or close to the tie line between Cu_2Se and In_2Se_3. Along with the chalcopyrite $CuInSe_2$, the ordered defect compounds (ODC) viz., $Cu_3In_5Se_9$, $Cu_2In_4Se_7$, $CuIn_3Se_5$ and $CuIn_5Se_8$ also lie on the tie line. The ODC compounds have the same chalcopyrite

structure as CuInSe$_2$ [17]. The complex ternary diagram can be reduced to a simpler pseudo binary phase diagram (Figure 21) along the tie line.
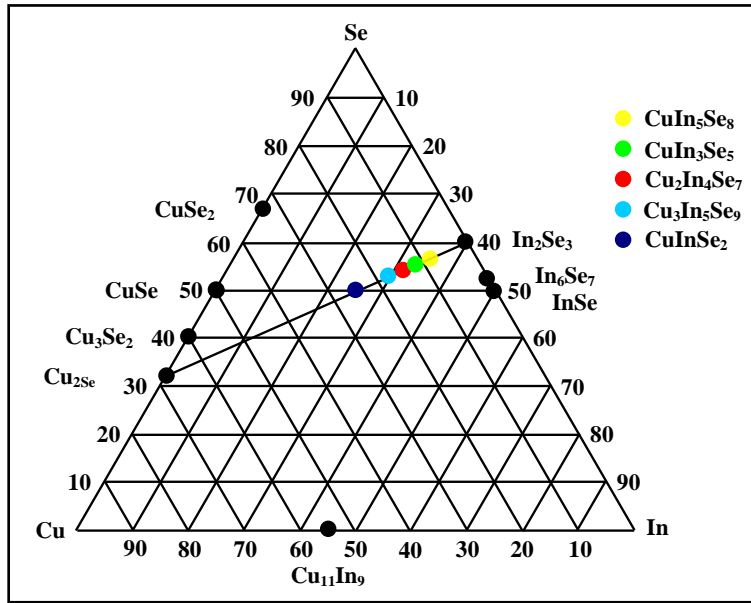
Figure 20 Ternary Phase Diagram of the Cu-In-Se Alloy (Redrawn)

In the pseudo binary phase diagram, α = CuInSe$_2$, β = CuIn$_3$Se$_5$, γ = CuIn$_5$Se$_8$, and δ = high temperature phase with sphalerite structure. As seen from pseudo binary phase diagram, the α phase exists at copper concentration between 24–24.5 at. % at room temperature. The existence of α phase is over a very narrow composition range and does not even include the stoichiometric composition of 25 at.% Cu. Typically the copper content in the thin film absorber is 22-24 at. %.
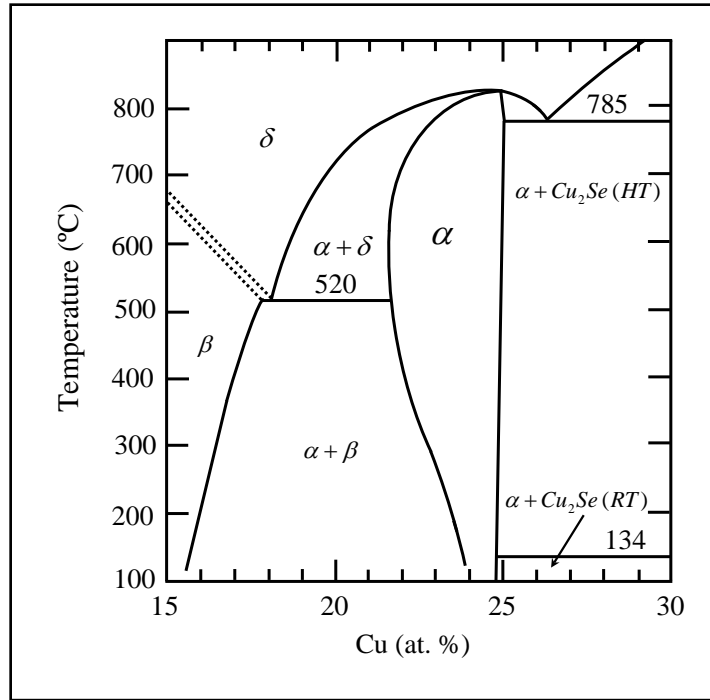
Figure 21 Pseudobinary In_2Se_3–Cu_2Se equilibrium phase diagram for compositions around the CuInSe2 chalcopyrite phase (Redrawn) [18].

The α or CuInSe$_2$ phase exists between 22 -24.5 at.% Cu at the growth temperature of 500 – 550 ℃. At room temperature, both CuInSe$_2$ and CuIn$_3$Se$_5$ phases exist at 22-24.5 at.% Cu. The β or CuIn3Se5 phase evolves due to the creation of copper vacancies (V_{Cu}) and indium on copper sites (In_{Cu}). Therefore, the phases are also termed ordered vacancy compounds. The β phase has a bandgap of 1.23 [19] -1.3 [20] eV. Higher bandgap at the junction will help increase the V_{oc} [21]. However, some groups have reported that the β phase is weakly n-type [22]. The surface layer is weakly n-type and the bulk of the material is p-type, thus they form a buried p-n junction [23-24]. The inverted surface helps in reducing the recombination at the metallurgical interface with CdS. The thickness of the ODC layer depends upon the copper content in the film. ODC layer thickness varies inversely with copper content in the absorber [25].

31

Partial replacement of indium by gallium and by addition of sodium actively or passively widens the α phase thus making it possible to have single phase (α phase) region between 22-24.5 at.% Cu at room temperature [26]. It is evident from the phase diagram that the $CuInSe_2$ phase exists over a range of copper-poor compositions at growth temperature of ~500 °C. If the absorber is prepared in a copper-rich regime, Cu_2Se phase forms. The Cu_2Se phase is highly conductive. The presence of this phase diminishes the performance of the solar cell. The presence of any trace amount of this phase can degrade the cell performance and therefore, it must be removed by etching with 10% KCN solution.

3.3.5 Absorber Preparation Techniques

A wide variety of techniques have been used to fabricate CIS thin film absorbers. These include, three-source evaporation [27-30], selenization (sulfurization) of sputtered metallic precursors (termed sputtering for the sake of brevity) [31], flash evaporation, laser ablation [32], vapor transport [33], spray pyrolysis [34-36], liquid phase epitaxy [37-38], electro-deposition [39-40], screen printing [41] and selenization of metallic layers [42-45]. Among the several techniques mentioned above, coevaporation and sputtering are the most promising. Sputtering is an established process for very high-throughput manufacturing. ARCO Solar, later Shell Solar pioneered the CIS preparation using the sputtering technique [46]. The two-stage process developed by ARCO Solar consisted of sputtering of a copper and indium layers on Mo-coated sodalime glass at first step. In the second step, the deposited copper-indium layers were exposed to selenium-bearing gas ambient of hydrogen selenide (H_2Se) mixed with argon. The hydrogen selenide dissociates and provides selenium, which reacts and mixes with the copper and indium

to produce high-quality CIS absorber layer. Sputtering technology has the added advantage of being easily scalable and adaptable to roll-to-roll production on flexible substrates.

In the early 90's, a low toxic selenization process was developed at the FSEC's PV Materials Laboratory to avoid use of highly toxic H_2Se gas. The two stage selenization process involved deposition of a copper-indium layer with excess copper. The elemental stack was selenized by annealing in the presence of selenium vapors obtained by thermally evaporating elemental selenium. Selenization of the copper-rich film improved the absorber adhesion with the molybdenum back contact. Indium was deposited on the copper-rich film to make it copper-poor and re-selenized to produce an efficient thin-film CIS absorber [47]. The process was later modified by gallium addition to achieve a cell efficiency of 9.02% [48]. Currently, CIGSeS absorbers are being prepared by rapid thermal processing of metallic precursor films with elemental selenium and conventional furnace annealing in selenium vapor obtained from diethylselenide (DESe) or other organometallic precursors [49]. Sulfurization of the selenized film to form CIGSeS and of metallic precursors to form $CuIn_{1-x}Ga_xS_2$ (CIGS2) is carried out in diluted H_2S gas [50]. Till date, in FSEC's photovoltaic materials laboratory, an efficiency of 13.73% has been obtained on a CIGSeS absorber layer prepared using diethylselenide as a selenium source [51]. Research activities in FSEC photovoltaic materials laboratory on CIGS2 thin-film solar cells resulted in an efficiency of 11.99% [52].

3.3.6 Doping in CIGS Absorbers

The most important characteristics of CIGS material is accommodation of a large amount of compositional variation without appreciable change in the electronic properties. Highly

33

efficient solar cells can be fabricated with Cu/(In+Ga) ratio of 0.7 to slightly less than 1. This phenomenon can be explained on the basis of defect chemistry of CIS. It has been shown that the formation energy of defects such as copper vacancies V_{Cu} and defect complexes $2V_{Cu}+In_{Cu}$ is low [53]. V_{Cu} is a shallow acceptor that contributes to the p-type conductivity of CIGS. The $2V_{Cu}+In_{Cu}$ defect prevents degenerate doping in indium-rich material. Isolated In_{Cu} acts as a deep donor while the combination with $2V_{Cu}$ has no deep level and is electrically neutral. Because of a high amount of $2V_{Cu}+In_{Cu}$ complexes, they interact with each other and further reduce the formation energy.

Thus the creation of such defect complexes can compensate for Cu-poor/In-rich composition of CIGS without adverse effects on photovoltaic properties. Doping of the CIGS semiconductor is controlled by intrinsic defects. Samples with p-type conductivity are grown if the material is copper poor and annealed under high Se vapor pressure, whereas Cu-rich material with Se deficiency tends to be n-type [54-55]. Thus Se vacancy (V_{Se}) is considered to be the dominant donor in n-type CIGS and also compensating donor in p-type CIGS whereas V_{Cu} is dominant acceptor in Cu-poor p-type material. Cu-poor material has In_{Cu} antisite donor defects along with V_{Cu} acceptors, resulting in heavily compensated n or p-type material. In the case of excess Cu, dominant defects are Cu_{In} antisite and In vacancy (V_{In}) acceptors, both of which contribute to a strongly p-type material. On the other hand Cu-rich material with Se deficiency tends to be n-type. Thus Se vacancy is considered to be dominant donor in n-type material.

3.3.7 Effect of Sodium on Absorber Preparation

Several beneficial effects of sodium in copper chalcopyrite thin-film solar cells are reported in the literature. It has been shown that the presence of sodium plays a very critical role during the growth of CIGS absorber layer and is beneficial for the device performance. Several sodium precursors have been explored to determine their effect on the growth of CIGS solar cells. Among those studied, sodium fluoride (NaF) has been found to be the best choice. This is because NaF is non-hygroscopic, stable in air and evaporates stoichiometrically [56]. It has been shown that selenization of the film containing sodium results in the formation of $NaSe_x$ compounds that delay the growth kinetics of the CIGS phase for better incorporation of selenium in the film [57]. Sodium has a tendency to reduce detrimental point defects. It reduces compensating donors by substituting selenium vacancies V_{se} and therefore increases the p-type conductivity.

Sodium also replaces In_{Cu} anti-site defects further reducing the compensating donors [58]. Apart from reducing the compensating donor, sodium also replaces copper vacancies thereby minimizing the formation of ordered defect compounds (ODC) and thus favors widening the α-phase region. Sodium also promotes increase in grain size and preferred (112) orientation of CIGS films [59-61]. Sodium has also been shown to passivate the surface and grain boundaries of CIGS films by promoting oxygen incorporation [57]. The overall effect of sodium on the device performance is noted by an increase in efficiency by improvement in fill factor and open circuit voltage. Addition of sodium helps in fabricating Cu-poor films with higher device efficiencies without a KCN treatment.

It has been shown that the optimum amount of sodium for better device performance is determined by the process used to prepare the absorbers films [61]. Therefore, films prepared by RTA will need higher amount of sodium compared to films synthesized in conventional furnaces with slower temperature ramp rates.

The highest efficiencies of CIGS thin-film solar cells have been achieved by using soda-lime glass as substrate material. Soda-lime glass contains significant amounts of sodium in the form of 13-15% Na_2O. The sodium from the substrate diffuses through the Mo back contact into the absorber. In order to ensure uniformity in sodium incorporation, the preferred technique is to use alkali barriers between the soda-lime glass and molybdenum back contact and deposit a known quantity of sodium, traditionally, by thermal evaporation of sodium precursor on molybdenum before the absorber growth [62-63]. However, for large area substrates the uniformity in Na deposition will still be compromised and this method of sodium incorporation adds another step in the process rendering it unsuitable for large volume production. Different methods have been tried to minimize this problem. In a recent study by Shogo et al, soda-lime glass thin-film deposited by rf-magnetron sputtering was used as sodium source for controlled incorporation of Na in CIGS films grown on flexible substrates [64]. The large area uniformity of deposited sodium is the noted advantage of this technique compared to the sodium deposited by traditional thermal evaporation.

In recent years an alternative technique has been developed wherein sodium doped molybdenum back contact has been explored. In fact, efficiencies of 13.7% have been achieved on flexible titanium foils using this method [65]. It is possible to control the optimum amount of sodium by sputtering a layer of know thickness from such a target. In an in-line manufacturing

set-up, this technique would eliminate the need for additional deposition for sodium precursor thus contributing to saving in terms of time and cost for the additional equipments. The benefits of this method are being realized to the point that companies like Plansee are already producing standard (3, 5, and 10 at. % Na) and custom made sodium doped molybdenum targets know commercially as MoNa. This technique is very suitable on a production scale for large areas and would eliminate the additional step for deposition of sodium precursor. However, this can only provide sodium at the back.

3.3.8 Back Contact to CIGS Solar Cells

A suitable back contact for CIGS solar cells must satisfy various requirements. Therefore, several metallic back contacts have been explored. Various parameters need to be satisfied for a choice of high quality back contact layer for CIGS solar cells. This includes,

i.   Due to the highly reactive ambient and high temperatures (~500°C) during CIGS processing, the back contact must withstand such harsh conditions without degrading its properties.

ii. Conductivity and adherence to the substrate should also be maintained throughout the entire processing and also during the operating lifetime of solar cell.

iii. The back contact must also play a role as a barrier against impurity diffusion form the substrate into the absorber.

iv. It must possess a high optical reflectance in order to avoid optical losses.

Several metals have been explored such as Au, Pt, Ni, Al, Ag, Cu, W, Cr, Mo, Ta, V, Ti, Nb, Mn as back-contact material for CIS based thin-film solar cells [65-71]. Pt, Au, Ni, and Mo

all form fairly reproducible, low-resistance contacts to the CIS absorber layer. Mo and Ni contacts seem to improve with high-temperature treatment [72]. Au and Pt show considerable diffusion into the CIS layer when annealed at elevated temperatures [73]. Molybdenum is the most widely used back contact material because of its relative stability at the processing temperatures, resistance to alloying with Cu and In, and its low contact resistance to the absorber layer [74]. Among all these materials investigated, molybdenum is preferred back contact for it satisfied most of the requirements for an ideal back contact. Molybdenum is chemically stable and does not react with Cu, In, Ga or their alloys during the processing. It makes a good Ohmic contact with the CIGS absorber due to the formation of an intermediate $MoSe_2$ layer [75]. The highly efficient CIGS solar cells have been made with molybdenum as the back contact layer. A number of investigations have reported about the mechanical, optical, and electrical properties of Mo thin films deposited with DC magnetron sputtering technique [66].

It is a well understood that sputter-deposited refractory metal thin films have a correlation between working gas pressure, power and residual stress of the as-deposited film, [77-80]. It has also been demonstrated that the sputtering power influences the stress state of the molybdenum thin films. Other studies have reported that the adherence of the molybdenum thin films their conductivity is strongly dependent on the working gas pressures [79-82]. Molybdenum thin film can possess a variety of properties by varying the process parameters. For example, films deposited at low working gas pressures generally have a poor adherence to the substrate, high conductivity and compressive stress state, while those deposited at high gas pressures tend to have a good adherence, low conductivity and residual tensile stress. The influence of working

gas pressure on the electrical and mechanical properties of the molybdenum back contact layer has been reported along with their effect on the performance of the solar cells [81, 82, 84, 85].

The main factor which influences the adherence of the film to the substrate is residual stress. Bell *et al*. have reported a strong correlation between the stress state within a film to the working gas pressure and angle of incidence of sputtered atoms [86]. Similar results were also confirmed with the study conducted by Scofield *et al*. who showed that films in compressive stress state had poor adherence and those in tensile stress had good adherence with the substrate [66]. Shen reported that stress state in molybdenum films changes from highly compressive to highly tensile in a narrow pressure range of 8 to 10 mTorr [88], while, Hoffman *et al*. obtained this transition pressure at ~0.2 mTorr [78]. Shen also reported that the microstructure of the compressive films was densely packed microstructure while films with tensile stress had a very porous columnar microstructure.

Gordillo *et al*. showed that the electrical conductivity of sputter-deposited molybdenum thin film is highly influenced by both sputtering power and working gas pressure both of which influence the microstructure of the film [88]. Scofield *et al*. found that the resistivity of about $10\mu\Omega\cdot$cm was steadily obtained at pressures between 0.2 and 2 mTorr without significant pressure dependence followed by a steep increase at pressure of more than 2 mTorr [66].

3.3.9 Deposition of Heterojunction Partner Layer

Cadmium sulfide (CdS) has been well investigated as a heterojunction partner with CIS based absorbers and a variety of techniques have been explored to fabricate device quality films [C1]. CdS is a direct bandgap *n*-type semiconductor with a bandgap of ~2.42 eV. Due to its wide

band gap and transparency, CdS serves as a window layer with minimum light absorption. The lattice mismatch between the CdS and CIGSe interface is very small. CdS can also grow epitaxially on CIS surface [81]. Due to much higher carrier density in CdS compared to CIGS, major portion of the depletion region is in the CIGS film. Therefore, the recombination of minority carriers at the back contact is minimized.

During the initial development stages of CIGSe thin film solar cells, the heterojunction was formed by depositing a thicker CdS layer of approximately 1-3 μm by sputtering [89] or evaporation [39]. The temperature of the substrate during the evaporation process was maintained between room temperature and ~200 ℃. Bilayers of CdS consisting of a thicker low resistivity layer doped with indium [90] or gallium [91] and a thinner high resistivity layer were deposited by evaporation or chemical bath deposition (CBD). So far, thin CdS layer deposited by CBD is the preferred technique for CIGS thin films solar cells.

If the thickness of CdS is more than the optimum, it absorbs some portion of high energy photons and therefore, decreases the short circuit current. The photon absorption can be minimized with an optimum thickness of ~50 nm. Too thin CdS layer or its absence can lead to an increase in the recombination in the space charge region of the absorber layer. This results in a reduction of open-circuit voltage, fill-factor and spectral response. In chemical bath deposition, the growth of CdS film occurs either by the reaction between the constituent ions or by clustering of colloidal particles [92]. CdS layer protects the junction against mechanical and chemical damages during the deposition of the subsequent ZnO layer.

The benefits of depositing CdS layer by CBD are described as follows:

i. CdS layer deposited by CBD provides complete coverage of the uneven absorber layer surface as compared to deposition by evaporation at very low thickness.

ii. The Cd^+ may also diffuse into the Cu poor surface layer of the absorber layer and occupy the Cu sites. This helps in reducing the acceptor defect density and thus causing a consequent type inversion. This type inversion might result in a buried homojunction. The diffusion of Cd^+ into the CIGSe layers also depends on the orientation of the CIGSe layer. (220/204) oriented CIGSe layers allow more Cd^+ diffusion into the CIGSe layer.

iii. During the CBD process ammonia removes the native oxides. The absorber surface is thus cleaned which enables the epitaxial growth of CdS layer.

iv. Sodium present at the CIGSe/CdS interface may affect the junction properties. CdS deposition by CBD may wash away the traces of sodium present on the absorber surface.

The limitations of CdS layer deposited by CBD are described as follows:

i. Large amount of toxic hazardous waste is generated during the CBD process.

ii. Being a wet process it cannot be incorporated within an in-line fabrication set-up.

iii. Yield is very low.

iv. The bandgap of CdS restricts the photons from the blue region to reach the absorber.

Due to the above mentioned disadvantages researchers are investigating other options to replace CdS as the heterojunction partner. However, it is difficult to find a replacement with

similar properties due to the beneficial chemistry of the CBD process and favorable properties of CBD CdS layer as a heterojunction partner.

The deposition of CdS by CBD is usually carried out with the following constituents:

1. Cadmium precursor: $CdSO_4$[93], $CdCl_2$ [94], CdI_2, or $Cd(CH_3COO)_2$ [95]

2. Sulfur precursor: Thiourea $(SC(NH_2)_2)$

3. Complexing agent : NH_4OH

The complexing agent NH_4OH slows down the reaction and also avoids the formation of $Cd(OH)_2$. The concentration of thiourea is maintained higher than that of the metal precursor. The optimum temperature range for CdS deposition is between 60 – 90 ºC where thiourea hydrolyzes and decomposes to release S^{2-} anions. The total reaction for the formation of CdS is given as:

$$Cd(NH3)_4^{2+} + SC(NH_2)_2 + 2OH^- \rightarrow CdS + H_2NCN + 4NH_3 + 2H_2O$$
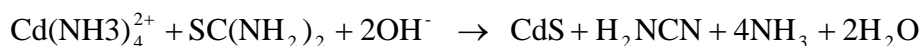
3.3.10 Transparent and Conducting Front Contact Layer

The front contact layer in the CIGSe based thin film solar cell should meet the following requirements;

i. It must provide high transparency (>85%) so as to let most of the light pass through it.

42

ii.   It must have low sheet resistance ~60 $\Omega/\square$ or less so that it can transport all the photogenerated current to the current collection grid without significant resistive losses.

The early generation CuInGaSe$_2$ based thin film solar cell used CdS doped with In [90] or Ga [96] as front contact layers in addition to the CdS buffer layer. The bandgap of these layer was ~2.42 eV. The entire short wavelength light (<520 nm) was absorbed by the thick CdS layer that resulted in reduction of the total photogenerated current. Deposition of CdS layer by CBD allowed the layer to be very thin. This minimized the absorption of short wavelength photons and also enabled the use front contact layer with higher bandgap so as to transport the photocurrent efficiently.

The materials which could satisfy the above criteria included ZnO, SnO$_2$:In (ITO) and SnO$_2$. The deposition of SnO$_2$ is carried out at 350-750 °C. After the deposition of CdS layer CIGSe devices cannot tolerate temperatures > 200 to 250 °C. The cost of ZnO is much lower compared to ITO. Hence ZnO is being used as the front contact layer.

The present day devices use oxide bilayers consisting

(i)   ~50 nm thick highly resistive layer and

(ii)   200 – 500 nm thick highly conductive layer.

Together with CdS, the highly resistive undoped ZnO (*i*:ZnO) layer protects the device from electrical losses due to the inhomogenities present in the absorber. Moreover, the *i*:ZnO layer prevents the diffusion of aluminum from the highly conductive ZnO:Al layer into absorber layers. *i*:ZnO layer also protects the interface layer from sputter damage induced during the deposition of the ZnO:Al layer which typically involves high energy sputtered species. The

thickness of the *i*:ZnO layer is also critical from the device performance point of view. If the thickness of the *i*:ZnO below the optimum thickness then it may lead to the increase in the leakage currents. However, if the layer is too thick it will decrease the current density due to an increase in the series resistance. i:ZnO layer greatly influences the open circuit voltage, V_{oc} [97].

Doped zinc oxide films have several attractive properties such as high conductivity, high (3.3 eV) bandgap making it highly transparent in the visible region and has high reflectance for infrared radiation. The low electrical resistivity of the transparent conductive oxide films is due to the presence of intrinsic defects, i.e. oxygen vacancies (V_O) and zinc interstitials (Zn_i) which act as shallow n-type donors [98-99]. Low resistivity films can be obtained by introducing charge carriers into ZnO by extrinsic doping with group III elements such as aluminum [], boron [100] or gallium [101]. Aluminum belongs to group III and Zinc belongs to the group II elements. When ZnO is doped with Al, Al atoms replace Zn atoms and act as donors. The amount of aluminum doping in ZnO can vary from 0.1 wt. % – 2 wt. % [102]. The properties of the highly conductive layers vary with the amount of doping and also the process gases. Various techniques have used for deposition of doped ZnO layer, viz., DC and RF magnetron sputtering [103], chemical vapor deposition [104], reactive DC sputtering, sol-gel techniques [105], atomic layer epitaxy [106] MOCVD, and laser ablation [107]. However, RF magnetron sputtering technique is the preferred choice due to higher deposition rates, very good thickness uniformity and high density of the films, relatively cheap deposition method and scalability to large areas.

3.4 Kesterites

Despite the promise of current thin-film technologies, both CdTe and CIGS rely on relatively rare and toxic elements. As production of these PV technologies increases, there is a concern for the amount of indium (In) and tellurium (Te) available and for how this scarcity could adversely affect production costs. A more abundant and environmentally benign absorber is needed in order to ensure a competitive and stable thin film PV market.

Because of these concerns, there has been a shift in research to the kesterite-related family of material, specifically $Cu_2ZnSn(S,Se)_4$(CZTS). This material involves earth abundant elements, while also meeting the requirements necessary to construct a successful solar energy device. The kesterite crystal structure is similar to the chalcopyrite type structure seen in CIGS, where every trivalent group III atom (In and Ga) are replaced with equal number of divalent group II and tetravalent group IV metals (Zn and Sn) [108]. Currently the record 9.7 % efficient cell has been developed using a liquid based deposition process[109], while only a maximum of 6.8% efficient cells have been produced using vacuum deposition techniques[110]. According to the literature there is a large gap in the fundamental understanding of this technology which results in the relatively low cell performance parameters. A more thorough knowledge base will eventually lead to improvement in cell efficiencies.

Current research focuses on the (a) the deposition process of precursor materials and subsequent annealing process, (b) the micro-structure and composition of CZTS absorber layer (c) the electronic and optical properties of the CZTS absorber layer as well as (d) the structure and properties of the interfaces between the CZTS and the Molybdenum back contact as well as the n-type heterojunction partner layer.

Various routes have been explored in an attempt to produce high quality CZTS films. The most successful has been a recent approach using a hybrid solution-particle based deposition approach [109]. A hydrazine solution containing dispersed solid particle precursors has been spin coated on a substrate and annealed to form single phase CZTS. Although the deposition method produces a fairly thin layer, the process can be performed multiple times in order to produce the appropriate layer thickness. This is an interesting approach because of its potential application in high throughput printing or coating methods that are currently employed in other electronic manufacturing industries. There has also been some success in the use of sputtered stacked metal precursors annealed in a Sulfur or Selenium atmosphere to produce high quality CZTS [111-113]. This is a similar process used to produce high quality CIGS absorber layers, and is the current method of fabrication within the industry. Efficiencies up to 6.7% have been produced with this approach [113]. As also seen in the CIGS cell production the most successful vacuum approach to fabricate CZTS cells has utilized co-evaporation techniques [110]. This has produced only slightly better conversion efficiencies of 6.8%. There is much work remaining in the optimization process of these techniques in order to produce the highest quality devices.

The morphology of the CZTS layer also remains to be fully optimized for cell production. A similar trend of higher processing temperature leading to larger sized grains is what has previously been seen in CIGS absorber layers. However, these larger grains are not necessarily associated with the highest conversion efficiencies. This is due to a number of factors. A segregation of ZnSe has been seen in conjunction with these higher temperatures [2]. This along with the formation of a MoS_2 or $MoSe_2$ phase along the interface at the back contact leads to higher recombination rates and higher series resistances. This will result in low fill

factors and cell efficiencies. There are models using pseudo J-V curves constructed using already achieved open circuit voltages and similar series resistances obtained in CIGS cells that predict conversion efficiencies above 11% [108]. If the issue of higher series resistances and recombination losses can be overcome, there will be a large increase in conversion efficiencies.

The overall band structure over the completed diode has not been studied well. There has been speculation of surface recombination effects at the heterojunction interface limiting the open circuit voltage (V_{oc}) [108]. A mismatch in conduction band alignment where the absorber layer conduction band edge is higher than that of the buffer layer is believed to be the cause of this interface recombination. Improvement in the matching of an appropriate heterojunction partner along with an optimized absorber synthesis method could also lead to increased cell efficiencies.

There is hope that the next generation of thin film solar cells will consist of earth abundant and non-toxic materials. Kesterite based cells already meet these requirements and have shown promise in their ability to produce conversion efficiencies that might rival the previously successful technologies of CdTe and CIGS. However, the limited knowledge base available for the CZTS technology will limit any large scale production from taking place. Through further research and a better understanding of the fundamentals behind this technology, there is a possibility of highly efficient and very cost effective technology to emerge in the thin film PV market.

3.5 Cadmium-Free Solar Cells

Champion CIGS thin film solar cells are currently prepared with a n-type heterojunction partner CdS layer along with an intrinsic ZnO buffer layer. There has been significant research in the development of an alternate to a cadmium based layer for several reasons, mainly from the desire to decrease the environmental impact by using a less toxic chemical. Other motivations include the possibility to increase the transmission of higher energy photons below 550 nm, to optimize the conduction band offset at the CIGS/CdS interface, and to remove the wet-chemical deposition procedure to allow for a more efficient in-line manufacturing process. One very promising candidate is the ZnMgO alloy. Various reports of CIGS devices that incorporate a ZnMgO layer (sometimes in conjunction with another layer such as ZnS) have demonstrated comparable or superior performance with devices that include a classical CdS/ZnO buffer layer [115-117].

A single $Zn_{1-x}Mg_xO$ layer can be used to replace just the ZnO window layer or both the CdS and ZnO layers. This is such a versatile material because of the precise adjustments of the optical and electronic properties made possible through the control of the Mg composition. The band gap energy along with the transmission spectra can be effectively controlled by adjusting the composition of a $Zn_{1-x}Mg_xO$ thin film [118], as well as the conduction band offset when used in a device [119]. Through control of these material properties, there are a number of functions that this material can perform. Furthermore, this layer can perform multiple functions simultaneously if a magnesium gradient is imposed [120].

As previously mentioned, it is also important for the material that replaces CdS to utilize a deposition method that can be implemented with minimal manufacturing cost while also

maintaining the integrity of the device. If the wet-chemical CdS deposition method can be replaced with a dry process such as RF sputtering, this will allow for a more efficient in-line manufacturing process. Currently thin film layers of ZnMgO have been deposited using RF sputtering with some success [117,120]. However, sputtering of the heterojunction partner can result in damages at the absorber surface that can cause an increase in interface recombination resulting in a decrease in the conversion efficiency. Therefore, special care of the deposition process and post treatment process need to be considered when completing this layer.

Therefore, ZnMgO remains a top choice in the possible replacements for a Cd-free buffer layer. However, additional research is needed to provide a recipe for successful use of ZnMgO in production of an efficient solar power conversion device. Advances in the utilization and understanding of a ZnMgO layer will greatly benefit the thin film PV market.

CHAPTER 4 EXPERIMENTAL

This section describes the experimental techniques used for the deposition of molybdenum back contact followed by development of CIGSeS and CIGS2 thin films solar cells on those contacts. Various materials and device characterization techniques used in this research have also been described briefly toward the end of this chapter.

4.1 Device Fabrication

4.1.1 Substrate Cleaning

Commercially available low cost, low iron sodalime float glass ~3 mm thick was the substrate of choice used in this research. Substrate cleaning is the most critical part of the device fabrication since a poorly cleaned interface between the substrate and the device can serve as a source of impurities and potential site for delamination either during processing or later.

(i) The sodalime glass substrate was cleaned using the 1% LiquiNox® soap solution prepared with deionized water. The glass substrate was immersed and allowed to stay in this soap solution for a period of one hour in the temperature range of 50-70 ℃ with continuous stirring of the solution. The substrate was rinsed thoroughly in running tap water to remove all traces of soap.

(ii) This was followed by ultrasonic cleaning in a bath of isopropyl alcohol for 30 minutes.

(iii) Finally the step (1) was repeated without using any soap with the deionized water. The substrate was dried using a jet of nitrogen gas.

4.1.2 Deposition of Alkali Diffusion Barrier

A thin barrier layer was deposited on the sodalime glass prior to the deposition of molybdenum back contact so as to minimize the diffusion of sodium from the sodalime glass during the absorber preparation. Several alkali barrier layers have been tried such as silicon nitride, silicon dioxide, aluminum oxide. However, the performance of silicon nitride as an alkali barrier has found to be better when compared to the other barriers [121]. Silicon nitride is deposited on sodalime glass using reactive radio frequency (RF) magnetron sputtering from a pure silicon target. Though targets of silicon nitride are available in the market, there are two reasons for not choosing them. First, the quality of films obtained is far better by reactive sputtering of pure silicon target compared to films deposited from compound targets of silicon nitride [122]. Second, the cost associated with pure silicon target is approximately one third of the cost associated with ceramic targets of silicon nitride.

The cleaned substrates were mounted in the vacuum chamber and were maintained overnight in high vacuum using a combination of mechanical, turbo molecular pump and cryopump to obtain a base pressure of $< 2\mathrm{x}10^{-6}$ Torr. Ultrahigh purity argon and nitrogen gas were introduced into the chamber using mass flow controllers and measured using convectron gauges. Depositions were carried out from a silicon target of dimensions 30 cm x 10 cm. The substrates were moved linearly along the width of the target using a LabVIEW$^{©}$ controlled stepper motor. The substrate movement was controlled to deposit films with a nominal thickness of approximately 800 – 1000 Å.

4.1.3 Molybdenum Back Contact Deposition

Molybdenum is one of the most suitable materials used as back contact for CIS based thin film solar cells. As mentioned before, the properties of molybdenum films depend strongly on the target–substrate distance, the power and the argon pressure during deposition. Molybdenum back contact was deposited by DC magnetron sputtering in a vacuum chamber with base pressure of $< 2 \times 10^{-6}$ Torr using a combination of a mechanical, turbo and a cryopump (pumping rate 1500 liters/sec). Depositions were carried out from a molybdenum target of dimensions 30 cm x 10 cm. The substrates were moved linearly along the width of the target with the help of a LabVIEW© controlled stepper motor. The thickness variation was in the range of $\pm$ 2.5% along the 30 cm length of the target. A total of four layers, viz., two compressive and two tensile were deposited. The first and the third layers were deposited under high argon pressure so as to achieve tensile films. The second and the fourth layers were deposited under low argon pressure and high power. These layers were compressive in nature. The total thickness of the resulting molybdenum back contact layer was ~0.7 μm. Also, recipe for single layer of molybdenum back contact has been developed with the details provided in the results and discussion section.

4.1.4 Deposition of Sodium Precursor

As mentioned earlier (Section 3.3.7) various compounds can be used as sodium precursors. Among the available sodium precursors, NaF is stable in air, non-hygroscopic and evaporates congruently. Hence in this research, NaF was used as the sodium precursor. The substrates were allowed to cool in the sputtering chamber after the deposition of molybdenum

back contact. The substrates were then immediately moved to the evaporation chamber for deposition of the NaF. For some samples, NaF was deposited after the deposition of CuInGa metallic precursors on the molybdenum coated glass substrate. A combination of mechanical and diffusion pumps in conjunction with a liquid nitrogen trap was used to maintain high vacuum ($\sim 2 \times 10^{-5}$ Torr). There are several advantages of diffusion pump including low maintenance cost, low running cost, high pumping speed and reliability. The major disadvantage of diffusion pumps is the tendency for the oil vapors to backstream into the vacuum chamber. A liquid nitrogen trap was used to overcome backstreaming of the oil vapors.

The NaF layer was deposited by the thermal evaporation. The thickness of the NaF layer was varied between 40 Å to 80 Å. The distance between the substrate and the evaporation boat was maintained at ~18 cm. The power was adjusted so as to maintain the rate of evaporation (deposition) at ~1 Å per second. The total thickness and the deposition rates were measured with "Inficon XTC/2" thin-film deposition controller. After the deposition was over, the gate valve for diffusion pump was shut and the substrate was allowed to cool for ~2 hours before the samples were moved to the next processing station.

4.1.5 Deposition of Metallic Precursor

A two-stage process was used for the preparation of the absorber layer. The first step consists of the deposition of the CuGa-In metallic precursors. The glass substrates coated with silicon nitride/molybdenum/NaF were mounted in the sputtering chamber and maintained at high vacuum for overnight. The metallic precursors were deposited by DC magnetron sputtering. Since the melting point of gallium is 29.76 ℃, it is difficult to prepare a pure gallium target and

consequently to sputter from it. Hence, an alloy target of Cu-Ga (78 at. % Cu and 22 at.% Ga) was used. This concept was pioneered by the researcher at PV Material laboratory at FSEC [123]. Now it is being used over several places including leading companies. The indium precursor was deposited from 99.999% indium target. The layers were deposited in a stacking sequence. The idea underlying the selection of optimum stacking sequence has been elaborated in the results and discussion section of this research work. The precursor deposition was started with CuGa as the first layer and ended with a very thin CuGa layer. The substrates were moved linearly along the width of the targets and the substrate movement rate was optimized so as to achieve the desired film thickness. All targets are of same size. The deposition of CuGa was normally carried out at a sputtering power of 350 W and argon pressure of 1.5 mTorr and the indium was deposited at sputtering power of 180 W and argon pressure of 0.7 mTorr. The deposition parameters were optimized so as to obtain either copper-rich or copper-poor absorbers.

4.1.6 Preparation of Absorber Layer

A large three-zone conventional furnace was utilized for the preparation of CIGSeS absorbers. The furnace includes a gold coated mirror for insulation. The mirror helps to maintain uniform temperature along the entire length of the furnace. A quartz tube is placed coaxially within the gold coated tube. The quartz tube is used to keep the mirror clean from any deposits. The heating element coil fits in between the quartz tube and the gold coated infrared reflector furnace. Each end of the gold mirror furnace is supported at two ends by ceramic block. A metal

flange with a high temperature compatible O-ring is used to seal the open end of the quartz tube during the process.

The precursor films are homogenized and the required amount of an organometallic selenium precursor is introduced in the furnace. The selenization process was carried out in organometallic selenium precursor vapor diluted in pure hydrogen or in the forming gas prepared by mixing N_2 and H_2. The selenization process was carried out in the temperature range of 450 ºC – 550 ºC for 30-60 minutes. After the selenization process all the remnants of the reaction products were exhausted and refilled with H_2S diluted with nitrogen gas to carry out the sulfurization process. The sulfurization process was carried out at 500 ºC with 5-10 minutes dwell period. The process gases were evacuated from the chamber and it was finally filled with ultra-high purity UHP nitrogen during cool down.

The CIGS2 absorber on the other hand were prepared in a Lindberg three zone tubular furnace with a continuous flow of dilute (~8-10%) H_2S gas in nitrogen at temperatures of 475-500 ºC. The gases were exhausted through a scrubber consisting of multiple bubbling columns containing highly concentrated NaOH solution for eliminating the H_2S gas before venting the contents to the atmosphere.

4.1.7 Deposition of CdS Heterojunction Partner Layer

Chemical bath deposition (CBD) was used in this research for the deposition of the cadmium sulfide (CdS) heterojunction partner layer. The CdS deposition was carried out in an alkaline aqueous solution with pH >9. The main ingredients that were used in the CBD process

included, ammonium hydroxide (NH$_4$OH), cadmium sulfate octahydrate (3Cd.3O4S.8H$_2$O) and thiourea (SC(NH$_2$)$_2$).

The aqueous stock solutions of all the ingredients with required concentrations were prepared separately. At first, the absorber samples were treated with a dilute KCN solution to etch away any trace amounts of Cu$_{2-x}$(Se,S)$_X$ phase. The samples were thoroughly flushed with deionized water so as to remove the traces of KCN solution. The flushings were stored under hazardous waste category. The thiourea solution was filtered so as to remove any undissolved particulates that may act as nucleation sites. The solution of deionized water together with NH$_4$OH, CdSO$_4$, and SC(NH$_2$)$_2$ were mixed and the sample was immediately transferred into this mixture. The temperature of the water bath was maintained at ~65 ℃. The beaker was then placed in the water bath and stirring was initiated using a magnetic stirrer. After 7-8 minutes the CdS solution attained ~60 ℃. The samples were taken out of CdS solution after 15 minutes. The color of the sample became bluish purple. The samples were cleaned with deionized water so as to remove any particulates of CdS from the surface. Finally, the samples were thoroughly dried using a gas jet of nitrogen.

4.1.8 Deposition of Transparent Conducting Oxide (TCO) Layer

i:ZnO and ZnO:Al TCO bilayers were deposited using RF magnetron sputtering. The ZnO:Al target of 99.995% purity contained ~2 wt.% Al$_2$O$_3$. After the deposition of the CdS layer the samples were mounted into the vacuum chamber for TCO deposition. A reference glass sample was always mounted along with the CIGS samples so as to measure the transparency and

sheet resistance during every deposition. The optical transmittance of the i-ZnO/ZnO:Al bilayers was measured using "*Shimadzu UV-2401PC*" spectrophotometer.

A combination of mechanical pump, turbo molecular pump and cryopump (pumping speed 800 liters/sec) was used to achieve a base pressure of ~$2x10^{-6}$ Torr. The samples were maintained overnight in high vacuum. This process also aids in degassing the chamber walls and to reduce the water vapor content from the chamber. Each target was presputtered for ~25 minutes so as to remove any undesired contaminants from their surface. A thin (~50 nm) layer of *i*:ZnO was deposited at a RF power of 200 W and Ar pressure of 1.5 mTorr. This was followed by ZnO:Al layer of ~500 nm at RF power of 425 W and argon pressure of 1.0 mTorr. ZnO:Al film with a sheet resistance of 25-50 $\Omega/\square$ and transparency of >85% was routinely deposited using this process. After the deposition, the samples were allowed to cool for at least 1-2 hours before moving to the next chamber for the deposition of front contact fingers.

4.1.9 Deposition of Front Contact Grid

Thermal evaporation was used for the deposition of chromium/silver front contact fingers using a mechanical mask. Due to poor adhesion of silver to ZnO and to prevent the diffusion of silver into the ZnO:Al layer, initially, ~500 Å thick layer of chromium is deposited followed by the deposition of ~1.25 μm thick silver. The average deposition rate for chromium was ~2-5 Å per second. The power was optimized so as to maintain the rate of deposition for silver at ~10 – 20 Å per second. The total thickness and the rate of deposition were measured using "Inficon XTC/2" thin-film deposition controller. The metal mask allows to create contact grids for about 9 cells over a 2.5 cm x 5 cm substrate area with each cell area of approximately ~0.414 cm^2.

Figure 14 provides a schematic of the complete transverse cross-section of the CIGSeS thin film solar cell.
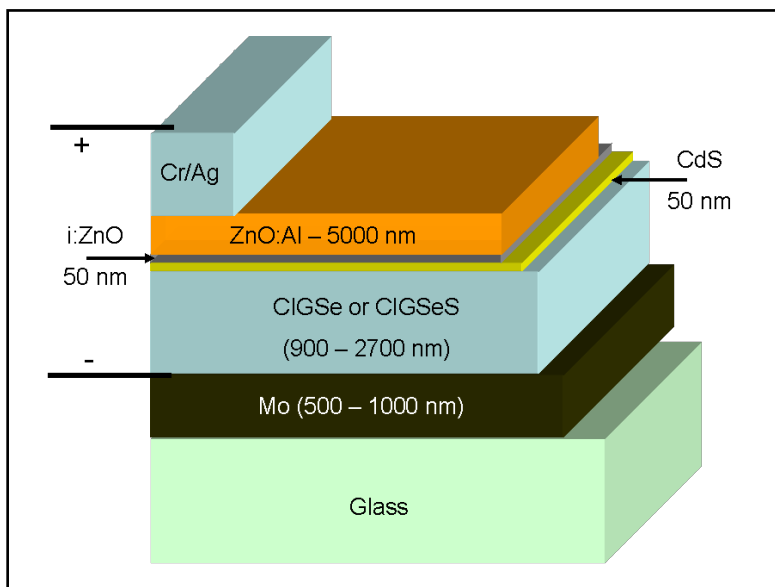
Figure 22 Structure of CIGSeS thin film solar cell

4.2 Characterization

4.2.1 Materials Characterization

Several characterization techniques were employed to study the materials properties and device characteristics. The sheet resistance of the absorber films was measured using a two-probe method to carry out a relative comparative assessment of conductivity from one experiment to the other. A **Dektak3** profilometer was used to measure the thicknesses of the various films that were deposited. Scanning electron microscopy (SEM) was carried out at the Materials Characterization Facility (MCF) of the UCF using **Zeiss ULTRA-55 FEG SEM** to study the surface morphology of the films and the cross sectional view to observe the lateral

grain growth. Chemical composition of the bulk of the film (precursors and absorber) was carried out by electron probe micro analysis (EPMA) and energy dispersive X-ray spectroscopy (EDS). The EPMA data used in this research work is a statistical average of data points from 10 different locations. EDS was carried out on Zeiss ULTRA-55 at MCF and EPMA analyses was carried out at NREL. The X-ray diffraction (XRD) measurements were carried out on **Rigaku D/MAX XRD** II with a thin film attachment using a 40 kV copper X-ray tube to analyze the crystallographic structures and phases. The lattice parameters, preferred orientation and the composition of the absorber films were estimated by studying the XRD peaks.

Electron Back Scattered Diffraction (EBSD) was carried out at NREL to analyze absorber films in order to provide orientation maps and to study misorientation between grains, grain size and their distribution.

4.2.2 Device Characterization

4.2.2.1 Current-Voltage (I-V) measurement

I-V characteristics of all the completed devices were carried out using an in-house fabricated I-V setup. The illumination was obtained using Newport solar simulator Model No. 91190-1000 with AM1.5 global filter. I-V measurements were carried out both in light and under dark conditions. I-V measurement under illumination provides important photovoltaic parameters such as open circuit voltage (V_{oc}), short circuit current density (J_{sc}), series resistance (R_s), shunt resistance (R_p), fill factor (FF) and efficiency (η). I-V measurement was also carried out in Dark to obtain the diode parameters such as, reverse saturation current density (J_0) and diode quality factor (A). Devices with efficiencies >10% were sent to NREL for authentication and certification.

4.2.3. Residual Stress Measurement

The residual stress was measured with the bending-beam method. Thin rectangular glass strip of 0.15 mm thickness, 1 cm $\times$ 15 cm was attached to the soda-lime glass substrate during every deposition. The nature of the bending in the glass strip can be either convex or concave depending on the stress state. Stoney derived the classic expression relating the radius of curvature of the deposited thin film, R to its internal residual stress, σ_i in case where the films are much thinner than the substrates [98].

$$\sigma_i = \frac{E_s t_s^2}{6(1-v)t_f} \left(\frac{1}{R} - \frac{1}{R_0} \right) \quad \dots\dots\dots\dots\dots\dots\dots\dots\dots\dots\dots\dots\dots\dots\dots\dots\dots\dots \text{ (11)}$$
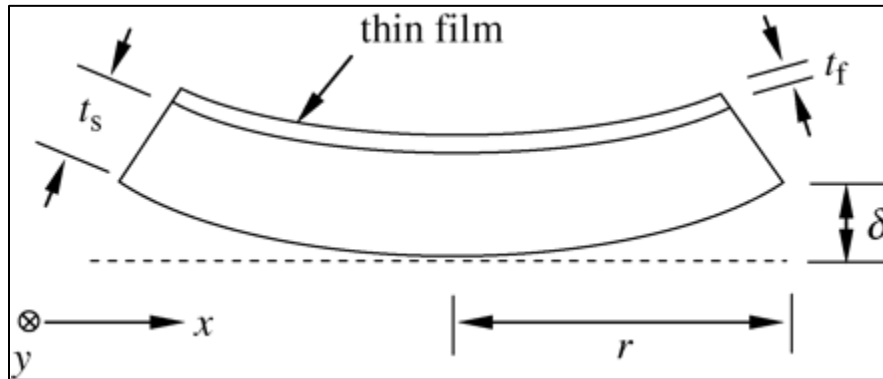
Figure 23 Schematic of a bent glass strip with a thin film deposited over it

Here, E_s is the Young's modulus of the strip, t_s is the thickness of the glass strip, t_f is the film thickness, v is Poisson's ratio of the glass strip, R and R_0 are the radii of the curvature of the

film after and before deposition respectively. Dividing equation by (1-v) considers that the stress

state within the film is biaxial. Therefore, Stoney's equation can be reformulated as,

$$S = \left[\frac{4E_s t_s{}^2}{3(1-v)L_0{}^2}\right] \times \left[\frac{\delta}{t_f}\right] \quad\text{.. (12)}$$

Here, S is the average stress, L_0 is the length of the glass strip, and δ is the deflection at the ends

of the glass strip as depicted in Figure 23.

CHAPTER 5 RESULTS AND DISCUSSIONS

5.1 Development of Single Layer Molybdenum Back Contact

A multi-pass processing is not desirable in high volume production because it prolongs total production time and correspondingly increases the manufacturing cost. In order to make manufacturing compliant with an in-line deposition, it is justifiable having minimum deposition sequences. The goal of this research was to develop a composite molybdenum back contact layer 1) that can be deposited in a single pass, 2) has good adhesion to sodalime glass 3) optimum conductivity 4) stable in the reactive ambient up to 550°C, the softening point of sodalime glass substrate.

As mentioned before, the properties of sputtered thin films such as resistivity, stress and structure are directly related to the incident energy of the sputtered atoms and the neutralized argon atoms. The incident energy in turn is dependent on the sputtering power, working gas pressure, working distance, angle of incidence and direction of incidence. During a single run, the sputtering power, working gas pressure, working distance remain the same. However, the angle and direction of incidence vary for each location on a substrate when the substrate is moving over the sputtering target with respect to the race track on the sputtering target from where the sputtered species (atoms, molecules, etc.) originate. Therefore, even under identical conditions of sputtering power, working gas pressure and working distance, the residual stress, resistivity, structure and morphology of the deposited film will be different at different locations on the substrate. The forthcoming results will validate this statement. Therefore, the film deposited after a single complete pass will actually be a composite structure.

5.1.1 Benefits of Choosing a Multilayer Structure for Back Contact

It is a well-established fact that optimum amount of sodium during the formation of CIGS absorber is beneficial for device performance. Sodium has several advantages in improving the absorber quality and several models have been proposed to explain this fact. Coincidently, soda lime glass which is the substrate of choice is a good source of sodium. To serve the purpose of being able to use the sodium from the glass substrate, a molybdenum layer with an open structure is desired. Films with open structure are obtained when they are sputtered under the condition of low sputtering power and high gas pressure. However, the films so obtained have high resistivity which is not desirable for a back contact. On the other hand, films sputtered at high sputtering power and low sputtering gas pressure have low resistivity but inherently suffer from poor adhesion to the glass substrate. Therefore, a multi-layered molybdenum back contact is deposited so as to achieve good adhesion to soda lime glass along with high conductivity. Moreover, the open films tend to be in tensile stress and the compact films tend to be in compressive stress. Therefore, stacking of these individual layers eventually minimizes the overall stress in the composite film.

5.1.2 Molybdenum Film Deposited by Other Research Groups

Cleaning of the glass substrate is a very critical step before deposition of the molybdenum film by magnetron sputtering. At the National Renewable Energy Laboratory (NREL), a very stringent cleaning procedure is adopted followed by very rapid drying process using a spin rinse drier. Any shortfall in the cleaning can result in water marks on the substrate surface that can lead to incorporation of impurities on the glass surface. These impurities can

63

eventually lead to poor adhesion of molybdenum film to the glass substrate. As a matter of fact, the molybdenum film used in the preparation of the >20% efficient CIGS solar cell was deposited at intermediate power and pressure in the range of 7-10 mTorr with the total thickness of the film being 1µm, deposited in two passes under similar conditions. The reason for choosing a double layer as opposed to a single layer of 1µm thickness is that the film deposited in single pass would peel-off. Other research groups have tried to add adsorbed gases to assist in the adhesion of the film to the substrate. At the Institute of Energy Conversion, University of Delaware, small amount of oxygen was added during molybdenum deposition. A research group in Japan is known to have added small amounts of water vapor during CIGS deposition to improve the performance of the devices. In this research the molybdenum films were deposited on sodalime glass substrate coated with an optimized barrier layer of $Si(O,N)_X / SiO_2$ in order to avoid out-diffusion of sodium from the soda-lime glass substrate to the absorber layer. A standard lab cleaning procedure was adopted for cleaning the glass substrates followed by blow drying in a jet of nitrogen gas as mentioned before.

5.1.3 Molybdenum Deposition with Moving Substrate

At the beginning of this experimental work, estimation of deposition rates was carried out for molybdenum target at various sputtering parameters of power and pressure. The working distance between the target and substrate was maintained at 90 mm. The results are summarized in Figure 24. It is desirable to achieve the highest deposition rates during sputtering. It can be seen that the highest deposition rates are obtained with increase in sputtering power and that the increase in sputtering rate with increase in the sputtering gas pressure is not much significant.

The sputtering power supply used in this research has a current limitation of 1A. Therefore, the deposition rates at higher power (>300 W) and gas pressures were not feasible due to corresponding increase in the discharge current that approached 1 A limiting value.

It has been shown that the deposition rate is a liner function of sputtering power. The results relate with the model suggested by Ekpe *et al* [124]. This model is based on the assumption that the flux of sputtered atoms to the substrate only consists of fast atoms and the thermalized atoms moving because of diffusion are neglected.
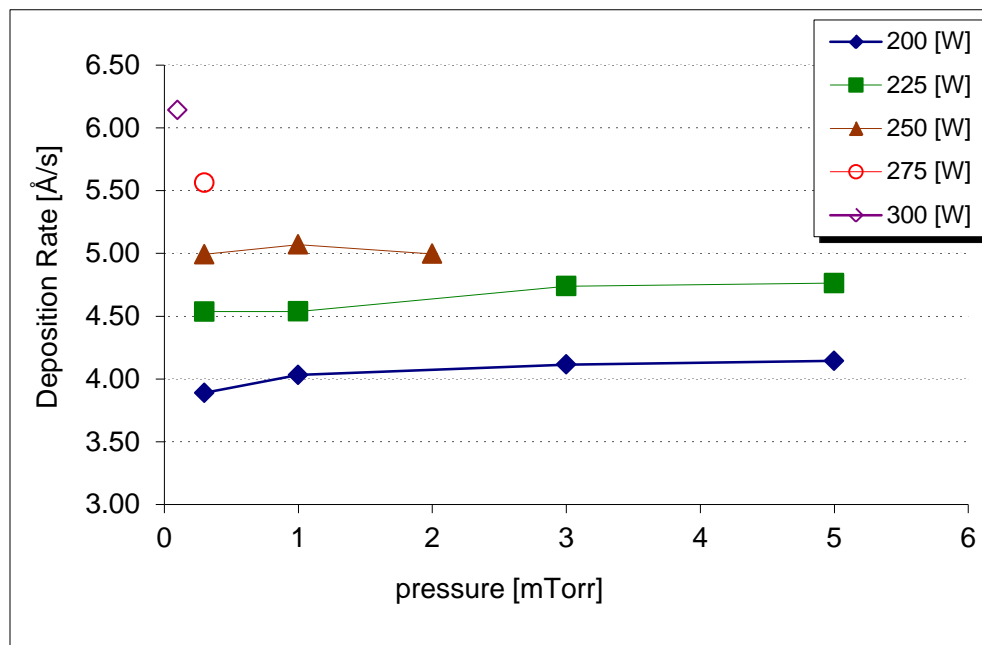
Figure 24 Molybdenum deposition rates obtained at various sputtering parameters

There are several advantages of **low pressure sputtering** and it is widely being adopted in the industry. It has been observed that the efficiency of target utilization strongly improves with decreasing the sputtering gas pressure [125]. Keeping this fact in mind, it was decided to

focus on the high power and low pressure regime to obtain the desired film types. Minimum incorporation of gaseous species/contamination takes place during film deposition and densities approaching bulk values are obtained. Being able to choose low pressure deposition parameters was a focus during this research. Resistivity measurement of deposited films was carried out in order to understand the relationship between sputtering parameters with the electrical properties. The detailed results are provided in the Figure 25. It is clear from the figure that working gas pressure plays a major role in the magnitude of resistivity as compared to sputtering power.
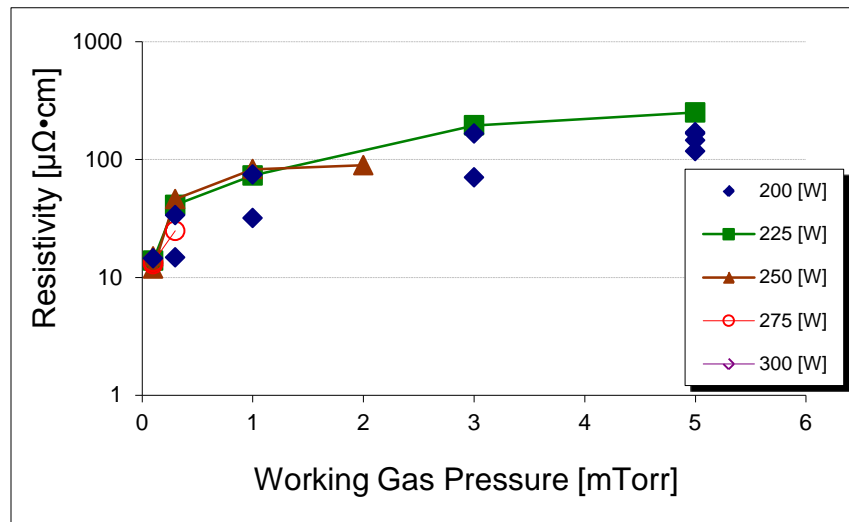
Figure 25 Variation of resistivity for molybdenum films deposited at various sputtering processing conditions

The resistivity values ranged between 13 $\mu\Omega$.cm (300 W/ 0.1mTorr) to 170 $\mu\Omega$.cm (200 W/ 5mTorr). The order of magnitude difference in resistivity has been discussed by several researchers based on the oxygen and argon content in the deposited films [126-127]. The

resistivity data comprises the combined effects of defects in the crystal and the presence of chemical impurities.
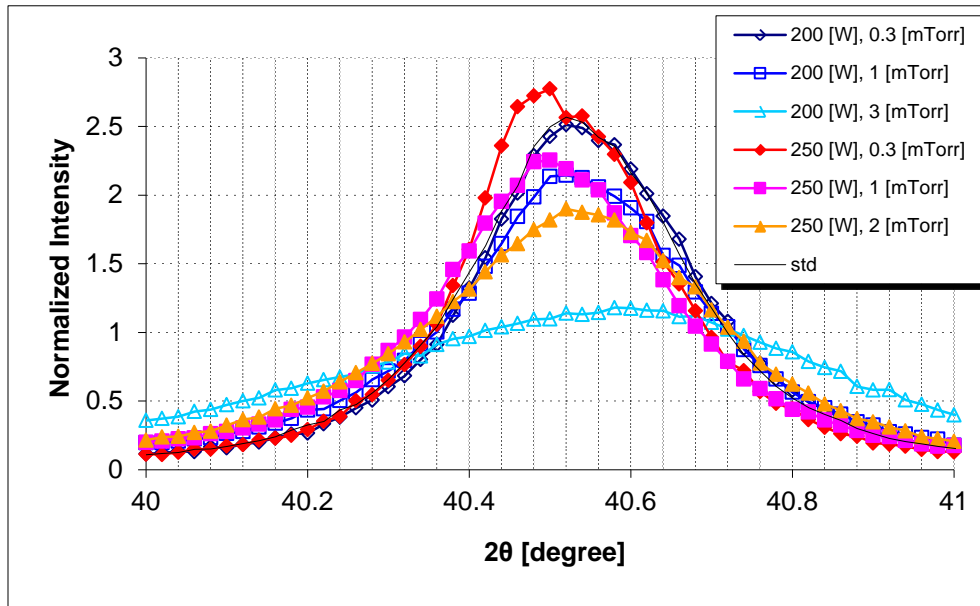
Figure 26 Comparison of (110) reflection for molybdenum films deposited at various sputtering processing conditions

Figure 26 shows the variation in peak intensity and peak broadening for the (110) reflection of the molybdenum film deposited at various sputtering conditions. It is evident here that higher sputtering power with low gas pressure favors the formation of highly crystalline film with (110) preferred orientation. Improved and defect free crystal structure corresponds with better electrical properties.

The next step was to determine the stress build-up in the deposited molybdenum films. The detailed procedure has been mentioned in the experimental section of this dissertation. The films were deposited on a 15 cm x 10 cm soda-lime glass substrate in the center of which a very

thin glass trip was attached so that after the completion of the film deposition the magnitude of the built-in stresses could be determined. The depositions were carried out at several sputtering parameters with the results summarized in Figure 27 and Figure 28.
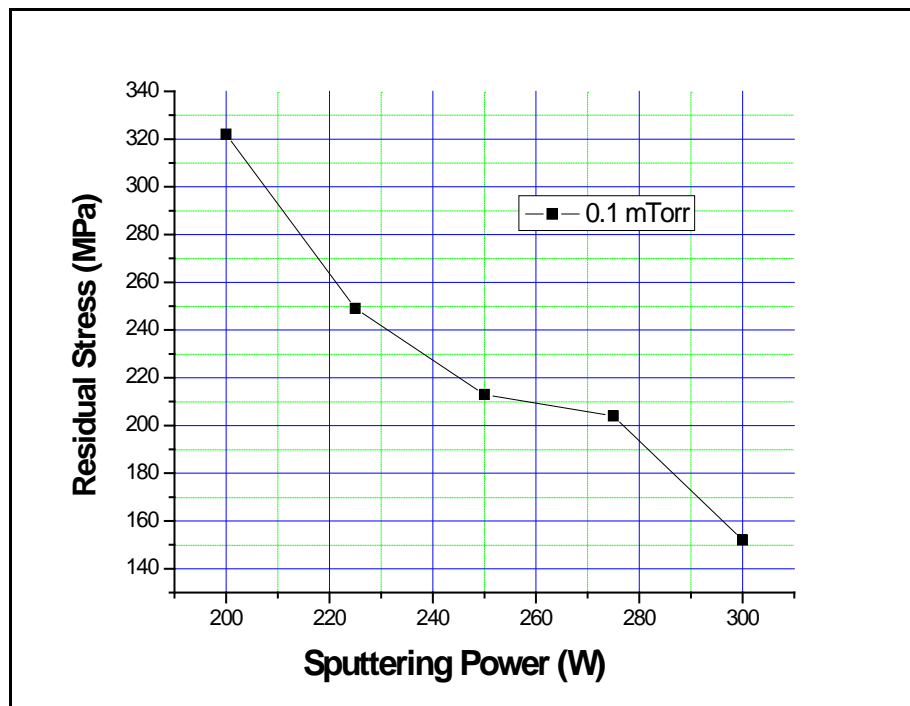
Figure 27 Variation of residual stress in molybdenum films deposited at various sputtering power

The decrease in residual stress with increase in sputtering power at constant pressure can be explained based on the fact that since the molybdenum atoms arriving at the glass substrate have higher kinetic energies they possess enough surface mobility to be able to relocate themselves in equilibrium their positions which results in reduced residual stress.
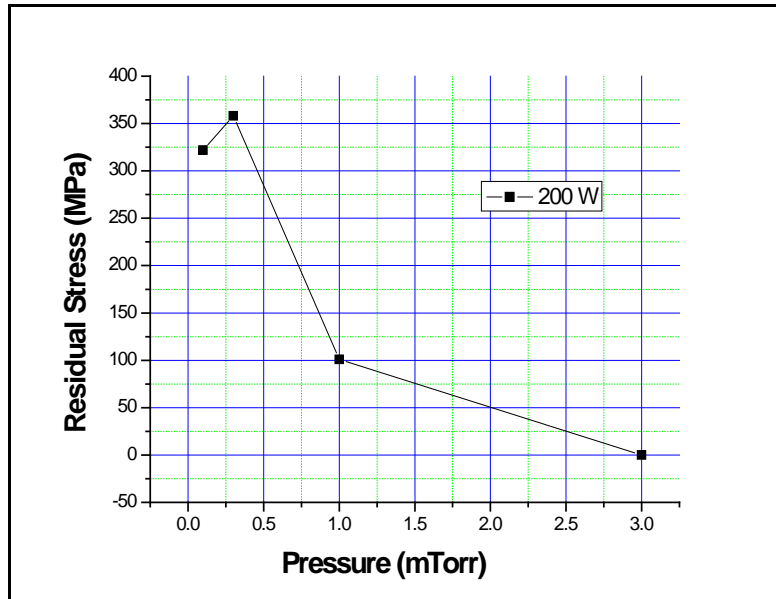
Figure 28 Variation of residual stress in molybdenum films deposited at various sputtering pressure

Figure 29 shows the bending of glass strip on account of built-in residual stress that developed during film deposition corresponding to the values depicted in Figure 27. It can be seen that all the films showed varied degrees of tensile stress. Even at the highest possible power of 300 W, although lower, tensile stress of about 150 MPa was observed and compressive stress was not observed in any of the depositions.

Figure 29 Bending of glass strips at various sputtering conditions

In the given scenario, the only feasible alternative in order to make an attempt to reduce the residual stress even further was to reduce the working distance between the target and the glass substrate and explore the film characteristics. The working distance between the target and the substrate was reduced to 7 cm. Based on the results summarized in Figure 27 experiments were carried out at reduced working distance of 7 cm at high power (300 W) and low gas pressures of 0.1, 0.3 and 1.0 mTorr. Surprisingly, the magnitude of the residual stress was so low that no bending was observed in any of the glass strips. In order to investigate the reason behind the observation molybdenum deposition was carried out with stationary substrate as discussed in the next section.

5.1.4 Molybdenum Deposition with Stationary Substrate

In order to demonstrate the fact that the film deposited in a single pass is actually a composite structure, following experimentation was carried out. At first the working distance between the target and the glass substrate was reduced to 7 cm. Molybdenum films were deposited on a 15 cm x 10 cm soda-lime glass substrate by keeping the substrate stationary over the target plasma in the middle as shown in Figure 30 which gives a schematic of the film deposition during magnetron sputtering. The numbers 1-8 correspond to the various regions on the surface of the sample. In this situation since the substrate is stationary different regions on the surface of the substrate receive flux of incoming species at various rates and angles. Also thin glass strips were mounted on the sodalime glass substrate at three locations corresponding to location 4 (in the center of the target), location 5 (on top of the race track), and on location 8 (away from the target plasma). The experimentation was carried out on either side of the target

as demonstrated in Figures 32, 32 and 33. After the deposition was complete very interesting results were obtained as seen in Figure 34 and Figure 35 showing photos of bending glass strips.
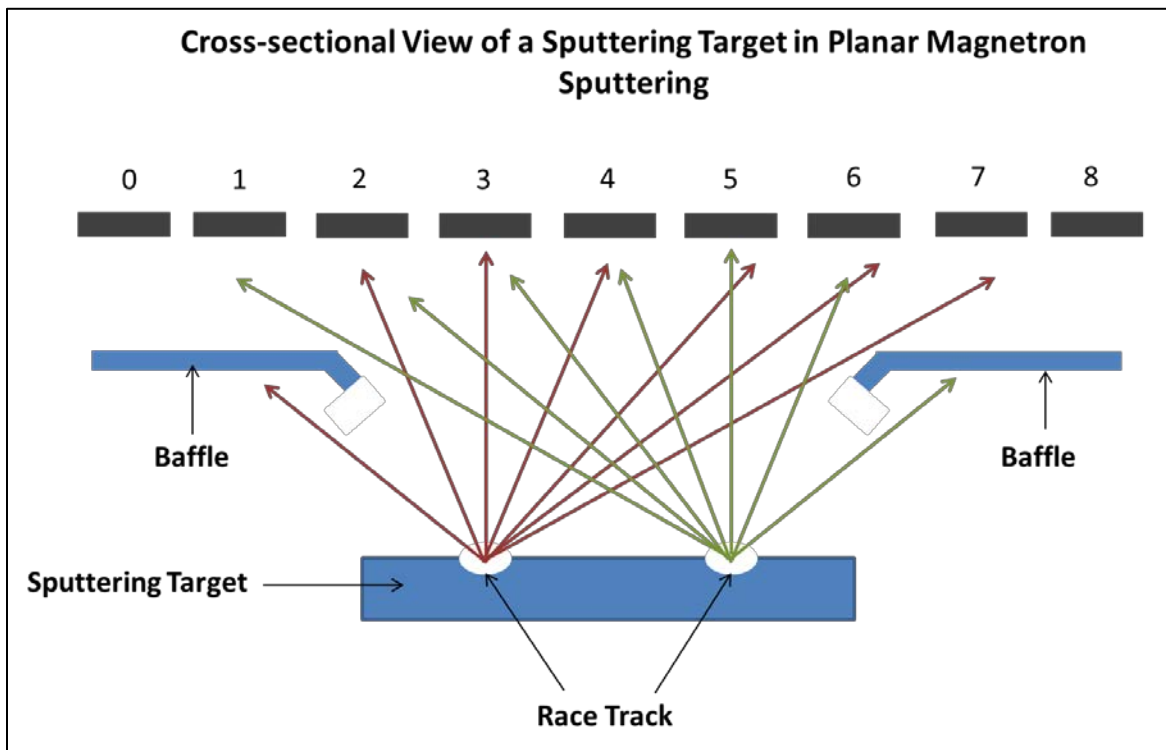
Figure 30 A schematic of deposition dynamics during DC magnetron sputtering
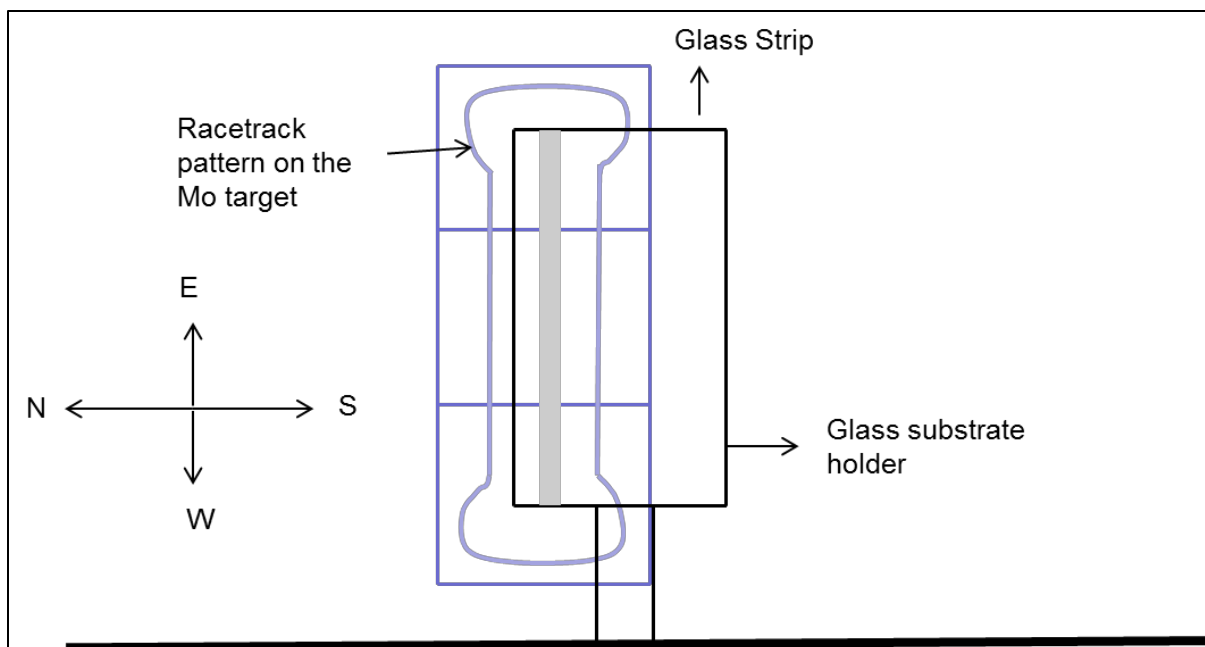
Figure 31 Orientation of glass strip with respect to the target plasma corresponding to the location 4
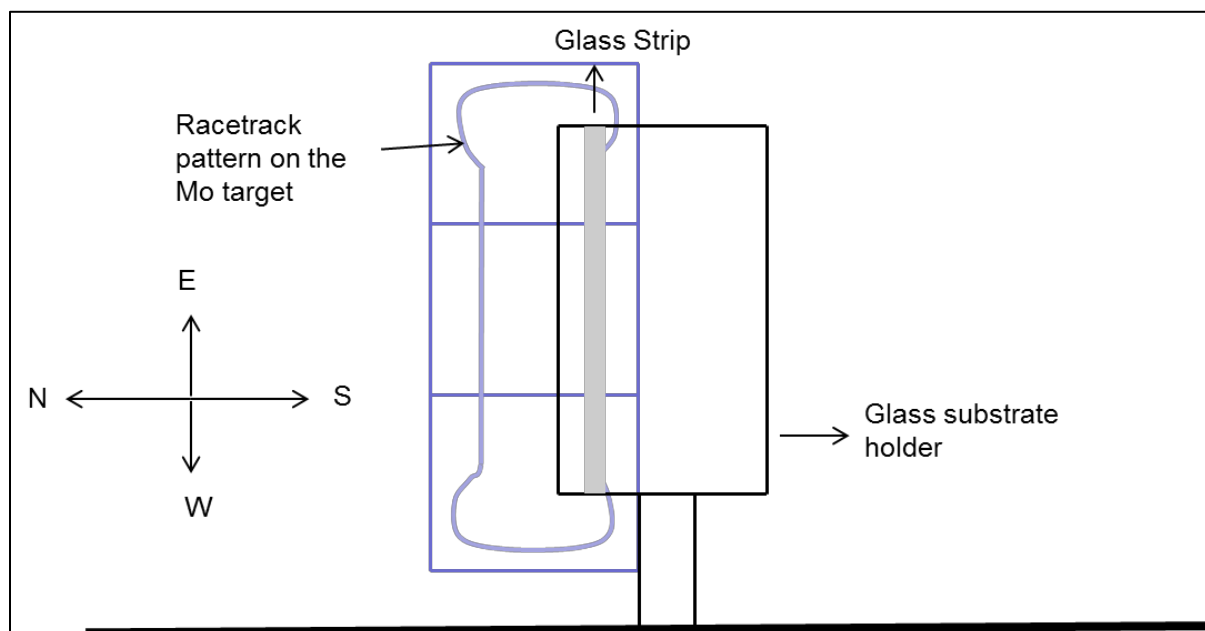
Figure 32 Orientation of glass strip with respect to the target plasma corresponding to the location 5
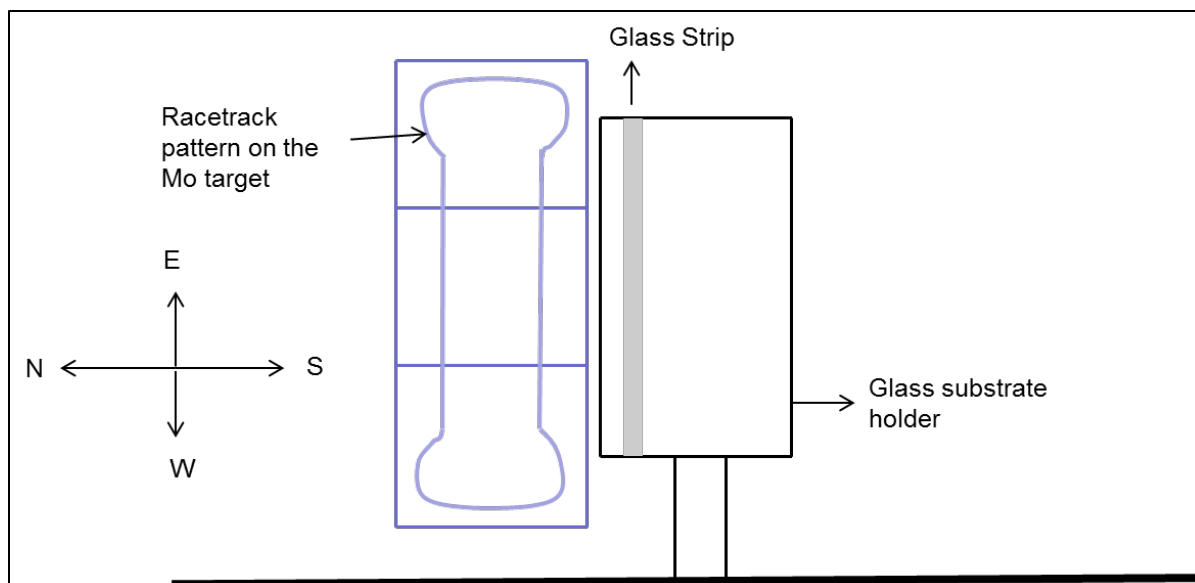
Figure 33 Orientation of glass strip with respect to the target plasma corresponding to the location 8

Figure 34 Bending of glass strips with stationary glass substrate during sputtering placed on the south side of molybdenum target

Figure 35 Bending of glass strips with stationary glass substrate during sputtering placed on the north side of molybdenum target

The glass strip on top of the race track (#5) that received flux of molybdenum atoms normal to the substrate showed a significant magnitude of tensile stress. However, the remaining two strips corresponding to region in the middle of the target (#4) and the region away from the target (#8) showed significant magnitude of compressive stress. Similar results were observed when the procedure was repeated on the north side of the target.

In order to explore the morphological features of the film deposited at various regions on the stationary substrate, SEM microscopy was carried out for location 4 (in the center of the target), location 5 (on top of the race track), and on location 8 (away from the target plasma).
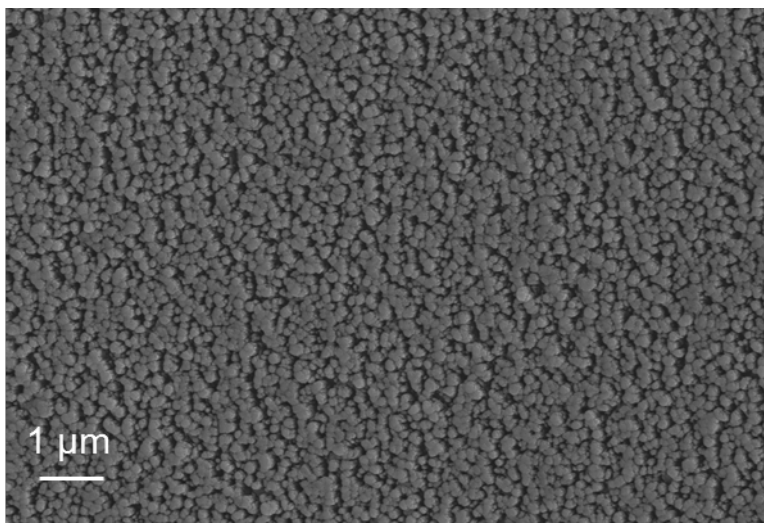
Figure 36 SEM micrograph (10000 x) of molybdenum film at location #8 that showed compressive state of stress
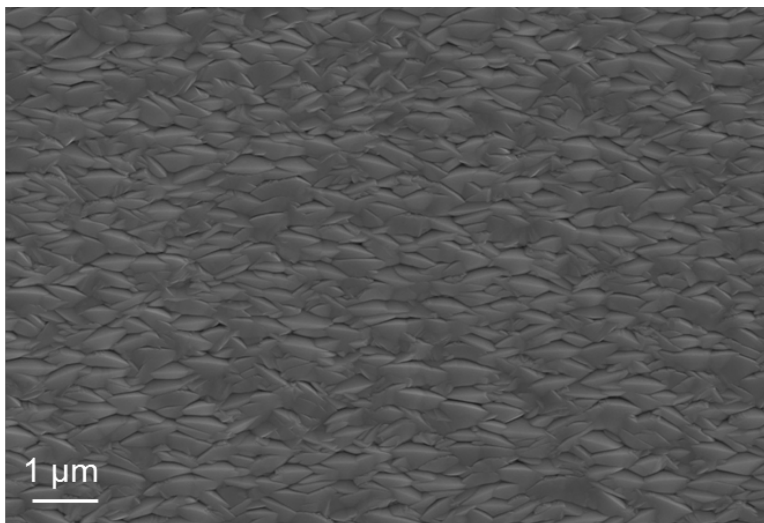
Figure 37 SEM micrograph (10000 x) of molybdenum film at location #5 that showed tensile state of stress
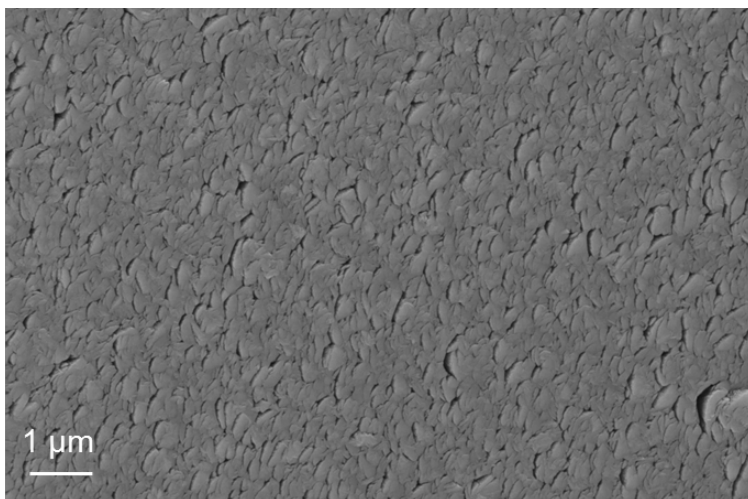
Figure 38 SEM micrograph (10000 x) of molybdenum film at location #4 that showed highly compressive state of stress

Three distinct microstructures can be seen in Figures 36, 37 and 38 determined by the angle at which the flux of atoms arrives at the given surface and the corresponding energies associated with them. It is can also be observed that the stress state associated with each microstructure is also different.

In order to get further details about the microstructural development at various regions on the surface of the substrate, SEM and XRD analysis was carried out for all the regions #1 though #8 for films deposited at two extreme conditions, at low power and high pressure conditions (200 W, 5 mTorr) and under high power and low pressure (300 W, 0.1 mTorr).
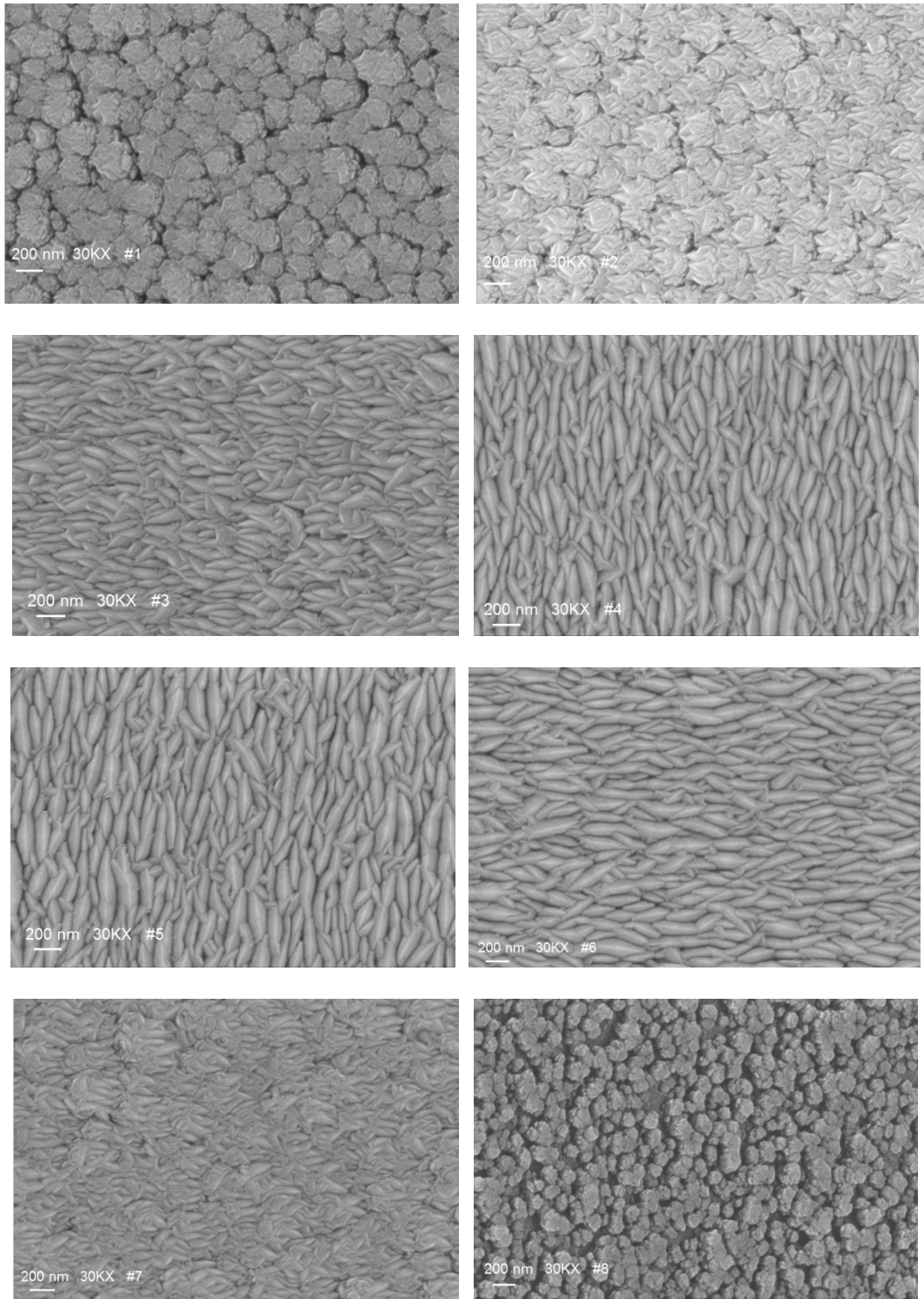
Figure 39 SEM micrographs (30000X) at various locations on molybdenum film deposited at 200 W, 5 mTorr with stationary substrate located on top of the target
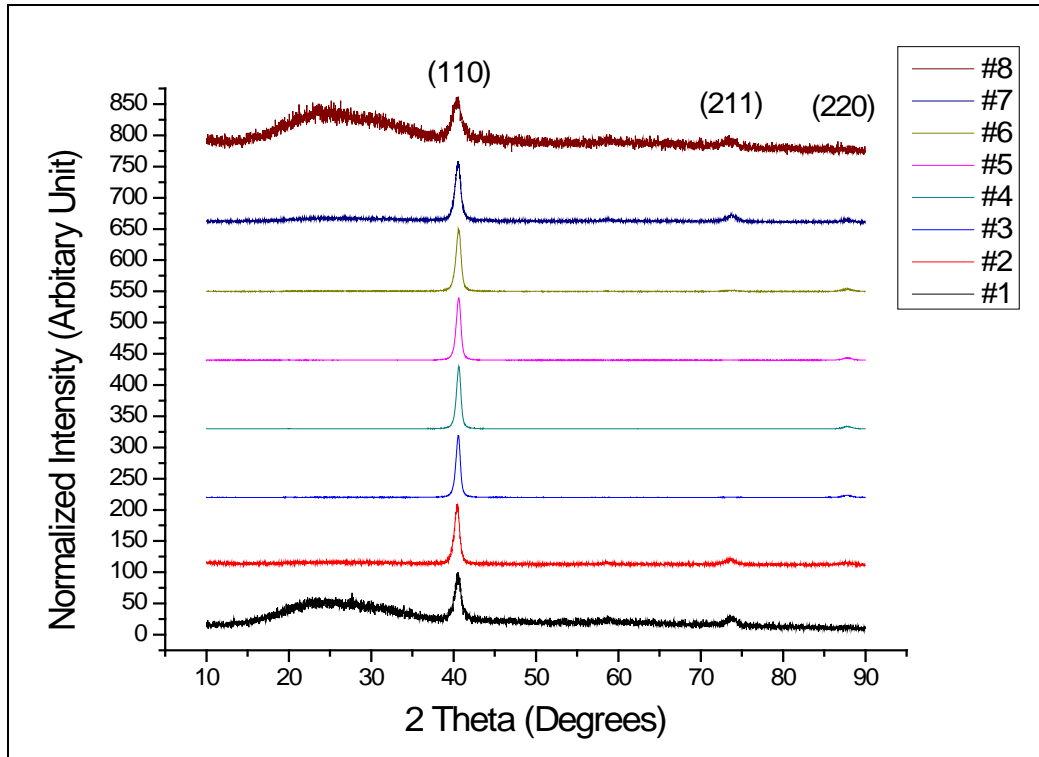
Figure 40 Comparison of XRD patterns for molybdenum films at various locations on stationary glass substrate deposited at 200 W, 5 mTorr

The SEM micrographs in Figure 39 depict the evolution of microstructure at various locations on stationary glass substrate deposited at 200 W, 5 mTorr. The regions in the middle of substrate correspond to a fish-like microstructure. Moving toward the ends it becomes equiaxed circular columns with more open structure. The microstructure in the in-between regions appears to be mixed type showing fish-like structure in near circular groups.

Figure 40 shows the corresponding XRD patters for the films depicted in Figure 25. Regions 2 through 7 show peaks for highly crystalline films with typical reflections (110), (211), (220) of a BCC crystal structure. However, the films at location 1 and location 8 at the edges show broad peaks corresponding to relatively less crystalline material. The films are also thinner

and hence did not have adequate thickness to evolve into a more crystalline phase. Since the atoms that arrive at these regions have lower energies the corresponding microstructure is more open with comparatively poor crystallinity. Similar analysis was also carried out for films deposited at high power and low pressure conditions (300 W, 0.1 mTorr).
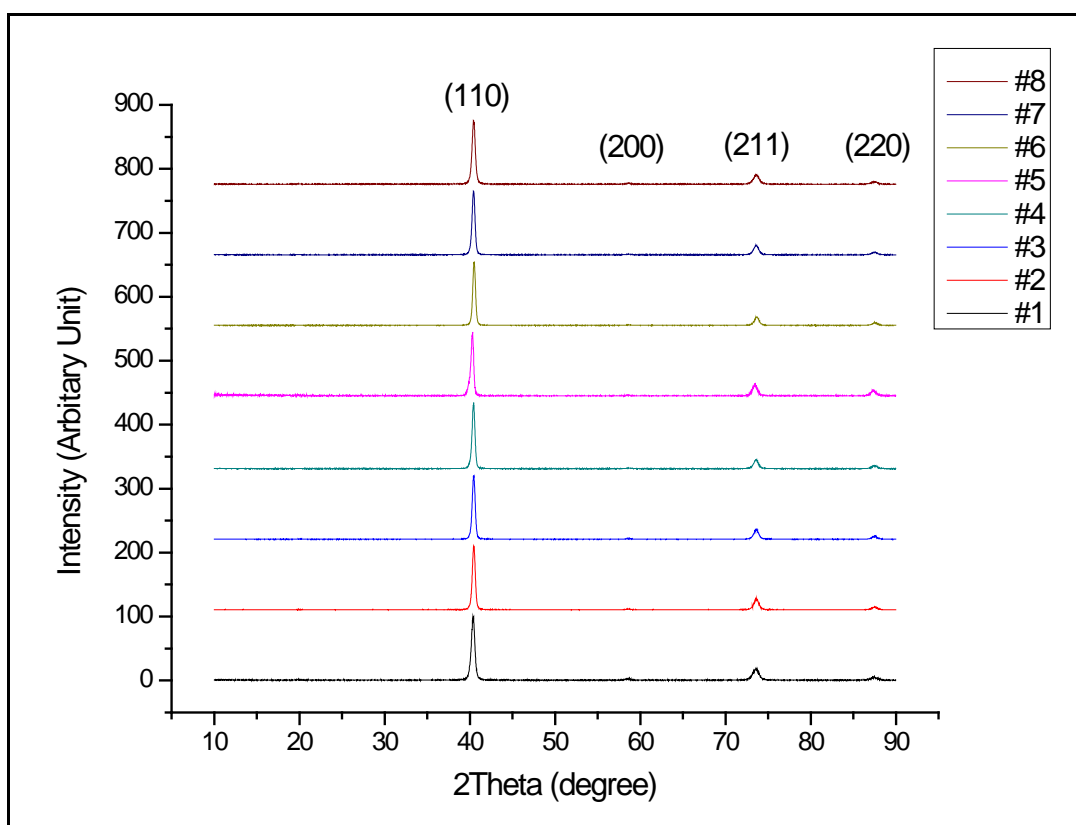
Figure 41 Comparison of XRD pattern for molybdenum films at various locations on stationary glass substrate deposited at 300 W, 0.1 mTorr
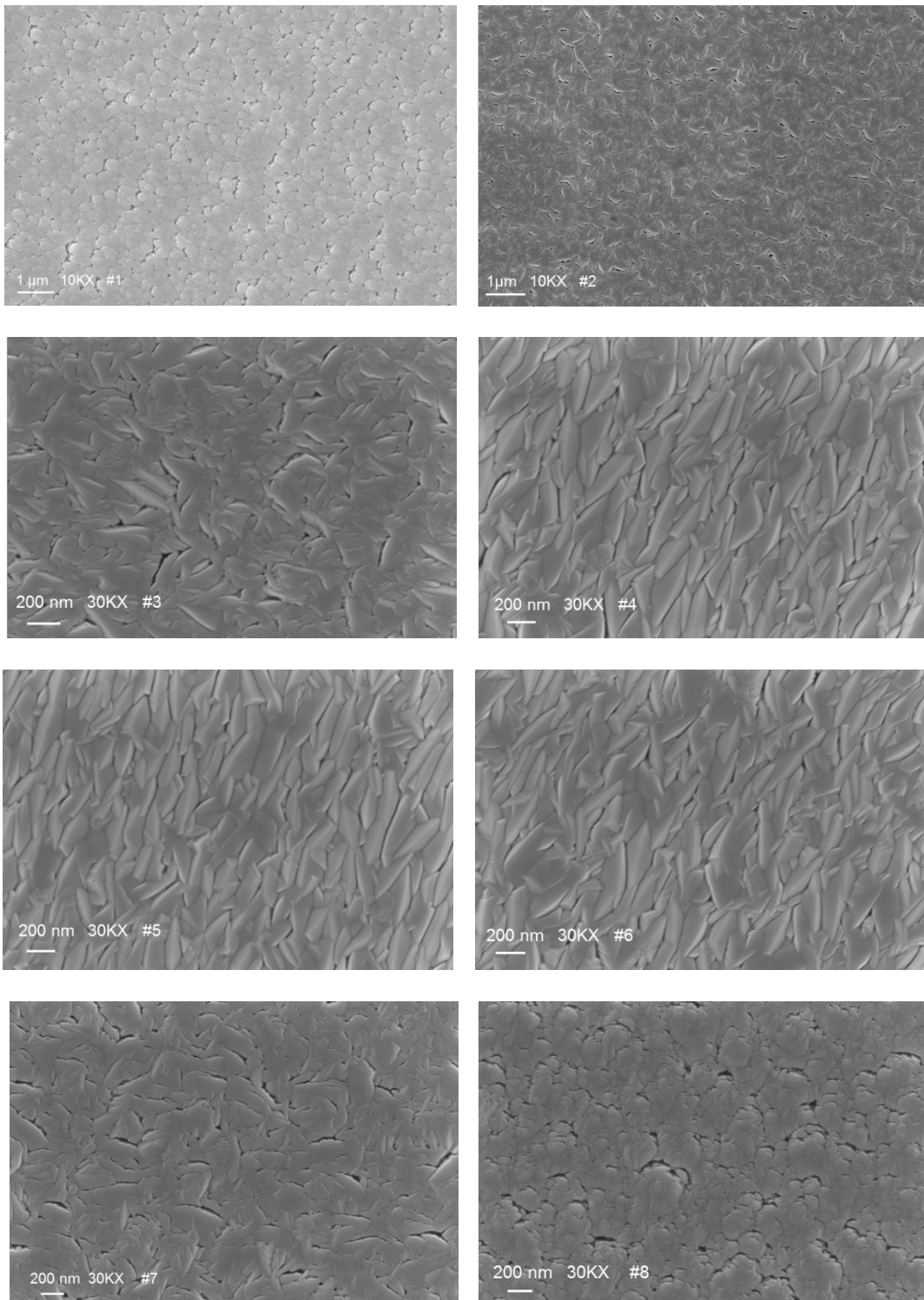
Figure 42 SEM micrographs at various locations on molybdenum film deposited at 300 W, 0.1 mTorr with stationary substrate located on top of the target

Figure 41 shows the corresponding XRD patters for the films depicted in Figure 40. In addition to (110), (211) and (220) reflections of a BCC crystal structure it can be observed that the films are also manifesting (200) peaks which were absent in films deposited at 200 W, 5 mTorr. Also the (110) peak reflections are sharper than the same reflection in the former showing comparatively better coalesced grains.

The SEM micrographs in Figure 42 show several microstructures depending upon the location on stationary glass substrate deposited at 300 W, 0.1 mTorr. The regions in the middle of substrate share similarities to fish like microstructure seen before for films deposited at 200 W, 5 mTorr with length-wise growth. Moving toward the end regions, the microstructure begins to take equiaxed circular morphology. However, the films are still more compact in this region than films deposited at 200 W, 5 mTorr. The microstructure in the in-between regions appears to be mixed type showing close to fish-like but with the growth in both length and width direction.

From the above results and discussion, it is clear that the flux of atoms arriving on the glass substrate with different energies and at different angles contribute to different morphological structure and different stress states in the deposited film. Also, the overall stress in a film deposited with moving substrate is a sum of these combined stress effects. In order to estimate the final stress in the film deposited with moving substrate depositions were carried out at a sputtering power of 300 W and a pressure of 0.1mTorr, 0.3mTorr and 1 mTorr. The reason for choosing high power low pressure regime has already been mentioned before. In each situation the glass strip was attached to the substrate to measure the final value of residual stress after deposition. It was found that in all the above mentioned deposition parameters the

magnitude of residual stress was too low to measure since no observable bending of glass trips could be detected.

Table 1 Test results of single layer molybdenum films deposited at various parameters

Deposition Parameters		Scotch tap peel test	High temperature Thermal test	Result (ok/not ok)
Power (W)	Pressure (mTorr)			
300	<0.1	No peeling or loss of film observed on the scotch tape	The film stayed intact	Ok
300	0.3	Films did not peel	No peeling	Ok
300	1	Films did not peel	No peeling	Ok

The films were subjected to following two tests. The first test known as the **scotch tape peel test** was carried out to determine if the deposited film were well-adherent to the glass substrate. After verifying this test it was essential to determine if the films would maintain integrity at high temperature. In order to verify this, all the films were taken to a temperature of near 550°C for 10 minutes in the rapid thermal annealing furnace (RTA) and also in conventional furnace for 1 hour at 500°C. The temperatures chosen here correspond to the actual working temperatures employed for processing of CIGS thin film solar cells in RTA furnace and in conventional furnace respectively. The results are tabulated in Table 1. Based on these results

it was decided to step further and complete actual device on the single layer molybdenum deposited at 300 W and 0.1 mTorr.

With this experimental study it became possible to develop single layer molybdenum film which has;

1. Highest deposition rates among the chosen several deposition parameters

2. Good adhesional strength to the soda lime glass substrate

3. Lowest possible residual stress

4. Lowest resistivity, suitable for a device quality back contact for solar cells

5. Improved stability at high processing temperatures with no signs of peeling or flaking

Estimates were made for reduction in deposition times and material consumption compared to multilayer structure. Typically, the molybdenum-coated glass substrate available from commercial suppliers is approximately 1 µm thick. With a single pass deposition it became possible to reduce thickness to about 0.7 µm, which corresponds to 30% savings in material consumption. Also, due to higher deposition rates that were achieved as a result of low pressure sputtering and high power conditions along with reduced working distance the process could be completed with a substrate movement rate of 0.63 cm/minute instead of a total time of 0.4 cm/minute for a multilayer structure of similar thickness. This corresponds to reduction in deposition time by 30%. It can thus be concluded that the development of single layer molybdenum in this research work is well-suited in a manufacturing set-up where time and material utilization are very critical. The deposition rates mentioned here do not set up a limit on what can be achieved in an industrial set-up. With more powerful power supplies and improved

cooling arrangements for metallic target it would be possible to increase the deposition rates. This research intends to provide a guideline in the right direction to achieve that goal.

5.2 Development of CIGS2 Solar Cell on Single layer Molybdenum Back Contact

After successful depositions of single layers of molybdenum back contacts with minimum residual stress and optimum resistivity, was accomplished, it was necessary to determine whether they could be used as back contact for chalcopyrite solar cells. It was decided to fabricate CIGS2 solar cells instead of CIGSe solar cells for two reasons. First, processing in H_2S ambient is a harsher environment than processing in selenium ambient. Second, due to shortage in the availability of organometallic selenium precursor, it was decided to limit its consumption.

Figure 43 and Figure 44 show the cross-sectional SEM for single layer and multilayer molybdenum films. For the sake of comparison, deposition of CuGa and indium metallic precursors was carried out on multilayer molybdenum film coated sodalime glass substrate procured from a manufacturer (will be referred as commercial molybdenum in this dissertation) and on in-house developed single layer molybdenum on sodalime glass. Metallic precursors were deposited on single layer molybdenum films deposited at the parameters of 300 W sputtering power and at an argon pressure of <0.1mT and 1.0 mTorr. The molybdenum films and absorbers deposited on them discussed in this section will be quoted as SL0.1 and SL1.0 corresponding to single layer molybdenum films deposited at argon pressure of <0.1mT and 1.0 mTorr respectively.

84

Absorbers were prepared in all cases by annealing in gas ambient of dilute 8-10 % H_2S at 475 °C with a preannealing step at 125 °C for 25 minutes.
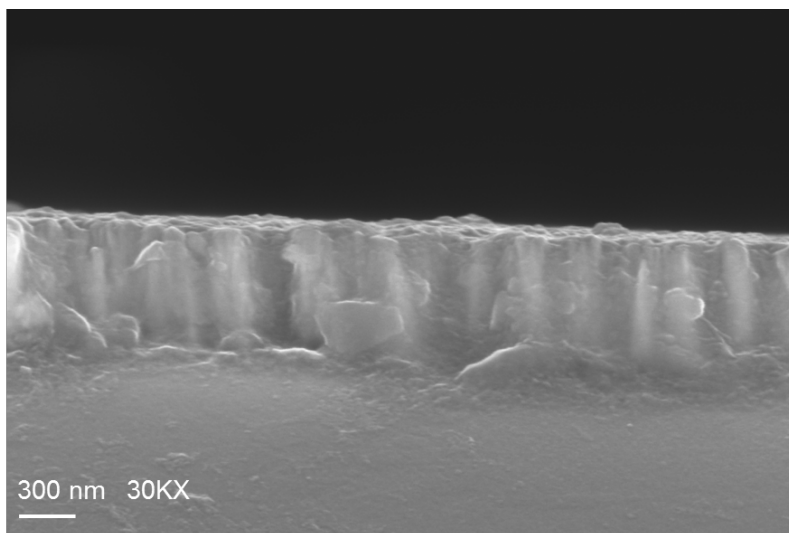
Figure 43 Cross sectional SEM of SL 0.1 molybdenum on sodalime glass substrate
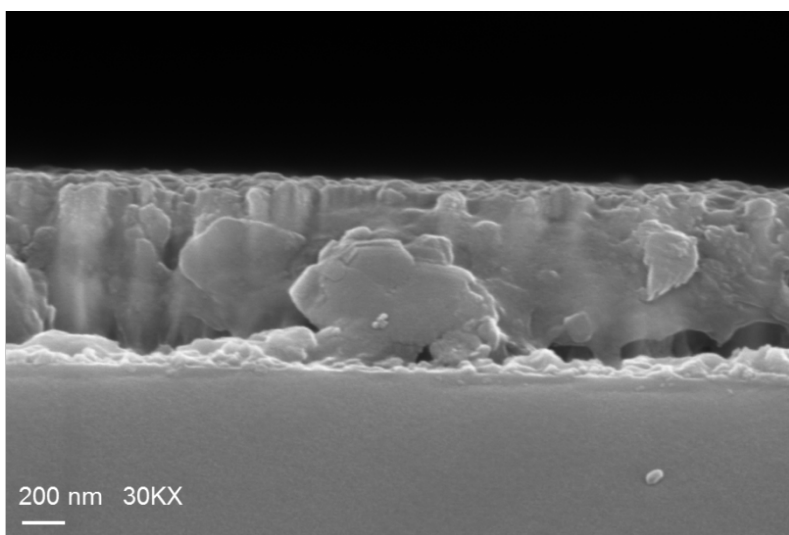
Figure 44 Cross sectional SEM of multilayer molybdenum on sodalime glass substrate

Figure 45 shows cross sectional SEM for a representative sample with CIGS2 absorber on top of the SL 0.1 molybdenum film. It can be seen in the SEM micrograph that the interface between the glass and molybdenum and between molybdenum and CIGS2 is continuous showing sign of good adhesion. Figure 46 shower the planar SEM of the same absorber showing compact grains of CIGS2.
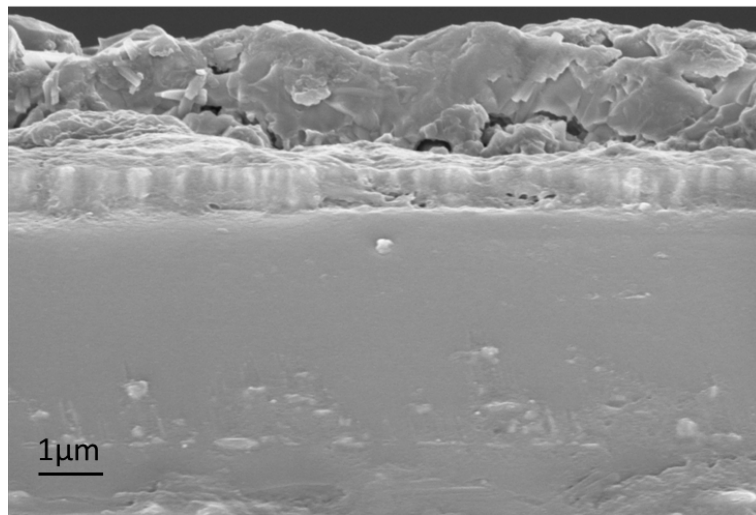
Figure 45 Cross sectional SEM (10000x) of CIGS2 absorber on single layer molybdenum back contact
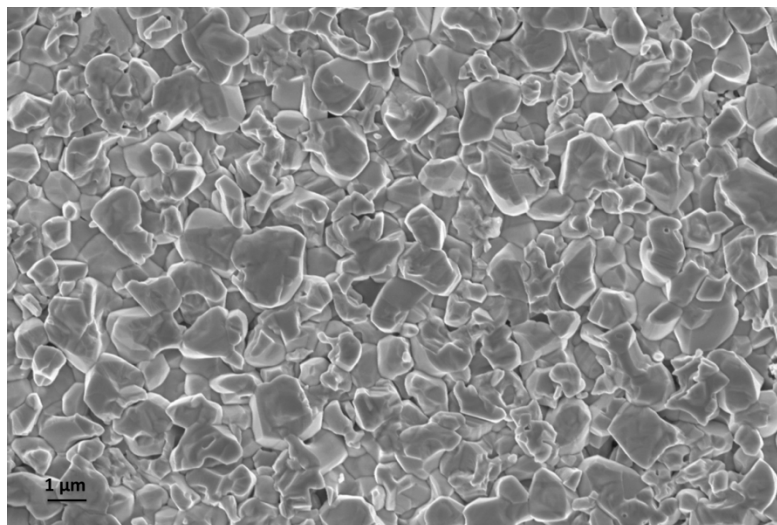
Figure 46 SEM micrograph (10000x) of CIGS2 absorber on SL 0.1 showing large, compact and
continuous grains
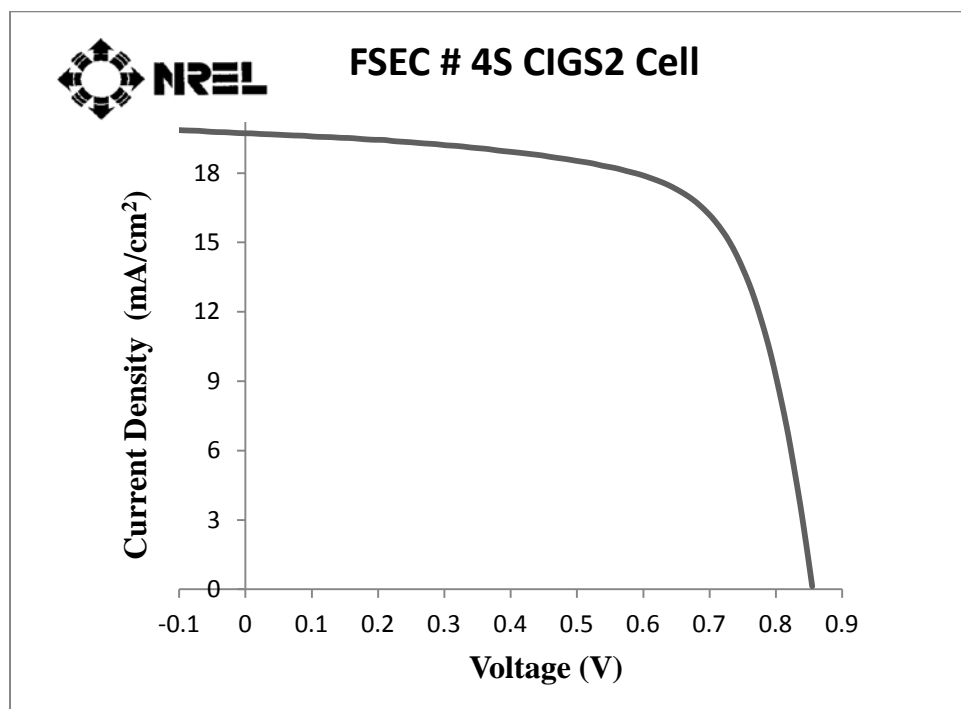
Figure 47 I-V characteristics of CIGS2 solar cell (#4S) on SL 0.1 molybdenum

Table 2 PV parameters for CIGS2 thin film solar cell (#4S) on SL 0.1 molybdenum

Parameter	Voc (V)	Jsc (mA/cm^2)	FF (%)	Ŋ (%)	Rs (Ω-cm^2)	Rsh (Ω-cm^2)
Values	0.856	19.72	67.36	11.38	5.19	765

CIGS2 solar cells were successfully fabricated on the SL0.1 molybdenum. Figure 47

provides the NREL certified I-V curve for a device with a device efficiency of 11.38%.

Similarly, absorbers were also prepared from precursors deposited on molybdenum films

procured from a manufacturer that went under identical processing conditions as mentioned before.
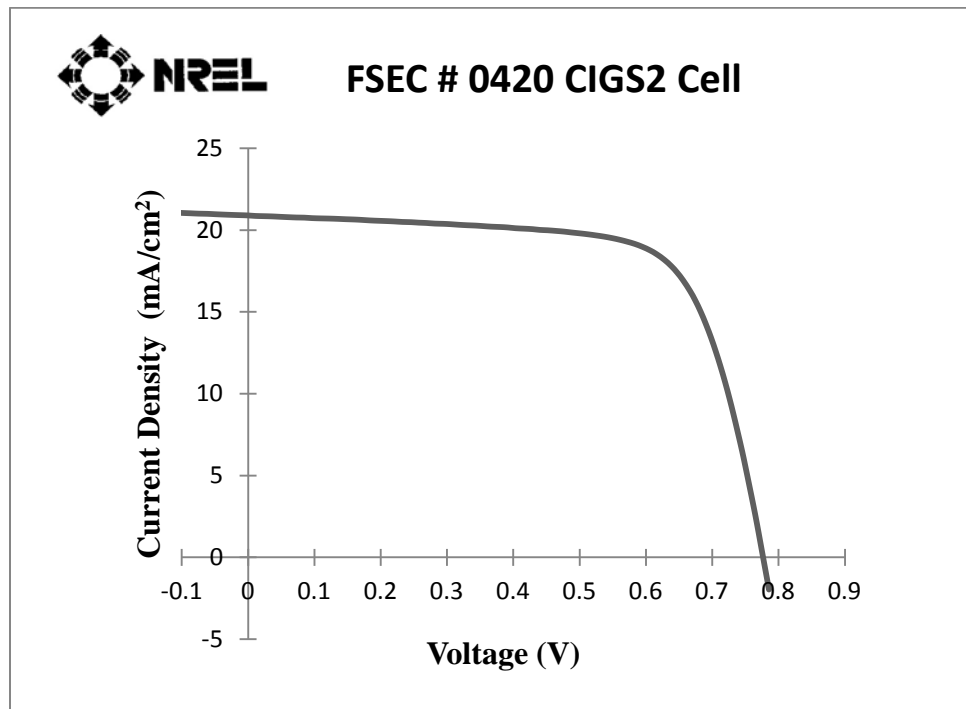
Figure 48 I-V characteristics of CIGS2 solar cell (#0420) on commercially available molybdenum

Table 3 PV parameters for CIGS2 thin film solar cell (#0420) on commercially available molybdenum

Parameter	Voc (V)	Jsc (mA/cm^2)	FF (%)	Ŋ (%)	Rs (Ω-cm^2)	Rsh (Ω-cm^2)
Values	0.7771	20.886	70.36	11.42	4.94	633

Figure 48 provides the I-V plots for the devices completed on commercially available molybdenum. Table 3 provides the PV characteristics extracted from the I-V plot showing

devices with good efficiency comparable to the devices on SL0.1 molybdenum. It can be noted that the series resistance is slightly lower compared to the former.

CIGS2 devices were also fabricated on SL1.0 molybdenum. Figure 46 provides the I-V plot followed for the completed device and the PV characteristics given in Table 4.
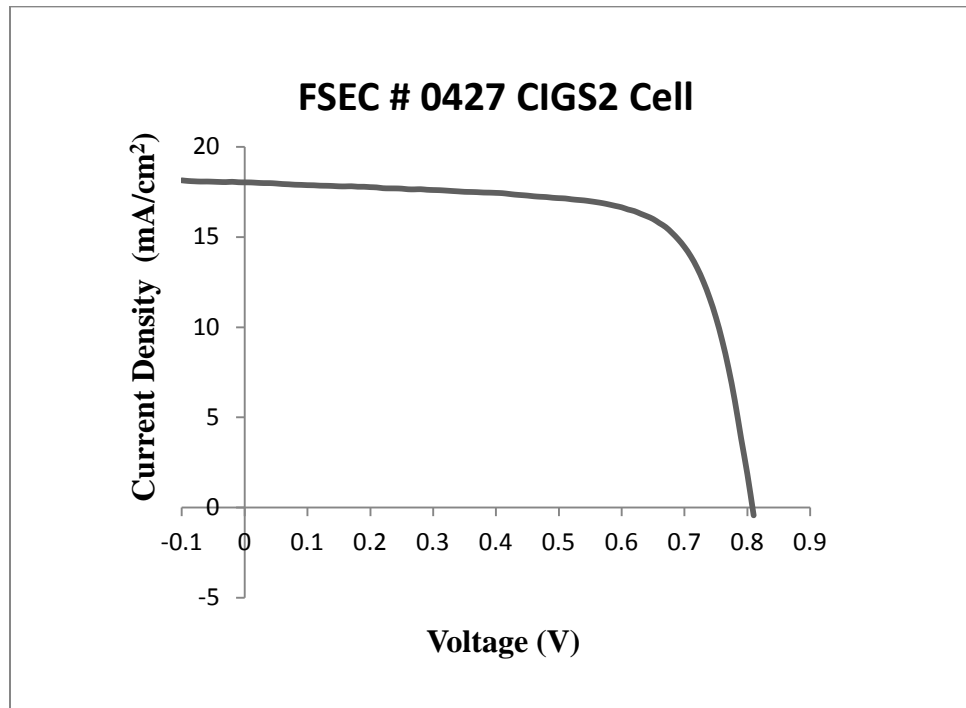
Figure 49 I-V characteristics of CIGS2 solar cell (#0427) on SL1.0 molybdenum

Table 4 PV parameters for CIGS2 thin film solar cell (#0427) on SL1.0 molybdenum

Parameter	Voc (V)	Jsc (mA/cm^2)	FF (%)	Ƞ (%)	Rs (Ω-cm^2)	Rsh (Ω-cm^2)
Values	0.80	18.14	72.3	10.56	6.97	750

From the PV characteristics in Table 4, it can be observed that series resistance calculated for the devices on SL1.0 molybdenum was highest compared to the devices completed on SL0.1

and commercial molybdenum. The higher series resistance was possibly due to formation of thicker molybdenum sulfide layer compared to other devices at the processing temperature of 500 °C. From a device fabrication and manufacturing view point single layer molybdenum SL0.1 is the preferred choice on account of better device performance and higher deposition rates achieved.

5.3 Optimization of Deposition Rates for Metallic Precursor Films

DC magnetron sputtering is used for deposition of metallic precursors from CuGa alloy and indium target. In case of sputtering, the deposition rate changes with the changes in sputtering power and pressure and the working distance between the metallic target and the substrate. However, the deposition rate versus sputtering power and pressure follows a U shaped curve and therefore, it is essential to optimize the sputtering power and pressure in order to get the highest possible deposition rates for a given system.

In the previous experiments, the sputtering power employed for the CuGa target was varied while keeping the sputtering pressure constant at 0.1 mTorr. The sputtering power was varied from 200 W to 350 W and the thickness calibration was carried out using a Dektak 3 Profilometer.

Realizing the possibility of being able to reduce the working distance (vertical distance of the substrates above the sputtering target), experiments were carried out to determine the effect of reducing the working distance on the deposition rates. It was observed that the deposition rate increased linearly with increase in the sputtering power for each set of working distance. Figure 50 shows the variation of deposition rate at a given working distance with respect to the

sputtering power and Table 5 shows the total thickness deposited for each sputtering power and the total time it took for deposition.
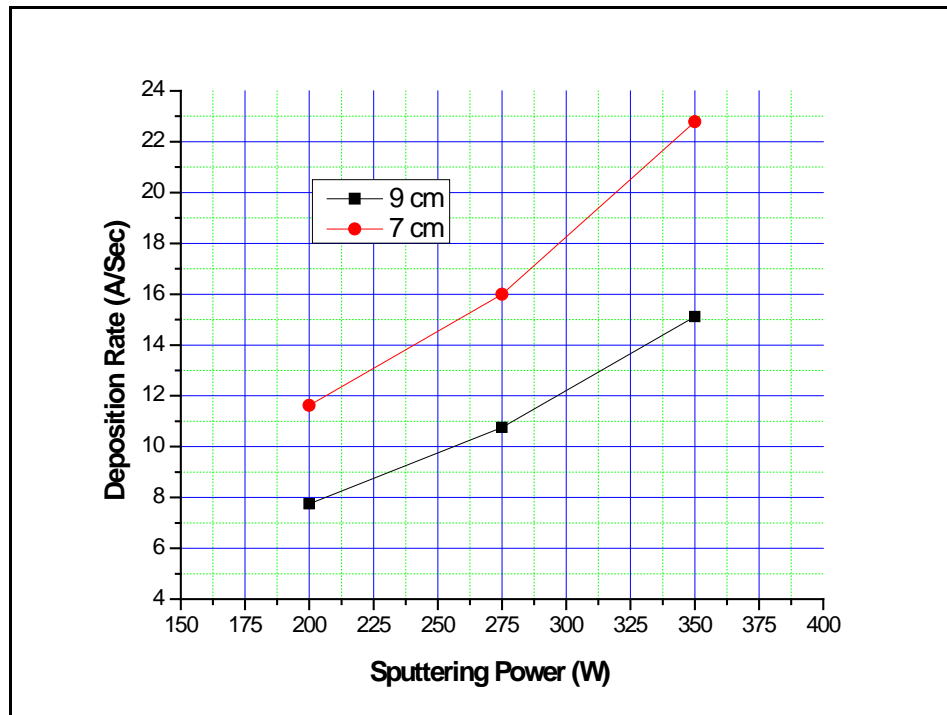
Figure 50 Effect of Sputtering power on deposition rate for CuGa target for two working distances

Table 5 Relationship between sputtering power and deposition rate for CuGa target at two working distances

Sputtering Power (W)	Total Deposition Time over 10cm width (Seconds)	Deposition Rate (Å/S) (90mm working distance)	Deposition Rate (Å/S) (70mm working distance)
200	800	7.75	11.62
275	800	10.75	16
350	800	15.12	22.78

In a similar way estimation of deposition rates was also carried out for the Indium target. Figure 51 provides the variation of the deposition rates with sputtering power and working distance.
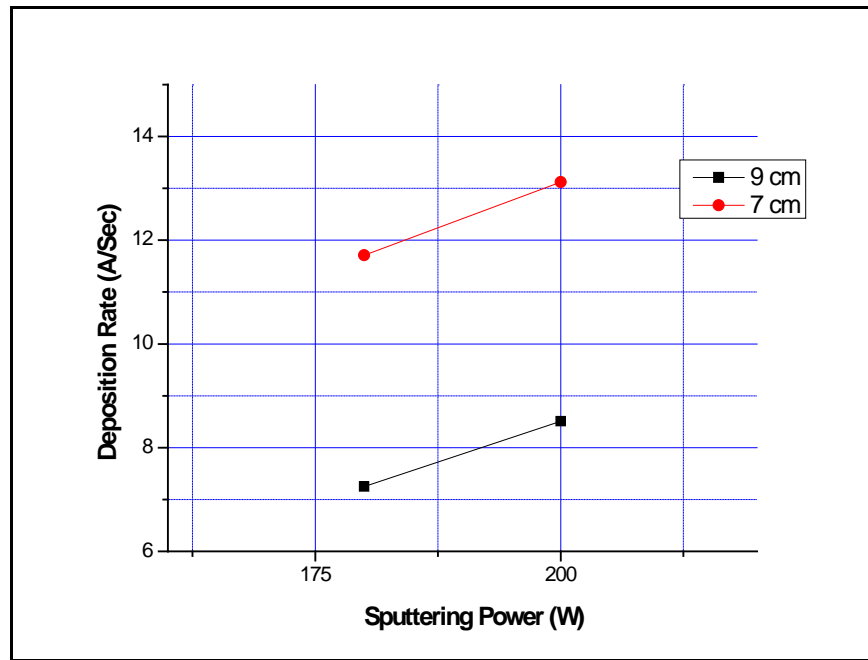
Figure 51 Effect of Sputtering power on deposition rate for indium target for two working distances

Table 6 Relationship between sputtering power and deposition rate for indium target at two working distances

Sputtering Power (W)	Total Deposition Time over 10cm width (Seconds)	Deposition Rate (Å/S) (90mm working distance)	Deposition Rate (Å/S) (70mm working distance)
180	1280	7.25	11.71
200	1000	8.51	13.12

It can be noted that for the identical sputtering power of 200 W, the deposition rate for indium target are slightly higher than those for CuGa target. Being a low melting metal with melting point of 156.6 °C, caution was taken not to increase the power since that could lead to generation of excessive heat at the target and melt it. On the same ground, being low melting metal high deposition rates can be easily achieved by sputtering at low pressure and optimizing the sputtering power to avoid excessive heat generation. With improved target cooling arrangements it would be possible to increase the deposition rates further for both the CuGa and Indium targets in order to meet the deposition rates estimated by researchers at NREL for CIGS progress roadmap in order to make PV manufacturing cost effective.

5.4 Effect of Location of Sodium Precursor on the Development of CIGS solar cells

Sodium plays a very important role in the development of CIGSeS thin film solar cells as discussed before in the materials review section of this dissertation. In the earlier research work carried out at FSEC, the effect of various quantities of NaF on the absorber quality and device performance of CIGSeS thin film solar cells has been studied. Normally, the sodium precursor is deposited over the molybdenum back contact before the metallic precursor deposition in a two-stage process. However, not enough work has been carried out to investigate the effect of location of sodium precursor on the properties of the absorber films prepared by selenization of metallic precursors. Experiments discussed in this section were carried out to understand the same and suggest the optimal location of the sodium precursor. The precursors used in this study were deposited on four layer molybdenum back contact.

Initially, a 40 Å thick layer of NaF was deposited on top of Cu-Poor metallic precursor. The film was selenized at 500 °C for 60 minutes. Table 7 provides the elemental composition of the resulting absorber film determined with EPMA analysis.

Table 7 EPMA analysis of film selenized at 500 °C for 60 minutes

Element	Cu	In	Ga	Se	Cu/(In+Ga)
10kV	20.72	28.75	1.0	49.5	0.67
20kV	21.03	27.54	0.19	51.23	0.75

In order to observe the microstructure of the resulting absorber films, SEM microscopy was carried out for the films as shown in Figure 52. It can be seen that the grains are highly faceted, compact and continuous.
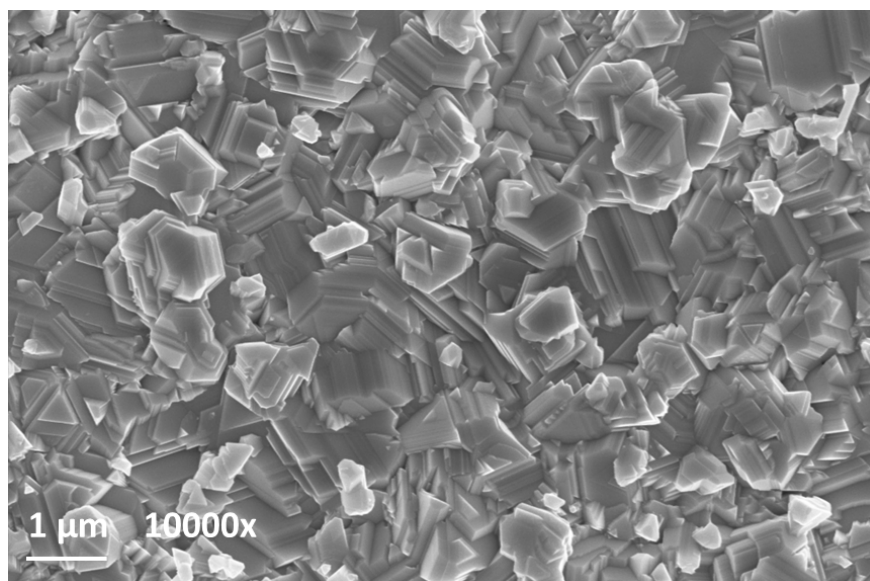
Figure 52 SEM micrograph of film selenized at 500 °C for 60 min with 40 Å NaF in the front (#0704-2A)
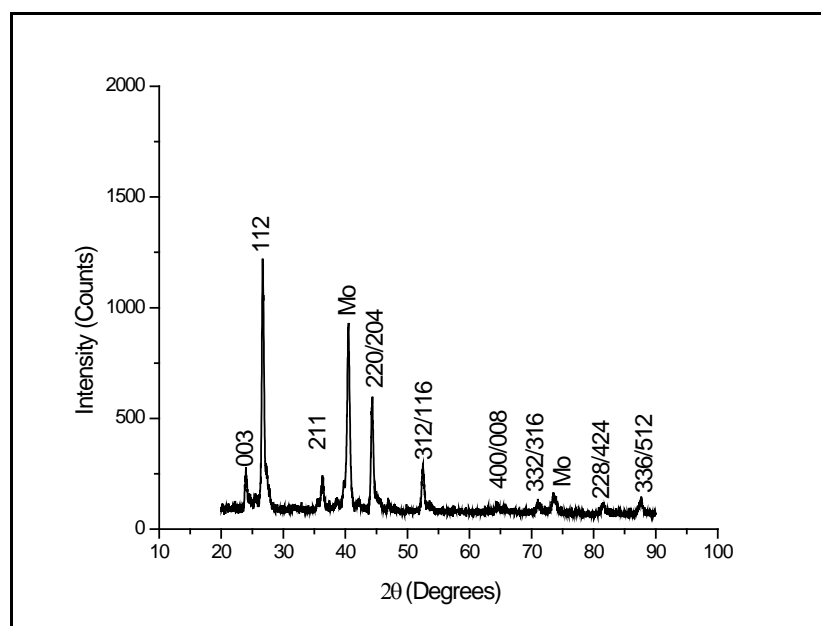
Figure 53 XRD pattern for CIGSe absorber with 40 Å NaF in the front (#0704-2A)
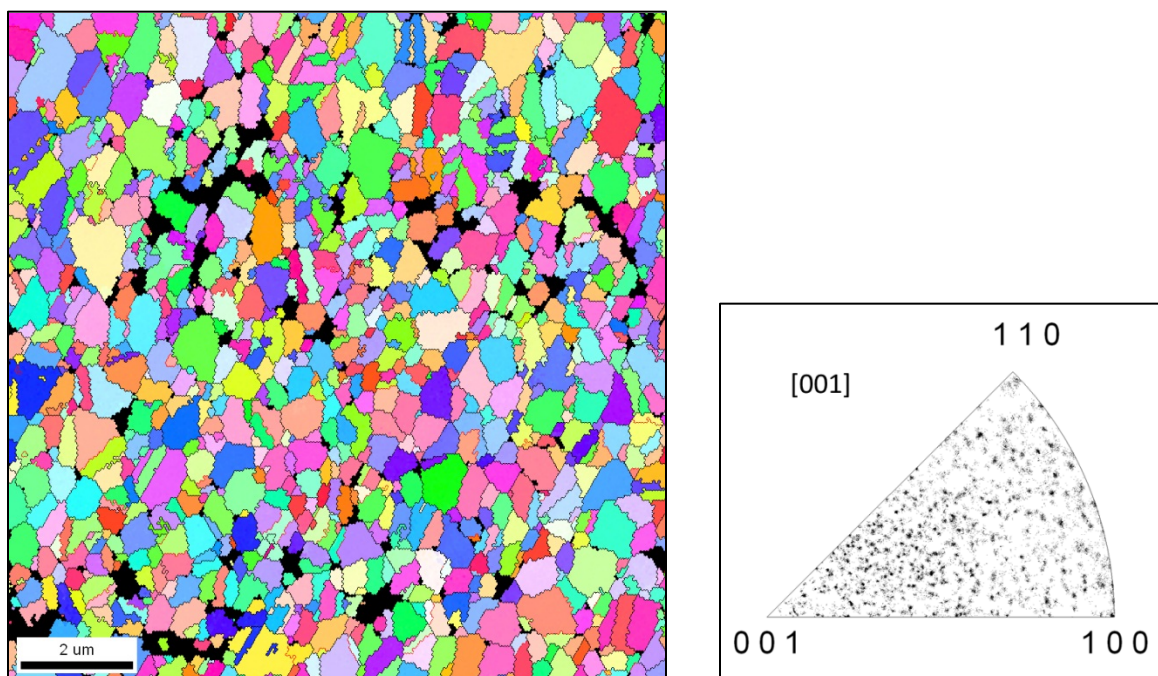
Figure 54 EBSD map for absorber film (#0704-2A) selenized at 500 °C for 60 minutes
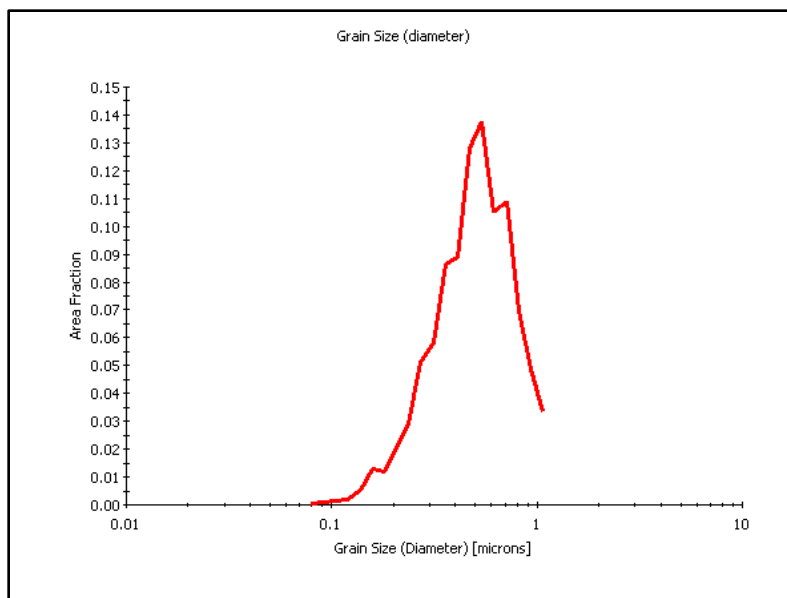
Figure 55 Grain size distribution obtained from EBSD map for film selenized at 500 °C for 60 min.

Figure 53 provides the XRD pattern for the CIGSe thin film showing (112), (211), (220/204), (312/116), and other reflections of highly crystalline chalcopyrite CIGSe and also reflections from molybdenum. The strongest reflection was from (112) plane at $2\theta = 26.68°$. The d-spacings for (220) and (204), (116) and (312), (008) and (400) of CIGSe are very close. Hence for each peak both of the reflections have been indicated in the XRD spectra. The lattice parameters calculated using the XRD data were $a_0 = 5.77$ Å and $c_0 = 11.59$ Å. The d-spacings of the planes calculated from XRD data of the film closely match with those of a $CuInSe_2$ phase. The molybdenum reflection was observed at $2\theta = 40.5°$.

EBSD mapping was carried out for absorber films to in order to estimate grain size and its distribution as shown in Figure 54 and Figure 55. It was found that only 3% of grains had size greater than 1µm. The grain size distribution peaked at around 0.5 µm comprising around 14 % of grains. It was important to investigate the quality of the absorber film from a device

performance view point. Therefore, devices were completed with the as- prepared absorber film. Figure 56 shows the light and dark I-V curve for the completed device. PV characteristics were extracted from the plot and the values are summarized in table 8.

Table 8 PV performance characteristics extracted from the I-V data for sample # 0704-2A

Parameter	Voc (V)	Jsc (mA/cm^2)	FF (%)	Ƞ (%)	Rs (Ω-cm^2)	Rsh (Ω-cm^2)
Values	0.46	35.25	59.23	9.67	3.2	1050
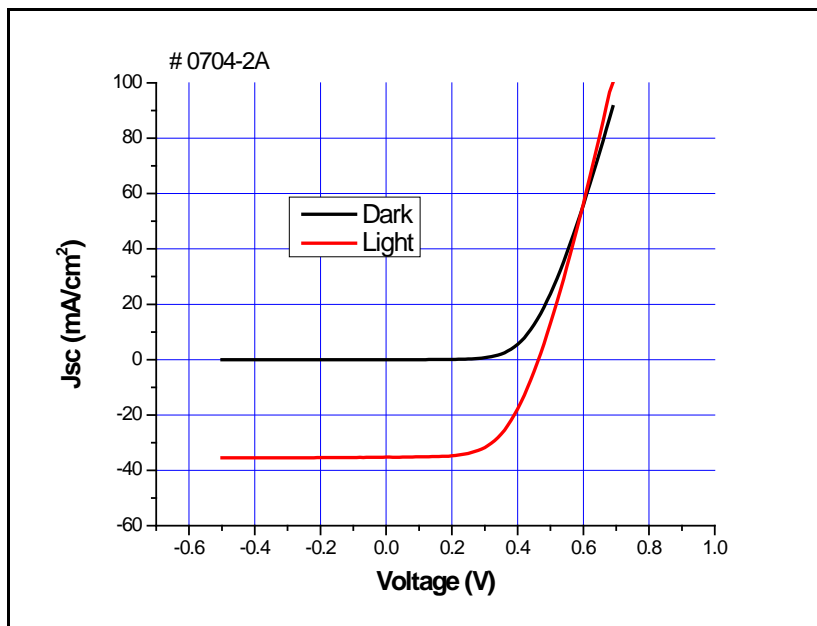
Figure 56 Current-Voltage Characteristics for sample # 0704-2A

It can be seen that although 40 Å NaF in the front provides a good device, the current density is still lower for a pure CIS absorber. With an effort to improve the absorber quality even better, the amount of sodium was increased to 80 Å in the front of precursor. The film was also

selenized at 500 °C for 60 minutes and devices were also completed on this absorber (#1020). Table 9 summarizes the PV performance characteristics extracted from the I-V data.

Table 9 PV performance characteristics extracted from the I-V data for sample # 1020

Parameter	Voc (V)	Jsc (mA/cm^2)	FF (%)	Ŋ (%)	R_s (Ω-cm)	R_{sh} (Ω-cm)
Values	0.46	38	66	11.8	1.5	1226

Improvement in J_{sc} and fill-factor is clearly evident from the I-V data with increase in the NaF content from 40 Å to 80 Å. It is known that addition of sodium improves the surface morphology and favors homogenization of the films, thereby minimizing and even eliminating the hillock like growth on the film surface and reducing defect. Sodium also has a high mobility and has the ability to act as a fluxing agent by imparting higher mobility to the other atomic species during the growth of the absorber film. Higher mobility of atoms results in improved grain growth.

CIGSe absorbers were also prepared with 40 Å and 80 Å NaF at the back for the sake of comparison with devices prepared with 40 Å and 80 Å NaF at the front. Figure 57 and Figure 58 provides the I-V characteristics for the as-prepared devices with 40 Å and 80 Å NaF at the back.
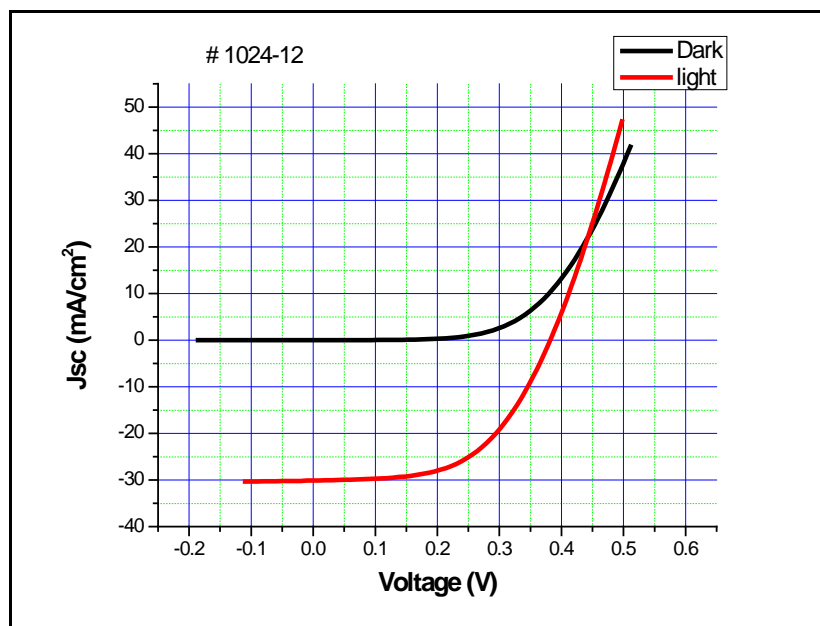
Figure 57 Current-Voltage Characteristics for sample # 1024-12 with 40 Å NaF at the back
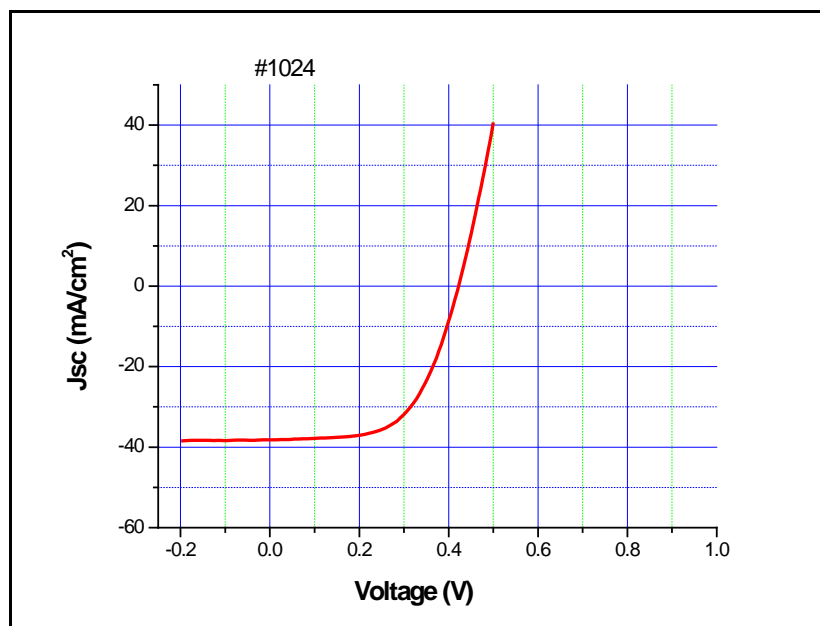
Figure 58 Current-Voltage Characteristics for sample # 1024 with 80 Å NaF at the back
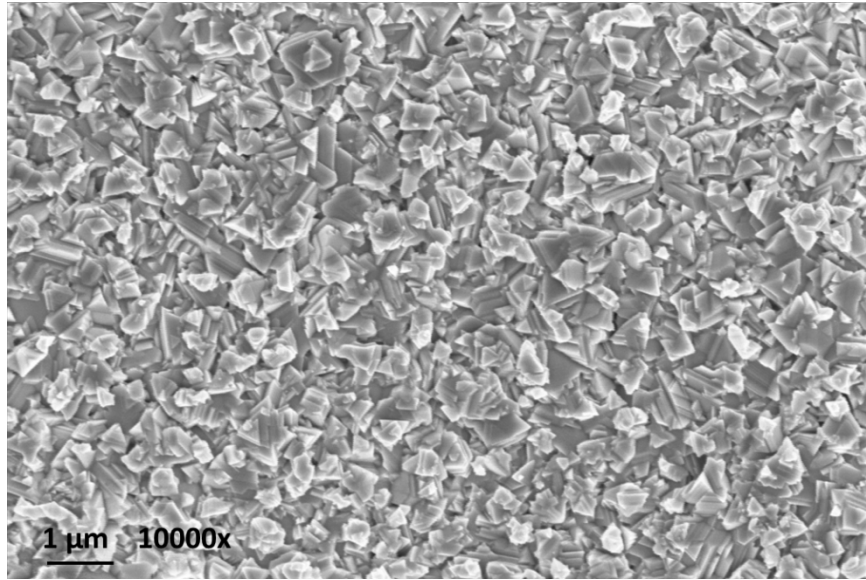
Figure 59 SEM micrograph of the absorber film selenized for 60 minutes with 80 Å NaF at the back (#1024)

Table 10 Comparison of PV characteristics for samples with 40 Å and 80 Å NaF at the Back

Parameter	Voc (V)	Jsc (mA/cm^2)	FF (%)	η (%)	R_s (Ω-cm^2)	R_{sh} (Ω-cm^2)
40 Å Back	0.38	30.1	54.4	6.29	2.26	455
80 Å Back	0.42	38.5	58.7	9.6	1.78	500

Table 10 summarizes the PV performance characteristics extracted from the I-V data for samples with 40 Å and 80 Å NaF at the back. Addition of sodium makes a significant impact on the overall improvement in the device quality of the films as reflected by the improvement in the J_{sc}, V_{oc}, and fill-factor with an overall increase in the device efficiencies from 6.3 % to 9.6 %. Comparison of SEM micrographs in Figure 52 and Figure 59 gives a clear indication that the location of NaF in the front and in the back makes a significant impact in the appearance of

absorber microstructure in terms of compactness of the grains and their size. Even with 80 Å NaF at the back of the absorber, the grains are much smaller than and not as compact as the grains in the absorber with 40 Å NaF at the front which shows large, compact and faceted grains.

In order improve the performance of the CIGSe devices it was planned to carry out sulfurization following selenization process. To begin with, precursors with 40 Å NaF in the front were selenized and sulfurized for 40 minutes and 5 minutes respectively. The selenization time was reduced so that the films are selenium deficient and that the sulfur would substitute for the selenium vacancies.
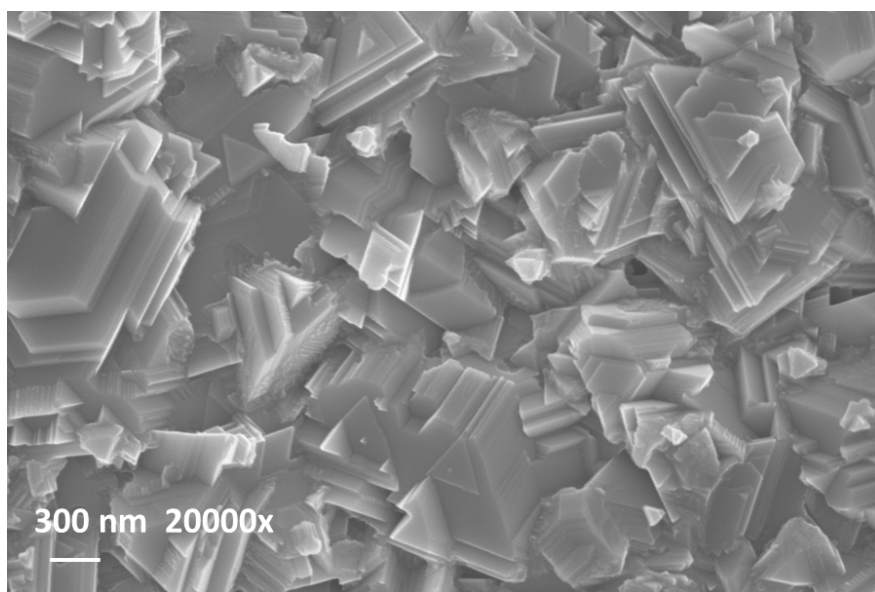
Figure 60 SEM micrograph of the absorber film 40 min and sulfurized for 5min at 500 °C (#0818)

Figure 60 provides the SEM micrographs of the resulting CIGSeS absorber film showing distinct faceting of the grains that are close and compact in arrangement. Figure 57 provides the XRD pattern for the film showing the (101), (112), (201), (211), (220/204), (312/116), and other

reflections of highly crystalline chalcopyrite CIGSeS and also the reflection from molybdenum. The molybdenum reflection was observed at $2\theta = 40.52°$. The strongest reflection was from (112) plane at $2\theta = 26.7°$. The lattice parameters calculated using the XRD data were $a_0 = 5.645$ Å and $c_0 = 11.274$ Å. Table 11 provides the elemental composition of the representative sample #0818 with and without KCN etching. It can be noted that there is seldom difference in the compositions of the absorber films with and without KCN etching. This is a good indication of the fact that there is insignificant amount of residual $Cu_{2-x}Se_x$ phase present at the absorber surface.
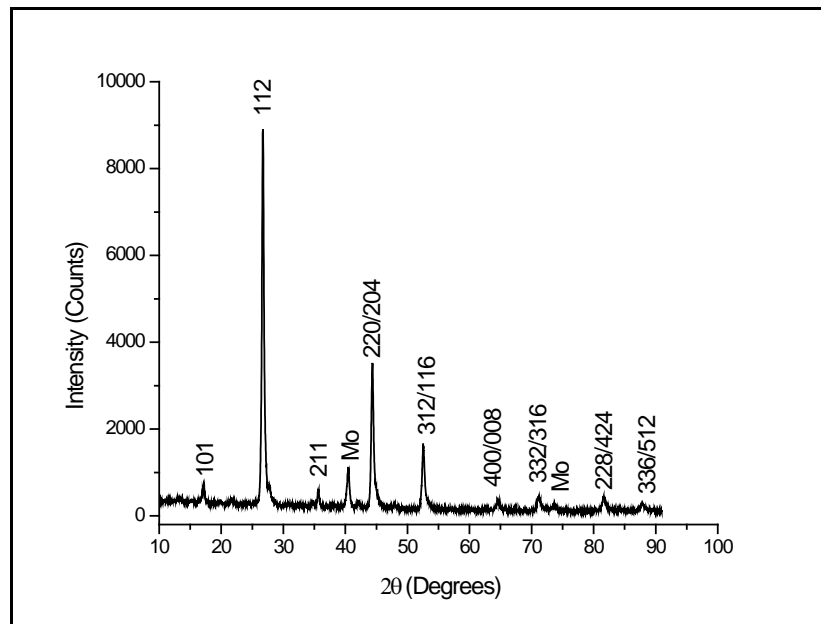
Figure 61 XRD pattern for CIGSeS thin film (#0818)

Table 11 EPMA analysis of absorber films selenized for 40 min and sulfurized for 5min at 500 °C

Element	Cu	In	Ga	Se	S	Cu/(In+Ga)	S/(S+Se)
10kV (Unetched)	19.71	29.29	1.04	45.02	4.94	0.65	0.1
20kV (Unetched)	20.36	27.75	0.25	48.28	3.36	0.73	0.07
10kV (Etched)	19.58	29.59	1.13	45.78	3.92	0.64	0.08
20kV (Etched)	20.61	27.75	0.24	48.78	2.61	0.73	0.05
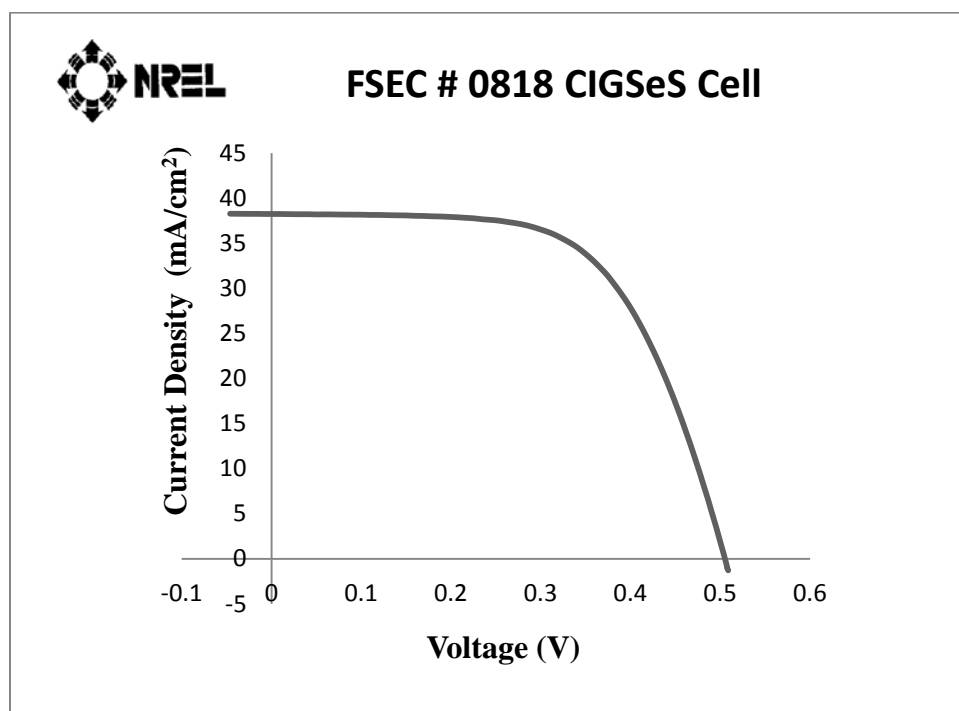
Figure 62 I-V characteristic of cell # 0818-8 selenized at 500 °C for 40 min and sulfurized for 5min

Table 12 Summary of PV characteristics for cell # 0818-8

Parameter	Voc (V)	Jsc (mA/cm^2)	FF (%)	ɳ (%)	R_s (Ω-cm^2)	R_{sh} (Ω-cm^2)
Values	0.51	38.24	61.39	11.85	3.0	1175

From the information provided by Figure 62 and Table 12, it can be seen that sulfurization treatment resulted in a significant improvement in the V_{oc} of the completed device. In order to understand the effect of additional NaF in the front under similar processing conditions that were used for sample # 0818, 80Å NaF was deposited in the front of the absorber and selenized and sulfurized at 500 °C for 40 minutes and 5 minutes respectively.
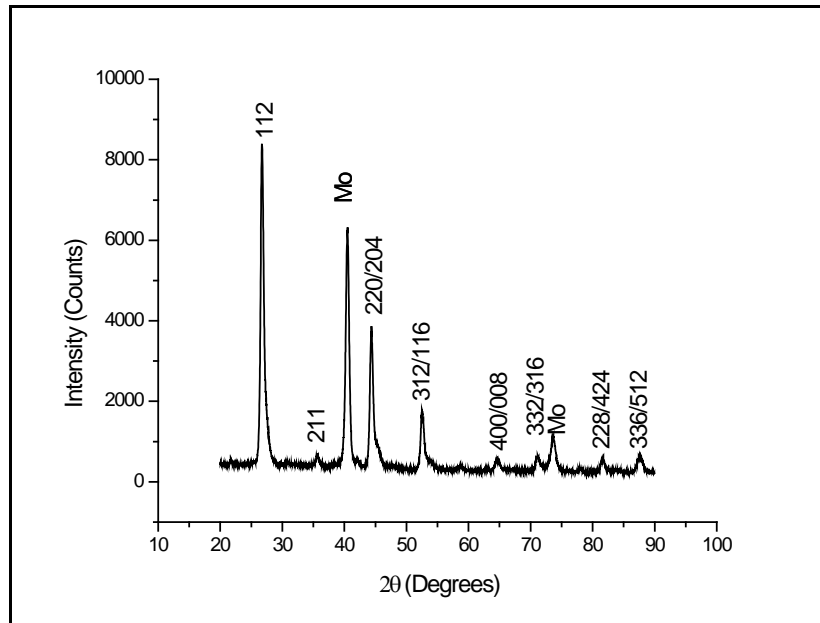
Figure 63 XRD pattern for CIGSeS absorber thin film (#0824)

Figure 63 provides the XRD pattern for the resulting CIGSeS absorber film (#0824) with all the major reflections. The molybdenum reflection was observed at $2\theta = 40.46°$. The strongest reflection was from (112) plane at $2\theta = 26.72°$. The lattice parameters calculated using the XRD data were $a_0 = 5.636$ Å and $c_0 = 11.260$ Å. EPMA data in Table 13 provides the elemental composition of the as-prepared absorber film.

Table 13 Elemental Composition of absorber film (# 0824)

Element	Cu	In	Ga	Se	S	Cu/(In+Ga)	S/(S+Se)
10kV (Etched)	21.72	28.17	0.86	45.29	3.95	0.748	0.08
20kV (Etched)	21.99	26.83	0.26	48.67	2.21	0.812	0.04
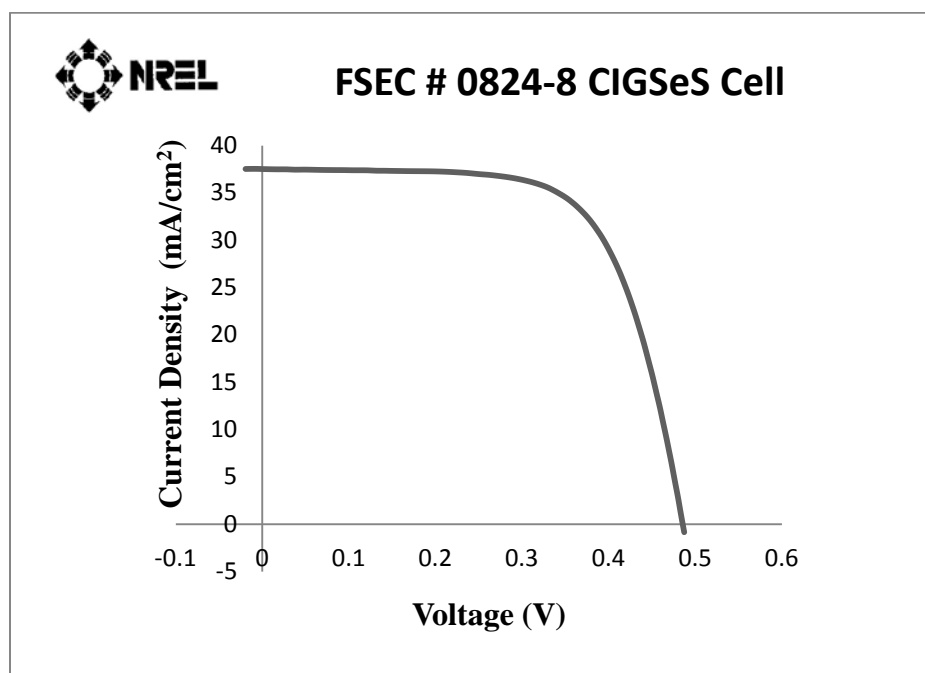
Figure 64 I-V characteristic of cell # 0824-8 selenized at 500 °C for 40 min and sulfurized for 5min with 80Å NaF

Table 14 Summary of PV characteristics for cell # 0824-8

Parameter	V_{oc} (V)	Jsc (mA/cm^2)	FF (%)	ɳ (%)	R_s (Ω-cm^2)	R_{sh} (Ω-cm^2)
Values	0.49	37.51	66.81	12.20	2.3	819.4

Figure 64 provides the NREL certified I-V characteristics for one of the representative device completed on the absorber sample #0824. Table 14 summarizes the PV parameters extracted from the I-V characteristics of cell # 0824-8. From the comparison of PV parameters of cell #0824 and #0818 it can be seen that additional NaF in cell # 0824 resulted in an 8.8 % increase in the fill factors compared to # 0818. Though there is a slight decrease in the J_{sc} and V_{oc} values of the former.

One common observation with all the samples that had NaF on the top is that the V_{oc} values are better than those with NaF at the back. It is known that selenization of films containing sodium results in the formation of NaSe$_x$ compounds that retard the growth of the CIGS phase and therefore facilitate better incorporation of selenium in the film. Now, when the sodium is readily available on top of the precursor this process of selenium incorporation through the formation of NaSe$_x$ compounds is much faster. Improvement in V_{oc} with addition of NaF has also been reported elsewhere [128]. It has been found that passivation of defect near the CdS/CIGS junction accounts for the increase in V_{oc} and improved junction properties. It was also observed that samples with 40 Å NaF on top (168 nm) had lower roughness than samples with 80 Å NaF on top (189 nm) as seen in the AFM images in Figure 65. The roughness values are lower than the values observed elsewhere for samples with 40 Å on the bottom (210 nm) of the metallic precursor [59].

106

#0818   40 Å NaF   #0824   80 Å NaF
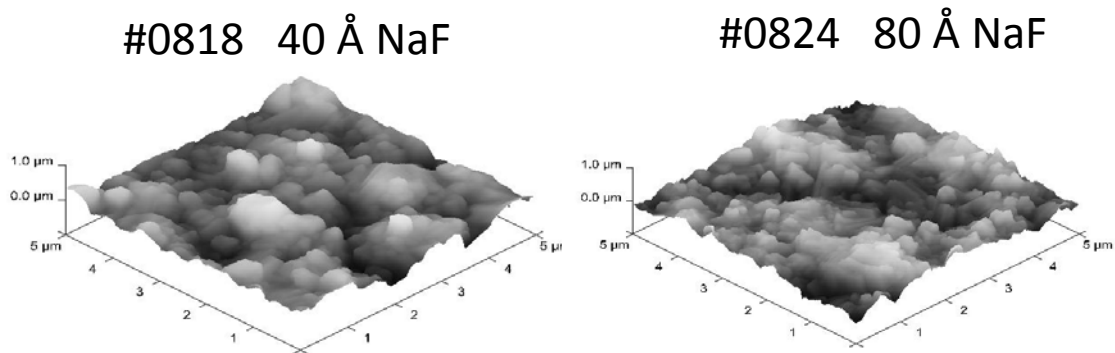
Figure 65 AFM images of sample # 0818 and # 0824
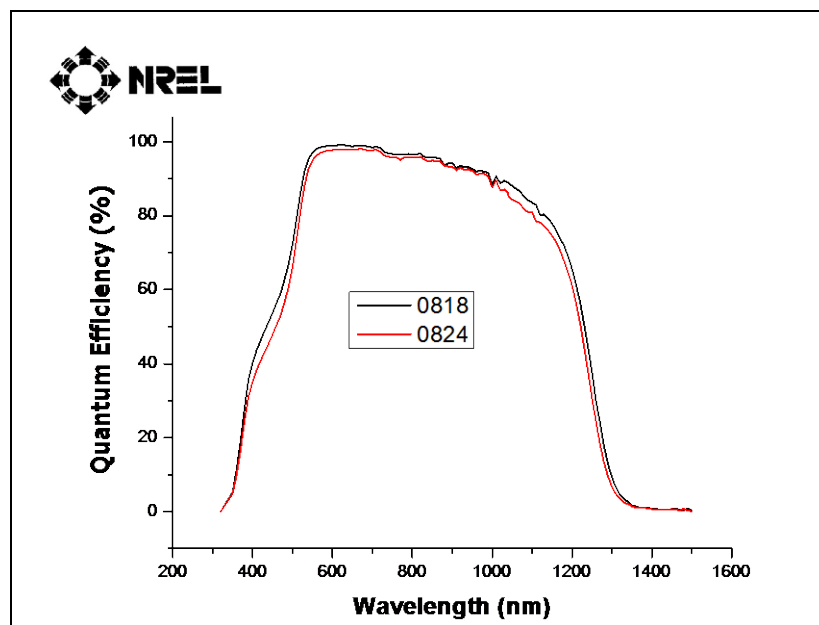
Figure 66 Comparison of Quantum Efficiency curves for CIGSeS device #0818-8 and #0824-8

Figure 66 shows the comparison of quantum efficiency (QE) curves for cell # 0818-8 and #0824-8. It can be seen that the QE curve for #0818 is uniformly offset from the QE curve of #0824 except in the regions 1 and 2 where the difference is large. This slight offset present between the curves is reflected in the slightly higher Jsc values for #0818 compared to #0824.

The losses corresponding to region 1 is due to absorption in the CdS layer. The loss in the QE for most heterojunction partner layers is proportional to the thickness of the CdS layer. This variation in the thickness is the possible reason for the large offset corresponding to this region. The QE response is reasonably flat in the wavelength range of 550 – 850 nm. The losses corresponding to region 2 are mainly due to incomplete collection of photogenerated carriers in the absorber.

From the above study it can be concluded that better CIGSeS absorbers can also be prepared with deposition of NaF on top of the metallic precursor films. This is a very useful finding both from a scientific understanding and also from a manufacturing view point. What is implied from this study is that irrespective of the sodium location it is possible to obtain devices with reasonable efficiencies. Moreover, it has been observed that sodium on top of the precursor provides comparatively better devices than sodium at the back. This finding can be effectively utilized for a useful application so as to speed up the deposition process for fabrication of CIGS solar cells, which is one of the goals of this study. Similar to using sodium doped molybdenum targets for deposition of back contact, it could be possible to dope a controlled amount of sodium in the metallic precursor targets and thereby eliminate the need for a separate step for the deposition of NaF.

CHAPTER 6 CONCLUSIONS AND FUTURE WORK

In this research, development of device quality, single layer molybdenum back contact with minimum residual stress and resistivity was successfully realized. Initially, study of relationship between sputtering parameters with properties of deposited films was carried out at a working distance of 9 cm. However, significant residual stress was found to remain even at low pressure and high power sputtering conditions. Later, by reducing the working distance to 7 cm it was found that the deposited films had low residual stress which was reflected in no observable bending in the glass strips attached to the glass substrates during deposition. It was found that the stress state and microstructure varied from location to location on the stationary glass substrate. Both tensile and compressive stress states were observed in the thin glass strips attached to the stationary glass substrate. Films were deposited on moving substrates at sputtering power of 300 W and at pressures of <0.1 mTorr, 0.3 mTorr, and 1 mTorr. No observable residual stress was detected in any of these films. The films were also found to be stable at high temperatures with no signs of cracking or flaking.

Attempt was made to fabricate CIGS2 solar cells on the developed single layer molybdenum back contact since processing in H_2S ambient is a harsher environment than processing in selenium ambient. CIGS2 thin film solar cell with device efficiency of 11.38 % was successfully fabricated on this back contact without any sign of peeling of the absorber layer. Attempts to increase the deposition rates for CuGa and In targets by changing the working distance, increasing the power and reducing the sputtering pressure were also successful. With this study it has become possible to deposit molybdenum back contact and the metallic precursor all at identical pressure conditions, allowing in-line deposition.

Optimization of sodium precursor was also carried out in this research work and it was found that better device could be obtained with sodium fluoride deposited on top of the metallic precursor. Sulfurization of absorber films resulted in improvement in the open-circuit voltages. NREL certified device efficiency of 12.2 % was obtained for CIGSeS device with 80 Å NaF in the front. This result shows that one could incorporate sodium fluoride within the metallic target and thereby eliminate the need for any additional step for sodium deposition thus saving considerable time in manufacturing line.

It will be very interesting and useful to study the molybdenum-CIGS interface for devices with 40 Å and 80 Å NaF in the front and at the back to see the effect of location of NaF on the formation of molyselenide layer and its thickness. Optimization of sulfurization profile will be very useful in order to improve the open-circuit voltages for the devices and thus improve efficiencies. It will also be useful to study the effect of location of NaF on the composition gradient of the devices and their effect on device characteristics.

REFERENCES

[1] "World Energy Outlook," November 2011.

[2] "Fossil Fuel," http://en.wikipedia.org/wiki/Fossil_fuel.

[3] "Global warming," http://cobwebsandseaslugs.com/global-warming.

[4] R. Nielsen, "How Much Solar Energy Can We Harvest?," *http://home.iprimus.com.au/nielsens/*, 2005

[5] "Statistical Review of World Energy 2012", www.bp.com

[6] Thin Film 2012–2016: Technologies, Markets and Strategies for Survival, GTM Research, April 2012.

[7] S.M. Sze, "Semiconductor Device Physics", John Wiley and Sons Inc., 2001.

[8] G. Liu, T. Schulmeyer, J. Brotz, A. Klein, W. Jaegermann, Thin Solid Films 431, 477 (2003).

[9] P. Jackson, D. Hariskos, E. Lotter, S. Paetel, R. Wuerz, R. Menner, W. Wischmann and M. Powalla, "New world record efficiency for $Cu(In,Ga)Se_2$ thin-film solar cells beyond 20%", 25th EUPVSEC, Valencia, Spain, 2010.

[10] C. Rincón and J Gonzalez, "Temperature Dependence of the Bandgap in $CuInSe_2$", Solar Cells, vol.16, 357, 1986.

[11] W. Hörig, H. Neumann, H. Sobotta, B. Schumann and G. Kühn, "The optical properties of $CuInSe_2$ thin films," *Thin Solid Films*, vol. 48, pp. 67-72, 1978.

[12] D.S. Albin,. J.J.. Carapella, J.R. Tuttle, and. R. Noufi, *Material Research Society Symposium Proceedings*, vol. 228, pp. 267-272, 1991

[13] Dimmler, H. Dittrich, R. Menner, and H.W. Schock, "Performance and Optimization of Heterojunctions Based on $Cu(Ga,In)Se_2$", *Proceedings of 19th IEEE Photovoltaic Specialist Conference*, New York, 1454, 1987.

[14] R. W. Birkmire and E. Eser, "Polycrystalline Thin Film Solar Cells: Present Status and Future Potential", Annual Review of Material Science, vol. 27, 625, 1997.

[15] T. Dullweber, O. Lundberg, J. Malmstrom, M. Bodegard, L. Stolt, U. Rau, H.W. Schock and J.H. Werner, "Back Surface Band Gap Gradings in Cu(In,Ga)Se$_2$ Solar Cells", Thin Solid Films, vol. 387 (1-2), 11, 2001.

[16] T. Nakada, H. Ohbo, T. Watanabe, H. Nakazawa, M. Matsui and A. Kunioka, "Improved Cu(In,Ga)(S,Se)$_2$ thin film solar cells by surface sulfurization," *Solar Energy Materials and Solar Cells*, vol. 49, pp. 285-290, 1997.

[17] U. Rau and H.W. Schock, "Cu(In,Ga)Se$_2$ Solar Cells," in *Clean Electricity from Photovoltaics*, M.D. Archer and R. Hill, Imperial College Press, vol. 1, Ch. 7, pp. 277-345, 2001.

[18] T. Haalboom, T. Gödecke, F. Ernst, M. RuHle, R. Herberholz, H.W. Schock, C. Beilharz and K.W. Benz, "Phase Relation and Microstructure in Bulk Materials and Thin Films of the Ternary System Cu-In-Se," *Proceedings of the 11th International Conference on Ternary and Multinary compounds*, ICTMC-11, University of Salford, pp. 249-252, 1997.

[19] T. Negami, N. Kohara, M. Nishitani, T. Wada and T. Hirao, "Preparation and characterization of Cu(In$_{1-x}$Ga$_x$)$_3$Se$_5$ thin films," *Applied. Physics Letters*, vol. 67, pp. 825-827, 1995.

[20] D. Schmid, M. Ruckh, F. Grunwald and H.W. Schock, "Chalcopyrite/defect chalcopyrite heterojunctions on the basis of CuInSe$_2$," *Journal of Applied Physics*, vol. 73, pp. 2902-2909, 1993.

[21] A. Niemegeers, M. Burgelman, R. Herberholz, U. Rau, D. Hariskos and H.W. Schock, "Model for Electronic Transport in Cu(In,Ga)Se2 Solar Cells," *Progress in Photovoltaics: Research and Applications*, vol. 6, pp. 407-421, 1998.

[22] D. Schmid, M. Ruckh, F. Grunwald and H.W. Schock, "Chalcopyrite/defect chalcopyrite heterojunctions on the basis of CuInSe2," *Journal of Applied Physics*, vol. 73, pp. 2902-2909, 1993.

[23] A. Niemegeers, M. Burgelman, R. Herberholz, U. Rau, D. Hariskos and H.W. Schock, "Model for Electronic Transport in Cu(In,Ga)Se$_2$ Solar Cells," *Progress in Photovoltaics: Research and Applications*, vol. 6, pp. 407-421, 1998.

[24] H. W. Schock and R. Noufi, "CIGS-based solar cells for the next millennium," *Progress in Photovoltaics: Research and Applications*, vol. 8, pp. 151-160, 2000.

[25] R. Klenk, "Characterisation and modelling of chalcopyrite solar cells," *Thin Solid Films*, vol. 387, pp. 135-140, 2001.

[26] R. Herberholz, U. Rau, H.W. Schock, T. Haalboom, T. Gödecke, F. Ernst, C. Beilharz, K.W. Benz and D. Cahen, "Phase segregation, Cu migration and junction formation in $Cu(In, Ga)Se_2$," *The European Physical Journal Applied Physics*, vol. 6, pp. 131-139, 1999.

[27] R.W. Birkmire, L.C. DiNetta, P.G. Lasswell, J.D. Meakin and J.E. Phillips, "High efficiency $CuInSe_2$ based heterojunction solar cells: Fabrication and results," *Solar Cells*, vol. 16, pp. 419-427, 1986.

[28] M.A. Contreras, B. Egaas, K. Ramanathan, J. Hiltner, A. Swartzlander, F. Hasoon and R. Noufi, "Progress toward 20% efficiency in $Cu(In,Ga)Se_2$ polycrystalline thin-film solar cells," *Progress in Photovoltaics: Research and Applications*, vol. 7, pp. 311-316, 1999.

[29] W.N. Shafarman and J. Zhu, "Effect of substrate temperature and deposition profile on evaporated $Cu(InGa)Se_2$ films and devices," *Thin Solid Films*, vol. 361-362, pp. 473-477, 2000.

[30] T. Negami, Y. Hashimoto and S. Nishiwaki, "$Cu(In,Ga)Se_2$ thin-film solar cells with an efficiency of 18%," *Solar Energy Materials and Solar Cells*, vol. 67, pp. 331-335, 2001.

[31] J. Piekoszewski, J.J. Loferski, R. Beaulieu, J. Beall, B. Roessler and J. Shewchun, "RF-sputtered $CuInSe_2$ thin films," *Solar Energy Materials,* vol. 2, pp. 363-372, 1980

[32] L.D. Laude, M.C. Joliet and C. Antoniadis, "Laser-induced synthesis of thin $CuInSe_2$ films," *Solar Cells,* vol. 16, pp. 199-209, 1986.

[33] J.A. Thornton, T.C. Lommasson, H. Talieh and B. Tseng, "Reactive sputtered $CuInSe_2$," *Solar Cells*, vol. 24, pp. 1-9, 1988.

[34] C. R. Abernathy, Jr, A. A. Anani, B. Haba, and G. Smestad, "Production of single phase chalcopyrite $CuInSe_2$ by spray pyrolysis," *Applied Physics Letters*, vol. 45, pp. 890-892, 1984

[35] C.W. Bates, K.F. Nelson, S. Atiq Raza, J.B. Mooney, J.M. Recktenwald, L. Macintosh and R. Lamoreaux, "Spray pyrolysis and heat treatment of CuInSe$_2$ for photovoltaic applications," *Thin Solid Films*, vol. 88, pp. 279-283, 1982.

[36] J. Bougnot, S. Duchemin and M. Savelli, "Chemical spray pyrolysis of CuInSe$_2$ thin films," *Solar Cells*, vol. 16, pp. 221-236, 1986.

[37] B. Schumann, A. Tempel and G. Kühn, "Epitaxial layers of CuInSe$_2$," *Solar Cells,* vol. 16, pp. 43-63, 1986.

[38] H. Takenoshita, "Liquid phase epitaxial growth and electrical characterization of CuInSe$_2$," *Solar Cells*, vol. 16, pp. 65-89, 1986.

[39] V.K. Kapur, B.M. Basol and E.S. Tseng, "Low cost methods for the production of semiconductor films for CuInSe$_2$/CdS solar cells," *Solar Cells*, vol. 21, pp. 65-72, 1987.

[40] Y. Ueno, H. Kawai, T. Sugiura and H. Minoura, "Electrodeposition of CuInSe$_2$ films from a sulphate bath," *Thin Solid Films*, vol. 157, pp. 159-168, 1988.

[41] V.K. Kapur, A. Bansal, P. Le and O.I. Asensio, "Non-vacuum processing of CuIn$_{1-x}$Ga$_x$Se$_2$ solar cells on rigid and flexible substrates using nanoparticle precursor inks," *Thin Solid Films*, vol. 431-432, pp. 53-57, 2003

[42] G. Hodes, T. Engelhard, D. Cahen, L.L. Kazmerski and C.R. Herrington, "Electroplated CuInS$_2$ and CuInSe$_2$ layers: Preparation and physical and photovoltaic characterization," *Thin Solid Films*, vol. 128, pp. 93-106, 1985

[43] B. M. Basol, V. K. Kapur, A. Halani, C. R. Leidholm, J. Sharp, J. R. Sites, A. Swartzlander, R. Matson, and H. Ullal, "Cu(In,Ga)Se$_2$ thin films and solar cells prepared by selenization of metallic precursors," *Journal of Vacuum Science & Technology A: Vacuum, Surfaces, and Films,* vol. 14, pp. 2251-2256, 1996

[44] M. Marudachalam, R. W. Birkmire, H. Hichri, J. M. Schultz, A. Swartzlander, and A. M. M. Jassim, "Phases, morphology, and diffusion in CuIn$_x$Ga$_{1-x}$Se$_2$ thin films," *Journal of Applied Physics*, vol. 82, pp. 2896-2905, 1997

[45] N.G. Dhere, S.S. Kulkarni, A.H. Jahagirdar and A.A. Kadam, "Composition and morphology of partially selenized CuIn$_{1-x}$Ga$_x$Se$_2$ thin films prepared using

diethylselenide (DESe) as selenium source," *Journal of Physics and Chemistry of Solids*, vol. 66, pp. 1876-1879, 2005

[46] K. Zweibel, "Harnessing Solar Power: The Photovoltaic challenge," ISBN 0-306-43564-0, 1st ed., Plenum Publishing, New York, 1990.

[47] N. G. Dhere, S. Kuttath and H. R. Moutinho, "Morphology of Precursors and CuInGaSe2 Thin Films Prepared by a Two-stage Selenization Process", *Journal of Vacuum Science and Technology*, A, vol. 13(3), 1078, 1995.

[48] N. G. Dhere and K. W. Lynn, "Gallium Content Enhancement In CIGS Thin Films Prepared By Two-Selenization Process Using Se Vapor", 25th Photovoltaic Specialists Conference, 897, 1996.

[49] T. Yamamoto, M. Nakamura , J. Ishizuki, T. Deguchi, S. Ando, H. Nakanishi and S.F. Chichibu, "Use of Diethylselenide as a Less-hazardous Source for Preparation of $CuInSe_2$ Thin Films by Selenization of Metal Precursors", Journal of Physics and Chemistry of Solids, vol. 64, 1855, 2003.

[50] A. H. Jahagirdar, N. G. Dhere, S. S. Kulkarni, A. A. Kadam, J. S. Shirolikar, H. Moutinho and B. To, "Preparation and Properties of CIGS and CIGSeS Thin Films using DESe as a Selenium Source and H2S as Sulfur Source", Photovoltaic Specialists Conference, Conference Record of the 31st IEEE, 414, 2005.

[51] A. Jahagirdar, "Solar Driven Photoelectrochemical Water Splitting for Hydrogen Generation using Multiple Bandgap Tandem Of CIGS2 PV Cells and Thin Film Photocatalyst", Ph.D. thesis, University of Central Florida, 2005.

[52] A. Kadam, "Preparation of Efficient CIGSS/CdS Thin-Film Solar Cells by Optimizing the Mo Back Contact and using Diethylselenide as Selenium Precursor", Ph.D. thesis, University of Central Florida, 2006.

[53] R. Herberholz, U. Rau, H.W. Schock, T. Haalboom, T. Gödecke, F. Ernst, C. Beilharz, K.W. Benz and D. Cahen, "Phase segregation, Cu migration and junction formation in $Cu(In, Ga)Se_2$," *The European Physical Journal Applied Physics*, vol. 6, pp. 131-139, 1999.

[54] R. Noufi, R. Axton, C. Herrington and S.K. Deb, "Electronic Properties Versus Composition of Thin Films of CuInSe$_2$", Applied Physics Letter, vol. 45, 668, 1984.

[55] P. Migliorato, J.L. Shay, H.M. Kasper and S. Wagner, "Analysis of the Electrical and Luminescent Properties of CuInSe$_2$", Journal of Applied Physics, vol. 46, 1777, 1975.

[56] M.A. Contreras, B. Egaas, P. Dippo, J. Webb, J. Granata, K. Ramnathan, S. Asher, A. Swartzlander and R. Noufi, "On the Role of Na and Modifications to Cu(ln,Ga)Se$_2$ Absorber Materials Using Thin-MF (M=Na, K, Cs) Precursor Layers", conference proceedings of 26th IEEE Photovoltaic Specialists Conference, Anaheim, IEEE Press, Piscataway, 359, 1997.

[57] D. Braunger, S. Zweigart and S.W. Schock, "The Influence of Na and Ga on the Incorporation of the Chalcogen in Polycrystalline Cu(In,Ga)(S,Se)2 Thin-Films for photovoltaic Applications", 2nd World Conference of Photovoltaic Solar Energy Conversion, Vienna, 1113, 1998.

[58] S.H. Wei, S.B. Zhang and A. Zunger, "Effects of Na on the Electrical and Structural Properties of CuInSe$_2$", Journal of Applied Physics, vol. 85, 7214, 1999.

[59] V. V. Hadagali, "Study of the effects of sodium and absorber microstructure for the development of CuIn$_{1-x}$Ga$_x$Se$_{2-y}$S$_y$ thin film solar cells using an alternative selenium precursor", PhD Dissertation, University of Central Florida, Spring 2009.

[60] P. S. Vasekar, "Effect of sodium and absorber thickness on CIGS2 thin film solar cells", PhD Dissertation, University of Central Florida, Spring 2009.

[61] S. A. Pethe, " Optimization of process parameters for reduced thickness CIGSeS thin film solar cells", PhD Dissertation, University of Central Florida, Fall 2010.

[62] J. Palm, V. Probst, F. H. Karg, "Second generation CIS solar modules" *Solar Energy*, vol. 77, pp. 757–765, 2004.

[63] K. Granath, M. Bodegard, and L. Stolt, "The effect of NaF on Cu(In,Ga)Se$_2$ Thin Film Solar Cells," *Solar Energy Materials and Solar Cells*, vol. 60, pp. 279-293, 2000.

[64] S. Ishizuka, A. Yamada, and S. Niki, "Efficiency enhancement of flexible CIGS solar cells using alkali-silicate glass thin layers as an alkali source material", *IEEE Photovoltaic Specialists Conference*, 2009.

[65] R. Wuerz, A. Eicke, F. Kessler, P. Rogin, O. Yazdani-Assl, "Alternative sodium sources for Cu(In,Ga)Se$_2$ thin-film solar cells on flexible substrates", Thin Solid Films.

[66] J.H. Scofield, A. Duda, D. Albin, B.L. Ballard, and P.K. Predecki, "Sputtered molybdenum bilayer back contact for copper indium diselenide-based polycrystalline thin-film solar cells," *Thin Solid Films*, vol. 260, pp. 26-31, 1995.

[67] F.A. Abou-Elfotouh, L.L. Kazmerski, R.J. Matson, D.J. Dunlavy, and T.J. Coutts, "Studies of the electrical and interface properties of the metal contacts to CuInSe$_2$ single crystals," *Journal of Vacuum Science and Technology A*, vol. 8, pp. 3251-3254, 1990

[68] S. Ashour, S. Alkuhaimi, H. Moutinho, R. Matson, and F. Abou-Elfotouh, "Junction formation and characteristics of CdS/CuInSe$_2$/metal interfaces," *Thin Solid Films*, vol. 226, pp. 129-134, 1993.

[69] F.A. Abou-Elfotouh, L.L. Kazmerski, T.J. Coutts, R.J. Matson, S.E. Asher, A.J. Nelson, and A.B. Swartzlander-Franz, "Interface properties of (Cd,Zn)S/CuInSe2 single-crystal solar cells," *Journal of Vacuum Science and Technology A*, vol. 7, pp. 837-841, 1989.

[70] R.J. Matson, O. Jamjoum, A.D. Buonaquisti, P.E. Russell, L.L. Kazmerski, P. Sheldon, and R.K. Ahrenkiel, "Metal contacts to CuInSe$_2$," *Solar Cells*, vol. 11, pp. 301-305, 1984.

[71] E. Moons, T. Engelhard, D. Cahen, "Ohmic contacts to p-CuInSe$_2$ crystals," Journal of Electronic Materials, vol. 22, no. 3, pp. 275-280, 1993.

[72] D.W. Niles *et al*., *Materials Research Society Symposium Proceedings*, vol. 260, p. 299, 1992.

[73] E. Moons, T. Engelhard and D. Cahen, "Ohmic contacts to *p*-CuInSe$_2$ crystals," Journal of Electronic Materials, vol. 22, pp. 275-280, 1993.

[74] S. Ashour, A.H. Moutinho, R. Matson, and F. Abou-Elfotouh, "Junction formation and characteristics of CdS/CuInSe$_2$/Metal interfaces," *Thin Solid Films*, vol. 226, pp. 129-134, 1993.

[75] K. Granath, A. Rockett, M. Bodegard, C. Nender, and L. Stolt, "Mechanical Issues of Mo Bacck Contact for Cu(InGa)Se$_2$", in *Proceedings of the 13th European Photovoltaic Solar Energy Conference*, 1995, p. 1983.

[76] L. Assmann, J.C. Bernède, A. Drici, C. Amory, E. Halgand, and M. Morsli, "Study of the Mo thin films and Mo/CIGS interface properties," *Applied Surface Science,* vol. 246, pp. 159-166, 2005.

[77] J.A. Thornton and D.W. Hoffman, "Stress-related effects in thin films," *Thin Solid Films*, vol. 171, pp. 5-31, 1989.

[78] D.W. Hoffman and J.A. Thornton, "Internal stresses in Cr, Mo, Ta, and Pt films deposited by sputtering from a planar magnetron source," *Journal of Vacuum Science and Technology*, vol. 20, pp. 355-358, 1982.

[79] J.A. Thornton and D.W. Hoffman, "The influence of discharge current on the intrinsic stress in Mo films deposited using cylindrical and planar magnetron sputtering sources," *Journal of Vacuum Science and Technology A*, vol. 3, pp. 576-579.

[80] T.J. Vink, M.A.J. Somers, J.L.C. Daams, and A.G. Dirks, "Stress, strain, and microstructure of sputter-deposited Mo thin films," *Journal of Applied Physics*, vol. 70, pp. 4301-4308, 1991.

[81] K. Orgassa, H.W. Schock, and J.H. Werner, "Alternative back contact materials for thin film Cu(In,Ga)Se2 solar cells," *Thin Solid Films*, vol. 431-432, pp. 387-391, 2003.

[82] T. Yamaguchi and R. Miyagawa, "Effects of oxygen on the properties of sputtered molybdenum thin films," *Japanese Journal of Applied Physics*, vol. 30, pp. 2069-2073, 1991.

[83] B.L. Ballard, P.K. Predecki, D. Albin, and J.H. Scofield, *Advance in X-ray Analysis*, vol. 38, 1994.

[84] K. Granath et al., in *Proceedings of the 13th European Photovoltaic Solar Energy Conference*, 1995, pp. 1483.

[85] R. Menner, E. Gross, A. Eicke, H. Dittrich, J. Springer, B. Dimmler, U. Rühle, M. Kaiser, T. Magorian-Friedlmeier, and H.W. Schock, "Investigations on sputter deposited molybdenum back contacts for Cu(In,Ga)Se$_2$," in *Proceedings of the 13th European Photovoltaic Solar Energy Conference*, 1995, pp. 2067.

[86] B.C. Bell and D.A. Glocker, "The effect of initial growth conditions on the stress profiles of Mo sputtered onto both moving and stationary substrates," *Journal of Vacuum Science and Technology A*, vol. 10, no. 4, pp. 1442-1445, 1992.

[87] Y.G. Shen, "Effect of deposition conditions on mechanical stresses and microstructure of sputter-deposited molybdenum and reactively sputter-deposited molybdenum nitride films," *Materials Science and Engineering A*, vol. 359, pp. 158-167, 2003.

[88] G. Gordillo, M. Grizález, and L.C. Hernandez, "Structural and electrical properties of DC sputtered molybdenum films," *Solar Energy Materials and Solar Cells*, vol. 51, pp. 327-337, 1998.

[89] C. X. Qiu and I. Shih, "Investigation of electrodeposited $CuInSe_2$ films," *Canadian Journal of Physics*, vol. 65, pp. 1011-1014, 1987.

[90] S. N. Qiu, L. Li, C. X. Qiu, I. Shih, and C. H. Champness, "Study of $CuInSe_2$ thin films prepared by electrodeposition," *Solar Energy Materials and Solar Cells*, vol. 37, pp. 389-393, 1995.

[91] D. Rudmann, G. Bilger, M. Kaelin, F.-. Haug, H. Zogg and A.N. Tiwari, "Effects of NaF coevaporation on structural properties of $Cu(In,Ga)Se_2$ thin films," *Thin Solid Films*, vol. 431-432, pp. 37-40, 2003.

[92] W.N. Shafarman and L. Stolt, "$Cu(InGa)Se_2$ Solar Cells," in Handbook of Photovoltaic Science & Engineering, A. Luque and S. Hegedus, Eds., *John Wiley & Sons*, Ltd, 2003, ch. 13, pp. 567-616

[93] M. A. Contreras, M. J. Romero, B. To, F. Hasoon, R. Noufi, S. Ward, and K. Ramanathan, "Optimization of CBD CdS process in high-efficiency $Cu(In,Ga)Se_2$-based solar cells," *Thin Solid Films*, vol. 403-404, pp. 204-211, 2002

[94] S. N. Qiu, W. W. Lam, C. X. Qiu, and I. Shih, "$ZnO/CdS/CuInSe_2$ photovoltaic cells fabricated using chemical bath deposited CdS buffer layer," *Applied Surface Science*, vol. 113-114, pp. 764-767, 1997

[95] Y. Hashimoto, N. Kohara, T. Negami, N. Nishitani and T. Wada, "Chemical bath deposition of Cds buffer layer for CIGS solar cells," *Solar Energy Materials and Solar Cells*, vol. 50, pp. 71-77, 1998

[96] J. Hedstrom, H. Ohlsen, M. Bodegard, A. Kylner, L. Stolt, D. Hariskos, M. Ruckh and H.-. Schock, "ZnO/CdS/Cu(In,Ga)Se$_2$ thin film solar cells with improved performance," *Proceedings of the 23rd IEEE Photovoltaic Specialists Conference*, 1993., pp. 364-371, 1993

[97] S. Ishizuka, K. Sakurai, A. Yamada, K. Matsubara, P. Fons, K. Iwata, S. Nakamura, Y. Kimura, T. Baba, and H. Nakanishi, "Fabrication of wide-gap Cu(In$_{1-x}$Ga$_x$)Se$_2$ thin film solar cells: a study on the correlation of cell performance with highly resistive i-zno layer thickness," *Solar Energy Materials and Solar Cells*, vol. 87, no. 1-4, pp. 541-548, 2005

[98] J. Schoenes, K. Kanazawa, and E. Kay, "Band and hopping conduction in high-resistivity ZnO," *Journal of Applied Physics*, vol. 48, no. 6, pp. 2537-2542, 1977

[99] G. Neumann, "On the defect structure of zinc-doped zinc oxide," *physica status solidi (b)*, vol. 105, no. 2, pp. 605-612, 1981.

[100] T. Nakada, N. Murakami, A. Kunioka, "Comparison between Al- and B-doped ZnO window layers for CuInSe$_2$ thin film solar cells," *Material Research Society Symposium*, Vol. 426, pp. 411-410, 1996

[101] B. Choi, H. B. Im, J. S. Song, and K. H. Yoon, "Optical and electrical properties of Ga$_2$O$_3$-doped ZnO films prepared by r.f. sputtering," *Thin Solid Films*, vol. 193-194, pp. 712-720, 1990.

[102] J. Duenow, T. Gessert, D. Wood, D. Young, and T. Coutts, "Effects of hydrogen content in sputtering ambient on ZnO:Al electrical properties," *Journal of Non-Crystalline Solids*, vol. 354, pp. 2787-2790, 2008.

[103] R. Cebulla, R. Wendt, and K. Ellmer, "Al-doped zinc oxide films deposited by simultaneous rf and dc excitation of a magnetron plasma: Relationships between plasma parameters and structural and electrical film properties," *Journal of Applied Physics*, vol. 83, pp. 1087-1095, 1998.

[104] W. D. Westwood, "Reactive Sputter Deposition," in *Handbook of Plasma Processing Technology: Fundamentals, Etching, Deposition, and Surface Interactions*, S. M.

Rossnagel, J. J. Cuomo and W. D. Westwood, Eds., Park Ridge, N.J., U.S.A: Noyes Publications, Ch. 9, pp. 233-259, 1990.

[105] E. Jim´Enez-Gonz´Alez, J. A. S. Urueta, And R. Su´Arez-Parra, "Optical And Electrical Characteristics Of Aluminum Doped ZnO Thin Films Prepared By Solgel Technique," *Journal Of Crystal Growth*, vol. 192, pp. 430–438, 1998.

[106] L. Stolt, J. Hedstrom, and J. Skarp, "CIS solar cells with ZnO windows deposited by ALE," *1994 IEEE First World Conference on Photovoltaic Energy Conversion,* vol. 1, pp. 250-253, 1994.

[107] M. Hiramatsu, K. Iameda, N. Horio, And M. Nawata, "Transparent Conducting ZnO Thin Films Prepared By XeCl Excimer Laser Ablation," *Journal Of Vacuum Science And Technology A*, vol. 16, pp. 669– 673, 1998.

[108] D.B. Mitzi, O. Gunawan, T. K.Todorov, K. Wang, S. Guha. The path towards a high-performance solution based processed kesterite solar cell, *Solar Energy Materials & Solar Cells* **95,** pp. 1421–1436, 2011.

[109] T. K. Todorov, K. B. Reuter, D. B. Mitzi, High-Efficiency Solar Cell with Earth-Abundant Liquid-Processed Absorber, *Adv. Mater.* **22** pp. 1-4, 2010.

[110] K. Wang, O. Gunawan, T. Todorov, B. Shin, S. J. Chey, N. A. Bojarczuk, D. Mitzi, and. S. Guhaa. Thermally evaporated Cu_2ZnSnS_4 solar cells, *Appl. Phys. Lett*. 97, 143508, 2010.

[111] P.A. Fernandes, P.M.P. Salomé, A.F. da Cunha, Björn-Arvid Schubert. Cu_2ZnSnS_4 solar cells prepared with sulphurized dc-sputtered stacked metallic precursors. *Thin Solid Films,* Volume 519, Issue 21, pp. 7382–7385, 2011.

[112] H. Yoo, J. Kim. Growth of Cu2ZnSnS4 thin films using sulfurization of stacked metallic films. *Thin Solid Films* **518,** pp. 6567–6572, 2010.

[113] H.Katagiri, K.Jimbo, S.Yamada, T.Kamimura, W.S.Maw, T.Fukano, T.Ito, T. Motohiro, Enhanced conversion efficiencies of Cu2ZnSnS4-based thin film solar cells by using preferential etching technique, *Appl.Phys.Express* **1**, 41201, 2008.

[114] I. Repins, N.Vora, C. Beall, S. Wei, Y. Yan, M. Romero, G. Teeter, H. Du, B. To, M. Young, R. Noufi. Kesterites and Chalcopyrites: A Comparison of Close Cousins, MRS Symopsium Spring 2011.

[115] D. Hariskos, S. Spiering, M. Powalla. Buffer layers in Cu(In,Ga)Se$_2$ solar cells and modules, *Thin Solid Films* **480–481** pp. 99 2005.

[116] J. Marlein, K. Decock, M. Burgelman. Analysis of electrical properties of CIGSSe and Cd-free buffer CIGSSe solar cells, *Thin Solid Films* **517** pp. 2353, 2009.

[117] D. Hariskos, B. Fuchs, R. Menner, N. Naghavi, C. Hubert, D. Lincot and M. Powalla. The Zn(S,O,OH)/ZnMgO Buffer in Thin-Film Cu(In,Ga)(Se,S)$_2$-Based Solar Cells Part II: Magnetron Sputtering of the ZnMgO Buffer Layer for In-Line Co-Evaporated Cu(In,Ga)Se2 Solar Cells, *Prog. Photovolt: Res. Appl.* **17** pp. 479, 2009.

[118] T. Minemoto, T. Negami, S. Nishiwaki, H. Takakura and Y. Hamakawa, "Preparation of ZnMgO films by radio frequency magnetron sputtering", *Thin Solid Films* **372** pp. 173, 2000.

[119] T. Minemoto, Y. Hashimoto, T. Satoh, W.S. Kolahi, T. Negami, H. Takakura and Y. Hamakawa, "Control of conduction band offset in wide-gap Cu(In,Ga)Se$_2$ solar cells", *Sol. Energy Mater. Sol. Cells* **75** pp. 121, 2003.

[120] Jian V. Li, Xiaonan Li, Yanfa Yan, Chun-Sheng Jiang, Wyatt K. Metzger, Ingrid L. Repins, Miguel A. Contreras, and Dean H. Levi. Influence of sputtering a ZnMgO window layer on the interface and bulk properties of Cu(In,Ga)Se$_2$ solar cells, *J. Vac. Sci. Technol. B* **27** pp. 2384, 2009.

[121] L. Pinard and J. M. Mackowski, "Synthesis and physicochemical characterization of silicon oxynitride thin films prepared by rf magnetron sputtering", *Applied Optics*, Vol. 36, No. 22 pp. 5451, 1997.

[122] Y. Lipin, and E. Machevski, "Protective Properties of Silicon Nitride, Deposited by Bias Reactive Sputtering", *Society of Vacuum Coaters*, 42nd Annual Technical Conference Proceedings, 1999.

[123] N.G. Dhere, S.R. Ghondali, M.B. Pandit, A.H. Jahagirdar and D. Scheiman, "CIGS2 thin film solar cells on flexible foils for space power", *Progress in Photovoltaics: Research and Applications*, 10, pp. 407, 2002.

[124] S.D. Ekpe and S.K. Dew, "Theoretical and experimental determination of the energy flux during magnetron sputter deposition onto an unbiased substrate," *Journal of Vacuum Science and Technology A*, vol. 21, pp. 476-483, 2003.

[125] J. Musil, "Low pressure magnetron sputtering", Vacuum, Vol. 50, 3-4, pp. 363, 1998.

[126] K. Granath, L. Stold, M. Bodegerd, A. Rockett, and D. Schroeder, in *Proceedings of the 14th European Photovoltaic Solar Energy Conference*, pp. 1278, 1997.

[127] E.F. Kaeble, *Handbook of X-rays*, New York: McGraw-Hill, 1967.

[128] P. T. Erslev, J. W. Lee, W. N. Shafarman, J. D. Cohen, " The influence of Na on metastable defect kinetics in CIGS materials", *Thin Solid Films*, pp. 2277, 2009.

.